US Army Corp·
of Engineers

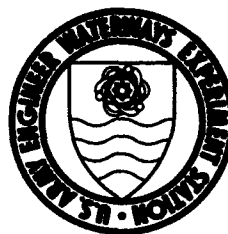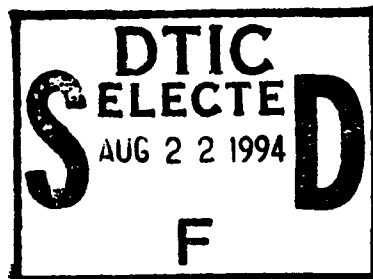AD-A283 529

DREDGING RESEARCH PROGRAM

CONTRACT REPORT DRP-94-5

CALCULATION OF MOVABLE BED FRICTION FACTORS

by

Palitha Nalin Wikramanayake, Ole Secher Madsen

Ralph M. Parsons Laboratory
Massachusetts Institute of Technology
Cambridge, Massachusetts 02139

DTIC
S ELECTE D
AUG 2 2 1994
F

August 1994
Final Report

Approved For Public Release; Distribution Is Unlimited

DTIC QUALITY INSPECTED 8

Prepared for **DEPARTMENT OF THE ARMY**
US Army Corps of Engineers
Washington, DC 20314-1000

Monitored by US Army Engineer Waterways Experiment Station
^909 Halls Ferry Road, Vicksburg, Mississippi 39180-6199

Under Work Unit 32463

94-26561
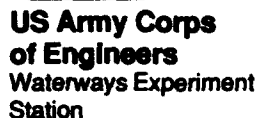
94 8 19 083

The contents of this report are not to be used for advertising, publication, or promotional *purposes*. Citation of trade names does not constitute an official endorsement or approval of the use of such commercial products.

Dredging Research Program
Report Summary

**US Army Corps
of Engineers**
Waterways Experiment
Station

Calculation of Movable Bed Friction Factors
(CR DRP-94-5)

ISSUE:

Much of the difficulty in obtaining accurate esti-
mates in simulating the movement of dredged
material disposed in open water results from lim-
ited understanding of water-sediment interaction
at the bed. Improvement in quantification of this
interaction requires intensive mathematical in-
vestigation into boundary layer mechanics.

RESEARCH:

When wind-generated waves propagate from
the deep ocean onto the continental shelf, they
begin to feel the effects of the bottom. These
bottom effects are accounted for as bottom
friction, which arises due to the no-slip flow
condition on the bottom. This condition gives
rise to a bottom shear stress and a thin boundary
layer where significant energy dissipation can
take place.

SUMMARY:

Laboratory experiments are outlined in this
report along with a brief description of the
methods involved in the model derivation.

The model is formulated in two stages:

● Deriving predictive relations for the ripple
geometry for a given bottom sediment and
a given wave condition.
● Developing a relationship between flow,
the ripple geometry, and the resulting fric-
tion factor.

The relation between the ripple geometry and
the roughness and the relationship between the
friction factor and the wave, sediment, and fluid
parameters are analyzed. Finally, simple rela-
tionships for the prediction of the roughness of a
movable bed under regular and irregular waves
are proposed, and numerical examples illustrat-
ing use of the relationships are given.

AVAILABILITY OF REPORT:

The report is available through the Interlibrary
Loan Service from the U.S. Army Engineer
Waterways Experiment Station (WES) Library,
telephone number (601) 634-2355. National
Technical Information Service (NTIS) report
numbers may be requested from WES Librarians.
To purchase a copy of this report, call NTIS at
(703) 487-4780.

Calculation of Movable Bed Friction Factors

by Palitha Nalin Wikramanayake, Ole Secher Madsen

Ralph M. Parsons Laboratory
Massachusetts Institute of Technology
Cambridge, MA   02139

Accesion For		
NTIS CRA&I		☑
DTIC TAB		☐
Unannounced		☐
Justification		
By		
Distribution /		
Availability Codes		
Dist	Avail and / or Special	
A-1		
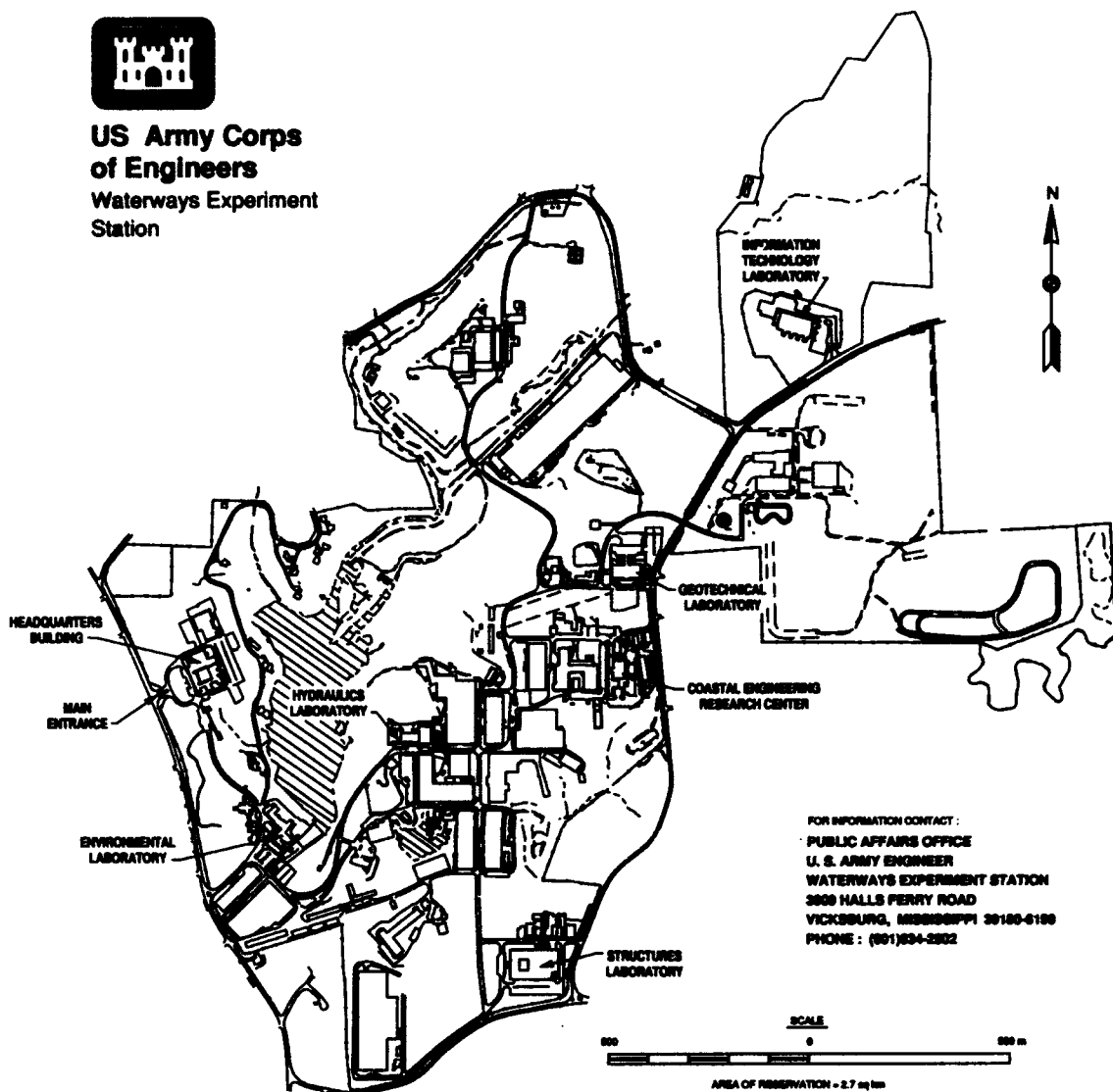
Final report

Prepared for   U.S. Army Corps of Engineers
Washington, DC   20314-1000

**US Army Corps
of Engineers**
Waterways Experiment
Station

PREFACE

SUMMARY

When wind-generated waves propagate from the deep ocean onto the continental shelf they begin to feel the effects of the bottom. These bottom effects are accounted for as bottom friction which arises due to the no-slip flow condition on the bottom. This condition gives rise to a bottom shear stress and a thin boundary layer where significant energy dissipation can take place.

The goal of this study was to develop a simple, physically realistic method to predict the friction factor over a movable sand bed under field conditions. Since reliable field measurements are available only for ripple geometry, laboratory data are used to derive the friction factor. Laboratory experiments are outlined in this report along with a brief description of the methods involved in the model derivation.

The model is formulated in two stages. The first involves deriving predictive relations for the ripple geometry for a given bottom sediment and a given wave condition. The second is the development of a relationship between flow, the ripple geometry, and the resulting friction factor. The relation between the ripple geometry and the roughness and the relationship between the friction factor and the wave, sediment, and fluid parameters is analyzed. Finally, simple relationships for the prediction of the roughness of a movable bed under regular and irregular waves are proposed and numerical examples illustrating use of the relationships are given.

1

CONTENTS

LIST OF TABLES

4

LIST OF FIGURES

5

PART I: INTRODUCTION

1. When wind generated waves propagate from the deep ocean onto the continental shelf they will begin to feel the effects of the bottom. The chief effects are shoaling, refraction, and bottom friction. The first two are commonly accounted for by assuming that there is inviscid flow all the way to the ocean bottom. Bottom friction, however, arises due to the no-slip condition at the bottom. This condition gives rise to a bottom shear stress and a thin boundary layer where significant energy dissipation can take place.

2. This energy dissipation results in a decrease in the wave height. Therefore in order to predict the wave height in coastal areas it is necessary to quatify the bottom shear stress. Another typical feature of coastal regions is the presence of steady currents induced by winds or tides. As discussed in the previous report (Madsen and Wikramanayake, 1990) the wave boundary layer causes the currents to experience an increased bottom resistance. Furthermore the wave motion at the bottom is usually strong enough to mobilize the bottom sediments, which in conjunction with a steady current can cause significant sediment transport.

3. It is obvious then that quantification of all these processes must be based on a good estimate of the bottom shear stress caused by the wave motion. Following the work of Kajiura (1964) and Jonsson (1966) this is done by relating the shear stress to the near-bottom wave velocity using a friction factor similar to that used in steady boundary layer flows. This friction factor can be calculated once the near-bottom Reynolds number and the relative roughness of the bottom are known. When the flow is fully rough turbulent, which is usually the case in most field scale flows, the friction factor is dependent only on the relative roughness of the bottom.

4. The relative roughness of the bottom is the ratio of the length scale of the wave orbital motion at the bottom to the length scale of the bottom roughness. A fundamental assumption of this approach is, in common with what is done for steady turbulent boundary layers, that the geometry of the bottom can be represented by a single length scale. While this is obviously an oversimplification for complex bottom geometry, it will be seen that the scatter in the experimental data is such that a more detailed

7

model of the bottom roughness cannot be justified.

5. Therefore when the bed geometry is known in advance, as in the case of a gravel bottom, a bottom roughness length can be estimated and the wave shear stress for a given wave motion can be calculated. In most coastal regions the bottom consists of cohesionless sediment--usually quartz sand--with diameters of the order of 0.2 mm. For a flat sediment bed the roughness could be expected to be comparable to the grain diameter.

6. However, wave attenuation measurements in the field, for example Iwagaki and Kakinuma (1963) and (1967), Treloar and Abernathy (1978), have resulted in values of the friction factor that are an order of magnitude higher than those that could be expected from a flat sediment bed. This is due to the presence of ripples and other bedforms on the bottom resulting in significantly greater resistance to the wave motion than from a plane bed.

7. The development of bed forms on beds of cohesionless sediment under the action of regular waves has been studied in detail under laboratory conditions. When an initially plane sediment bed is subjected to an increasing wave motion a point will be reached when the motion is just sufficient to move a few grains to and fro. This is referred to as initiation of motion. Further increase of the wave motion results in the formation of regular two-dimensional ripples with well-defined heights, lengths, and steepness. As the wave bottom orbital amplitude, which is the length scale of the wave motion, increases the ripple height and length increase while the steepness remains approximately constant.

8. Increase in the wave motion beyond a certain critical condition results in a decrease of the ripple steepness. Under these conditions the ripples are no longer regular and start to exhibit three-dimensional features. The ripple crests are more rounded than in the two-dimensional stage. This is due to ripples being overcome by the stronger wave motion. Still stronger wave motion results in the disappearance of the ripples. The bed is once again plane. However, under these conditions there is a mobile layer of sediment on the bed that follows the wave motion. This condition is known as sheet flow. At all stages of this process the exact geometry is found to depend on properties of the wave motion, the fluid and the sediments.

9. When bedforms are present it can be expected that the bottom roughness is scaled by their geometry and not by the grain diameter. Under sheetflow conditions there will be an increased friction due to the moving grains leading to an equivalent roughness scaled by the grain motion. Therefore it is seen that the roughness of a bed of cohesionless sediment is not a constant but is dependent on the wave, fluid, and sediment parameters.

10. Another important factor that must be considered when applying these ideas to field situations is that waves in the field are most often not regular and monochromatic. Instead, the coastal wave environment consists of a range of wave frequencies and amplitudes from many directions. Laboratory and field data suggest that bedforms under irregular waves can be significantly different from those obtained using regular waves. Still further complications arise when a steady current is present along with the waves. Current motions comparable to the wave motion can alter the geometry of the ripples and thus change their resistance to the wave motion.

11. In this report therefore an attempt is made to formulate a simple, physically realistic method to predict the equivalent roughness of a mobile bed under regular and irregular wave motion. The most recent laboratory and field data available on wave-formed ripple geometry and energy dissipation will be used. Extensions to cases for which no data are available will be suggested.

12. In Part II the concepts of bed roughness and the wave friction factor will be discussed. The derivation of the friction factor from experimental measurements will be outlined along with a brief description of the methods involved. The interaction between waves and a bed of cohesionless sediment will be reviewed in Part III. This will include the initiation of motion, ripple geometry and disappearance of ripples. The similarities and differences between results using regular and irregular laboratory waves and results from the field will be explored.

13. The available measurements of energy dissipation under wave motion will be utilized in Part IV to derive the equivalent bottom roughness due to bedforms. The relation between the ripple geometry and the equivalent roughness and the relationship between the friction factor and the wave,

sediment, and fluid parameters will be analyzed. Simple relationships for prediction of the roughness of a moveable bed under regular and irregular waves will be proposed.

14. Some numerical examples that illustrate the use the relationships proposed in Part IV will be given in Part V. A summary of the analysis and results of this report will be given in Part VI along with recommendations for future research.

PART II: THE WAVE FRICTION FACTOR AND THE EQUIVALENT BOTTOM ROUGHNESS

The Wave Friction Factor

15. The bed shear stress caused by steady flow over a horizontal bed has been studied for many years. Jonsson (1966), (1980a) and Jonsson and Carlsen (1976) applied the ideas developed for this case to the case of purely oscillatory flow over a flat bed by defining

$$\tau_{bm} = \frac{1}{2}\rho f_w u_{bm}^2 \tag{1}$$

where

τ_{bm} = Maximum bed shear stress due to the wave motion

ρ = Density of the fluid

f_w = Wave friction factor

u_{bm} = Maximum near-bottom velocity due to the wave motion.

16. Carrying the analogy further Jonsson used available experimental and theoretical knowledge to develop a friction factor diagram analogous to the Moody diagram used for steady pipe flow. In this diagram the flow is classified as belonging to the laminar, smooth turbulent, or rough turbulent regimes.

17. The friction factor for the laminar region is obtained by solving the linearized equations of motion for the wave boundary layer and is given by

$$f_w = \frac{2}{\sqrt{Re}} \tag{2}$$

where

$Re = \frac{u_{bm} A_b}{\nu}$ is the flow Reynolds number

ω = Radian frequency of the oscillatory motion

$A_b = \frac{u_{bm}}{\omega}$ is the bottom excursion amplitude

ν = kinematic viscosity of the fluid

18. In the smooth turbulent regime the flow is turbulent but still not affected by the properties of the bed. The friction factor depends only on the Reynolds number but the governing equations can no longer be solved exactly. For a given bed at high enough Reynolds numbers and large enough roughness scale the geometry of the bottom will affect the flow and after a transition region the flow will become rough turbulent. In rough turbulent flow--which is practically always the regime seen in the field--the friction factor is dependent only on the relative roughness of the b om.

19. The friction factor for the laminar and smooth turbulent regions is plotted in Figure 1 against the flow Reynolds number. For the purposes of this study the transition region will be ignored and the friction factor for a given bed will be taken as the greater of the value from Figure 1 or the value for fully rough turbulent flow, from equation (7), presented graphically in Figure 2.

Bed Roughness

20. In rough turbulent flow the roughness elements of the bed are not shielded by the viscous sub-layer and experience the full effect of the external flow. On a microscopic scale the bed shear stress is caused by the form drag and skin friction acting on individual roughness elements.

21. However at distances from the bed that are large compared to k_b, the physical size of the roughness elements, the effect of each element cannot be resolved. What is seen is a turbulent motion caused by many elements. At this distance therefore it is possible to define an average bottom shear stress. In steady flows it has been observed, Schlichting (1968), that in this region the flow velocity u can be represented by

$$u = \frac{u_*}{\kappa} \ln \frac{z}{z_0}$$ (3)

where

$u_* = \sqrt{\tau/\rho}$ is the shear velocity

κ = Von Karman's constant ($\kappa = 0.4$)

z_0 = a measure of the boundary roughness.
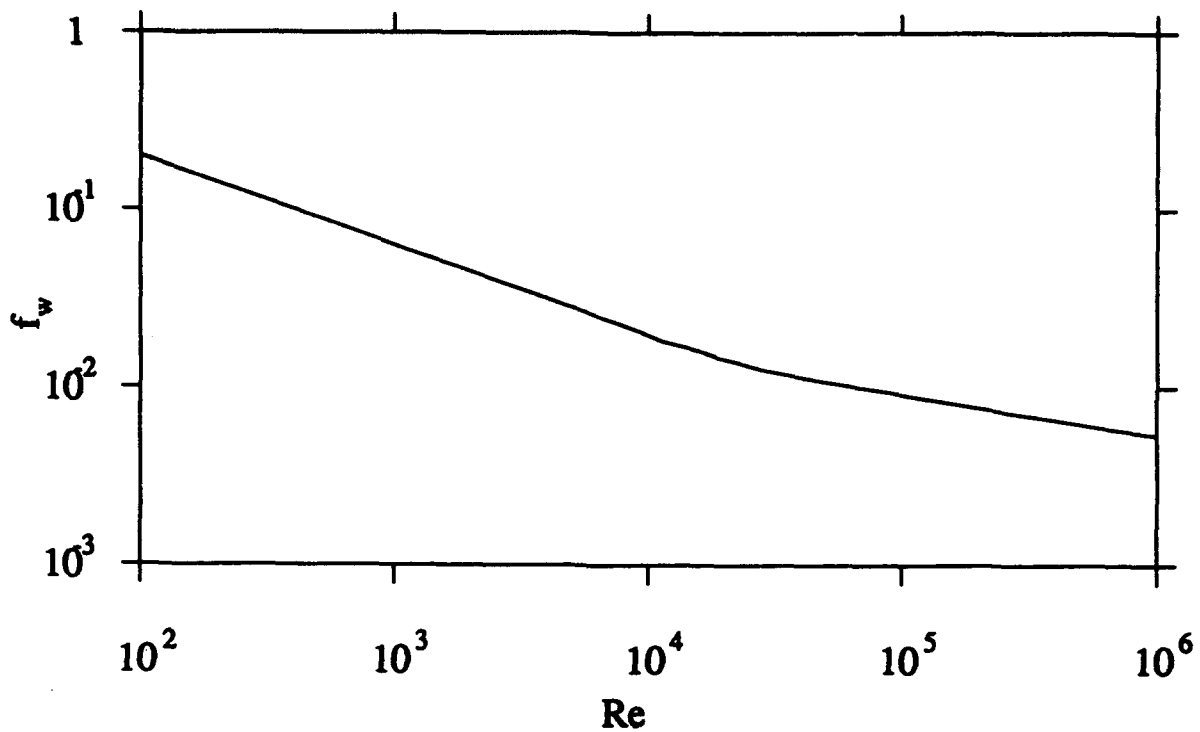
Figure 1. Friction factor for laminar and smooth turbulent flow from Jonsson (1966)
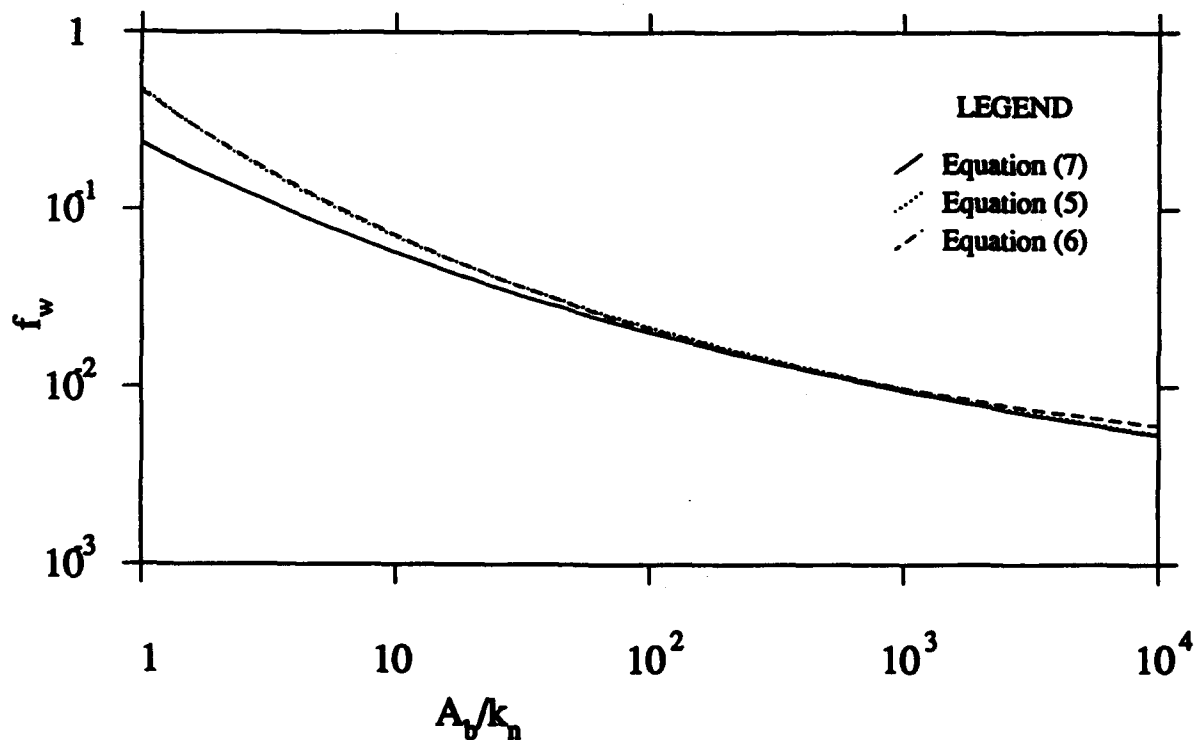
Figure 2. Friction factor equations for fully rough turbulent flow. Comparison of equations (5), (6), and (7).

22. In steady rough turbulent flow the degree of roughness of a surface is quantified by its equivalent Nikuradse sand grain roughness k_n. This is defined as the diameter of uniform sand grains that, when closely packed together, produce the same boundary resistance as the surface under consideration. From measurements of velocity profiles in the region where (3) holds it has been found that

$$z_0 = \frac{k_n}{30} \qquad (4)$$

23. This definition of the bottom roughness can be extended to any geometry that has sufficient regularity to allow the definition of the average shear stress. The exact value of this representative roughness must either be established by experiment or by extrapolation from results for similar geometries.

24. The relative roughness of a surface is then defined as the ratio of k_n and a length scale of the external flow. In steady flows this could be the flow depth or the lateral dimension of a closed conduit. In oscillatory flows the turbulence is confined to a thin boundary layer and the appropriate length scale is the excursion amplitude A_b.

25. Measurements of velocity profiles in oscillatory boundary layers, for example Jonsson and Carlsen (1976) and Jensen (1989), indicate that the velocity is logarithmic close to the bed for most parts of the wave cycle. This has lead to attempts to use the observed profiles along with equations (3) and (4) to calculate the shear velocity and the equivalent roughness as is done for steady flows.

26. Furthermore the use of z_0 as the height above the bed where the velocity vanishes is a widely used boundary condition in theoretical models. It should be pointed out that this is a purely conceptual extrapolation as equation (3) does not hold very near the bed. However, this method has been used quite successfully to relate the bottom roughness and the velocity profile in steady flows. It also has the advantage that it is a simple formulation. For these reasons the roughness concepts developed for steady turbulent flows have been used virtually unchanged in the analysis of oscillatory boundary layers.

Friction Factor Equations

27. Jonsson (1966) and Jonsson and Carlsen (1976) used a simplified approach to obtain a theoretical relationship between the friction factor and the relative roughness. The undetermined coefficient in this equation was found using two sets of velocity profile measurements in a wave boundary layer. The resulting implicit expression for f_w was

$$\frac{1}{4\sqrt{f_w}} + \log_{10}\left[\frac{1}{4\sqrt{f_w}}\right] = \log_{10}\left[\frac{A_b}{k_n}\right] - 0.08 \tag{5}$$

Swart (1977) proposed an approximation to equation (5) that was explicit in f_w as

$$f_w = \exp[5.213(A_b/k_n)^{-0.194} - 5.977] \tag{6}$$

28. Grant and Madsen (1979) used a linear eddy viscosity model to derive the equation

$$f_w = \frac{0.08}{ker^2 2\sqrt{\zeta_0} + kei^2 2\sqrt{\zeta_0}} \tag{7}$$

where ker and kei are the Kelvin functions of zeroth order,

$$\zeta_0 = \frac{k_n/30}{\kappa u_{*m}/\omega} \tag{8}$$

and u_{*m} is the shear velocity based on the maximum bottom shear stess $u_{*m} = \sqrt{\tau_{bm}/\rho} = \sqrt{f_w/2}u_{bm}$. In passing, it should be noted that equation (7) is, for all practical purposes, identical to the theoretical friction factor relationship derived by Madsen and Wikramanayake (1990).

29. The three equations (5), (6), and (7) are plotted in Figure 2 as graphs of friction factor against the relative roughness. It can be seen that all three curves lie quite close to each other showing that the theoretical and semi-empirical approaches lead to similar results.

30. It should be kept in mind that equations (5) and (7) are derived

assuming that the physical scale of the bed roughness k_b is much smaller than the boundary layer thickness. This condition is satisfied when A_b/k_b is large. Therefore the use of these equations at low values of A_b/k_n should be viewed as an extrapolation and not as a theoretical prediction.

31. In fact both Jonsson (1966) and Grant and Madsen (1982) propose that f_w be considered a constant when A_b/k_n is less than unity. This was based in part on the fact that the largest friction factor measured by Bagnold (1946) was 0.24. However since measurements on rippled sand beds give values as high as 0.5 we will not consider an upper limit for f_w in this study.

32. However, the problem of quantifying the equivalent roughness k_n for a particular bed remains unresolved. Two different friction factor relations, for example equations (5) and (6) above, could fit the same data equally well if the definition of k_n is adjusted. Riedel et al. (1972) published an extensive set of friction factor data for surfaces roughened with closely packed uniform sand grains. Grant (1975) found that equation (6) fit the data well if the bed roughness was set equal to the grain diameter.

Wave Friction and Energy Dissipation

33. The average energy dissipation per unit area in the wave boundary layer, E_d, was derived by Kajiura (1968) as

$$E_d = -\overline{\tau_b(t)u_b(t)} \tag{9}$$

where $\tau_b(t)$ and $u_b(t)$ are the instantaneous bed shear stress and near-bottom wave velocity, respectively, and the overbar denotes time averaging. Equation (9) can be evaluated only if the time variation of the bed shear stress is known.

34. Jonsson and Carlsen (1976) present data for a fixed, roughened bed indicating that the time variation of τ_b is of the form

$$\tau_b(t) = \tau_{bm}|\cos(\omega t+\varphi)|\cos(\omega t+\varphi) \tag{10}$$

16

when the bottom velocity is of the form $u_{bm}\cos(\omega t)$. ϕ is the phase lead of the shear stress with respect to the near-bottom velocity. For laminar flow ϕ will be 45 degrees while for turbulent flow it is expected to be somewhat less.

35. Lofquist (1986) has measured the instantaneous shear stress and the average energy dissipation over a rippled sand bed. His results show that the time variation of the shear stress can be very different from equation (10). The energy dissipation E_d can be related to the near-bottom velocity u_{bm} by an energy dissipation factor f_e defined by

$$E_d = \frac{2}{3\pi}\rho f_e u_{bm}^3 \tag{11}$$

36. It should be noted that a similar result with f_w replacing f_e can be obtained if the time variation in equation (10) and the definition of equation (1) are substituted into the right hand side of equation (9) with the phase lead ϕ taken to be zero. If a value of 20 degrees is assumed for the phase lead, which is the average value from the measurements of Lofquist (1986), it would lead to f_w being greater than f_e by about 6%.

37. Both f_w as defined from the maximum shear stress in equation (1) and f_e can be calculated from the data presented in Lofquist (1986). They are plotted against each other in Figure 3. It can be seen that except for a few points where f_w is much greater than f_e the two values are nearly equal with f_e being greater than f_w by about 5%. However this is a small difference when compared to the uncertainity in the measured values.

38. The fact that f_e is slightly greater than f_w indicates that the variation in equation (10) is not a good representation of the instantaneous shear stress. If the eddy viscosity model of Madsen et al. (1988) is used a sinusoidal variation of the bed shear stress would be obtained. If the energy dissipation is calculated from equation (9) with this variation along with a phase lead of 20 degrees f_e as defined by equation (11) is found to be greater than f_w by about 10%. This is an improvement over the result obtained using equation (10) and suggests that the sinusoidal shear stress variation is better than the variation suggested by equation (10).

39. Lofquist's experiments are described in greater detail in Appendix

17
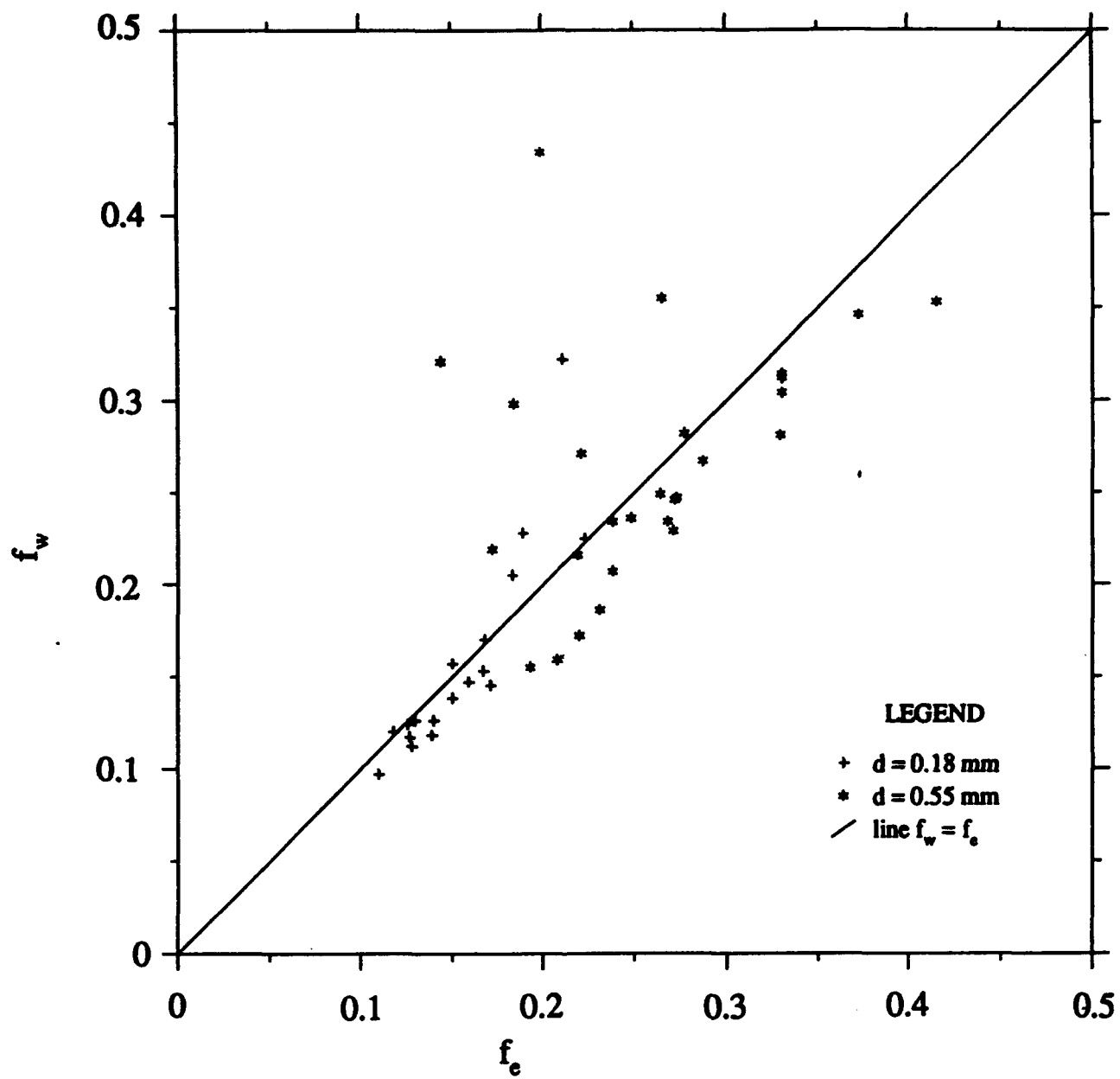
Figure 3. Comparison of the values of f_e and f_w derived from the measurements of Lofquist (1986)

18

A. On closer examination of the conditions it is seen that f_w is much greater than f_e when the ripple length is longest and therefore the number of ripples in the test section is the least. Under these conditions the effect of the end conditions can be expected to have the greatest effect. Therefore it seems reasonable to disregard these points and to consider that f_w as defined by equation (1) and f_e as defined by equation (11) are identical for rippled sand beds.

Experimental Determination of the Friction Factor

40. The friction factor has been determined from laboratory and field measurements by three main methods, one direct and two indirect. The direct method is to measure the bed shear stress due to the wave motion using a device such as a shear plate. Then the friction factor can be calculated directly from equation (1). This is the method used by Riedel et al. (1972) for fixed beds roughened by sand grains. However, this method would not be suitable for movable sand beds.

41. One of the indirect methods is through measurements of the velocity profile in the wave boundary layer. This is the method used by Jonsson and Carlsen (1976) for a fixed bed. They obtained the shear stress in two ways. One was by numerical integration of the equation of motion using the velocity measurements at various phases, while the other was through the use of equation (3) applied to the near-bed portion of the velocity profile.

42. Both these methods have the disadvantage that the velocity profile at various phases of the external flow must be measured. This is likely to be a difficult task on rippled sand beds. Furthermore even if this is done the first method requires the calculation of the rate of change of velocity with time at all levels. The accurate calculation of these gradients is a difficult task. The second method involves fixing a theoretical bed level in order to obtain a logarithmic velocity profile and also the question of how far this region is assumed to extend.

43. The other indirect method of obtaining the friction factor is through measurements of the energy dissipation caused by the wave boundary layer. This has been done by measuring the wave attenuation in a wave

19

flume and by measuring the energy input needed to maintain the wave motion in a wave tunnel or an oscillating bed. This seems the only practicable method for movable sand beds.

44. Once the energy dissipation is calculated it is, however, necessary to assume a relation between this value and the shear stress. Jonsson (1966) has argued that this is not possible because of the need to know the time variation of the shear stress and the phase lead with respect to the external motion. However, as discussed in the previous section, the data of Lofquist (1986) show that for rippled sand beds under a wide range of wave conditions the friction factor can be taken equal to f_e as defined in equation (11).

45. Therefore in this report we will consider only those data sets where the energy dissipation has been measured. This allows f_e to be determined unambiguously. The predictive relations proposed in later sections will be correct for f_e and therefore appropriate for applications, such as predicting wave height attenuation, where the energy dissipation is needed. Their use in applications which require the bottom shear stress depend on the assumptions made above. In the remainder of the report f_w and f_e will be used interchangeably and considered to represent the same value

The Roughness of a Movable Bed

46. In the discussion following equation (3) it was stated that for fixed sand roughened beds the bed roughness was found to be of the order of the grain diameter. In Figure 4 calculated values of the friction factor from the data of Carstens et al. (1969) are plotted against the ratio A_b/d. Also shown in the figure are two theoretical curves. One is equation (7) with $k_n = d$ as suggested by Grant (1975) while the other is equation (6) with $k_n = 2.5d$ as suggested by Nielsen (1983).

47. The data points obtained from a rippled bed are for stable ripples with a grain diameter of 0.297 mm. The points obtained from a flat bed are under conditions for which the flat bed is unstable indicating that there must have been considerable sediment motion on the bottom. It can be seen that the friction factors obtained from the rippled bed are an order of
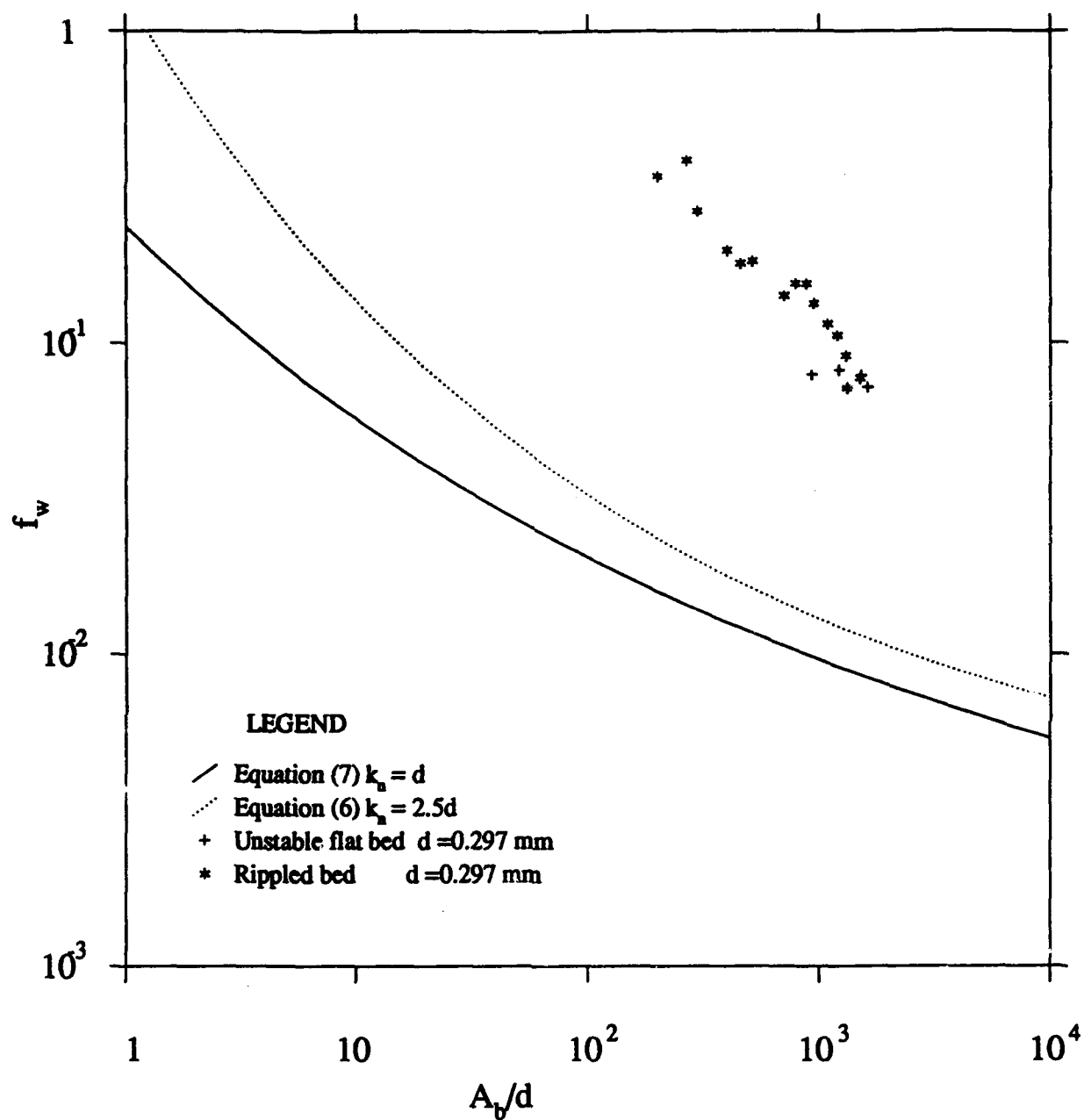
Figure 4. Measured friction factors for rippled beds and unstable flat beds along with the friction factor relations proposed by Grant and Madsen (1979) and Nielsen (1983) for flat sand beds

21

magnitude higher than the values that would be predicted from the theoretical equations assuming a flat bed. The points obtained with an unstable flat bed also plot well above the theoretical curves.

48. This discrepancy shows very clearly that the grain diameter is not the appropriate roughness scale both when the bed is rippled and when there is significant sediment motion on the bottom. Therefore, if the use of friction factor relations such as equations (6) and (7) is to be extended to movable beds it is necessary to propose new roughness scales for use in conditions where the flat sand bed is not stable.

49. These scales can be found by relating the observed roughness to the ripple geometry and the wave and sediment parameters. It should be emphasized here that it is the energy dissipation that is measured in the experiments. The roughness must then be calculated from one of the friction factor equations given above. Therefore in order to be consistent it is important that the same equation be used when predicting the friction factor after having predicted the roughness.

50. This means that as far as predicting the friction factor from the analysis of the energy dissipation measurements is concerned it does not matter which equation is used provided the method is consistent. In this report we will use equation (7) which was suggested by Grant and Madsen (1979) without any modification for low values of A_b/k_n.

51. Using this equation a value of A_b/k_n can be found for every measured value of the friction factor. Since A_b is known from the experimental conditions this means that the equivalent roughness as defined in this chapter is known. It is hoped that an analysis of these values will lead to relations that can predict the equivalent roughness given the ripple geometry and other parameters.

52. The method outlined above still requires the prediction of the ripple geometry as this is also dependent upon the wave and sediment parameters. It would appear that it is much simpler to predict the friction factor directly from the wave and sediment parameters without considering the ripples at all. A formula of this type has been proposed by Vongvisessomjai (1987, 1988) and Madsen et al. (1990).

53. However, this kind of direct formula is based solely on data from laboratory experiments. It will be shown in Part III that the ripple

geometry seen in the field under irregular waves is quite different from those seen under regular waves in the laboratory. Therefore it is necessary to investigate the connection between ripple geometry and the friction factor in order to propose a predictive relation that can be used under field conditions. This will be done in Part IV.

54. The effect of an applied wave motion on a movable bed composed of cohesionless sand grains is examined in this section. Experimental data on the initiation of motion, geometry of ripples, and the transition to sheet flow will be analyzed in order to propose predictive relations that describe these phenomena.

55. Since there has already been a considerable amount of work done regarding the effect of regular waves on sand beds, for example by Stefanick (1979) and Nielsen (1979), this aspect will not be investigated in detail. Instead the objective of this chapter will be to see how well existing ideas for regular waves can be applied to data from laboratory experiments with irregular waves and from field measurements.

Quantification of the Problem and Non-dimensional Variables

56. The physical problem considered is the response of a bed of cohesionless grains forced by the oscillatory motion of the fluid above it. This study is restricted to the behaviour of sand grains in water. It is assumed that the sand grains are specified by one linear dimension such as their mean diameter, d, and by the density of the grain material ρ_s. The relevant parameters for the water are its density ρ and its kinematic viscosity ν. Since the problem involves the suspension of the sand grains the acceleration due to gravity must also be considered.

57. The oscillatory motion is assumed to be fully specified by its bottom orbital amplitude A_b and its radian frequency ω. This assumption implies that this is entirely a bottom phenomena with no effect of the flow depth. While this is the case in the field, where the bottom boundary layer is only a small fraction of the depth, it will be seen that it is not always true for laboratory experiments.

58. It is expected that any aspect of the interaction can be described by the seven parameters A_b, ω, ρ, ν, d, ρ_s, and g. Since these parameters have three dimensions it follows that any feature expressed in non-dimensional form is a function of four independent non-dimensional parameters. Many different parameters have been proposed by various

24

authors. Some of these have physical significance, e.g., expressing the ratio of two forces on the grains, while others are used on the empirical grounds that they improve the correlation of the data.

59. An obvious non-dimensional parameter is the specific weight of the sand, s, defined as

$$s = \frac{\rho_s}{\rho}$$ (12)

For quartz sand this value is close to 2.65.

60. Most of the laboratory experiments have been conducted at room temperature which means that the viscosity was not varied over a large range. A convenient non-dimensional parameter that includes the viscosity is S_* introduced by Madsen and Grant (1976) and defined by

$$S_* = \frac{d\sqrt{(s-1)gd}}{4\nu}$$ (13)

which has the advantage that it includes only fluid and sediment parameters. Other parameters that include the viscosity have been suggested, e.g., the friction Reynolds number Re_* which is defined by

$$Re_* = \frac{u_* d}{\nu}$$ (14)

or the flow Reynolds number Re defined by equation (2). The parameter Re_* determines whether the flow over a flat sand bed is smooth or rough turbulent.

61. The effect of varying the viscosity on the ripple geometry has not been investigated in detail. Mogridge and Kamphuis (1972) conducted experiments at 6°C and 22°C and concluded that there was no significant difference in the ripple geometry over this range of temperatures. However, Stefanick (1979) and Grant and Madsen (1982) found S_* to be a useful parameter in describing ripple geometry.

62. The oscillatory boundary layer over rippled beds has been observed to be fully rough turbulent. Thus it may be argued that viscosity is not an important factor in this problem. However, the problem also involves

25

the motion of sand grains through the water, an aspect that is affected by
viscosity. Therefore S_* will be considered in the analysis of ripple
geometry. For the problem of water at room temperature over a sand bed S_*
will depend only on the grain diameter.

63. The remaining non-dimensional parameters will involve the wave
motion. One that is often used is the Shields parameter ψ, defined by

$$\psi = \frac{\frac{1}{2}f_w'u_{bm}^2}{(s-1)gd}$$

(15)

where f_w' is the friction factor for a flat sand bed. As mentioned in Part
II this is taken as the greater of the value obtained for laminar or smooth
turbulent flow from Figure 1 or the value obtained for rough turbulent flow
from equation (7) with $k_n = d$. This parameter is proportional to the ratio
between the surface shear stress on a flat bed, which tends to mobilise the
sediment, and the submerged weight of the grains, which tends to oppose
grain motion.

64. A second parameter that involves the wave motion is the
acceleration parameter A_* which is defined as

$$A_* = \frac{A_b\omega^2}{(s-1)g}$$

(16)

This is the ratio of the inertial force on the grain due to the fluid
motion to the downward force due to gravity. It should be noted that while
s has been defined as a separate parameter it is also used in the
definitions of S_*, ψ, and A_*. This is done in order to give these three
parameters some physical meaning.

65. The most commonly measured characteristics of ripples are the
ripple length, λ, and η the height of the ripple measured from crest to
trough. These values are usually made non-dimensional by dividing by the
grain diameter, d, or the orbital amplitude A_b. Another important non-
dimensional ripple parameter is the ripple steepness η/λ.

Representation of Irregular Waves

66. In the previous section it was assumed that the near-bottom orbital amplitude and the radian frequency were sufficient to specify the wave motion. These parameters are uniquely determined in the case of regular waves. However, waves in the field, even when they are in the same direction, are practically always irregular with a range of heights and periods.

67. Therefore in order to apply the ideas and results obtained from the analysis of ripples caused by regular waves to the field it is necessary to specify the field wave condition in terms of an equivalent wave height and period. The expectation is that it would be possible to find an equivalent representation that would lead to the same relations being applicable for the ripples caused by both regular and irregular waves.

68. Irregular waves are usually observed by obtaining a continuous record of the displacement of the water surface. One way of specifying an equivalent wave from this record is to take the root-mean-square wave height, H_{rms}, and the average wave period. However, it is known that for many wave processes, such as breaking, it is the higher waves that are the most significant. This has led to the significant wave height and period being used to specify irregular waves. These are defined as the average height and period of the highest one third of all the waves in the record. If the wave heights are Rayleigh distributed it can be shown that the significant wave height is equal to $\sqrt{2}H_{rms}$. The significant wave period is usually nearly equal to the average wave period.

69. A more complete way of representing random waves is through the wave spectrum. The spectrum gives the distribution of wave energy with the frequency. The energy, E_n contained in the range $\omega_n \pm \Delta\omega/2$ is given by

$$E_n = \rho g S_\eta(\omega_n)\Delta\omega \qquad (17)$$

where $S_\eta(\omega)$ is the surface amplitude spectrum.

70. Madsen et al. (1988) using a simple eddy viscosity model and the

linearized bottom boundary layer equations obtained the spectral energy
dissipation using a friction factor obtained from an equivalent
monochromatic wave. This wave was defined to have the same root-mean-
square bottom orbital velocity and amplitude as the specified wave
spectrum.

71. The equivalent bottom velocity u_{br} was defined by

$$u_{br}^2 = 2 \int_0^\infty S_{ub}(\omega) \, d\omega \tag{18}$$

where S_{ub} is the spectrum of the near-bottom orbital velocity and is given
by

$$S_{ub}(\omega) = \left[\frac{\omega}{\sinh kh}\right]^2 S_\eta(\omega) \tag{19}$$

72. The equivalent bottom orbital amplitude, A_{br}, was defined as

$$A_{br}^2 = 2 \int_0^\infty \frac{S_{ub}(\omega)}{\omega^2} \, d\omega \tag{20}$$

and the equivalent radian frequency ω_r can be found from

$$\omega_r = \frac{u_{br}}{A_{br}} \tag{21}$$

73. It should be noted that in the above method the spectrum of the
bottom velocity is used to calculate the equivalent quantities. If an
equivalent surface wave representation, such as H_{rms}, is given, only the
wave number of this equivalent wave would be used to transfer the surface
quantities to the bottom. Thus it can be expected that the method of
Madsen et al. (1988) will provide a more realistic representation when the
spectrum is broad for intermediate waves.

74. Sato (1988) conducted experiments on ripple generation by
irregular waves in a wave tunnel. He developed his wave signal by
generating a surface displacement record based on an empirical spectrum and

28

transformed it into a bottom velocity record using linear theory. This signal was then fed to the wave tunnel piston. He then obtained a "significant" bottom velocity and period by considering the highest one third of the bottom velocity fluctuations. These values were used as representative of the irregular motion.

75. Since ripple formation is a bottom process it would appear that both these methods, which are based on the bottom velocity rather than the surface displacement, are superior to the use of the significant height and period. The disadvantage of these methods is that they require either the wave spectrum or a detailed record of the surface fluctuation. This type of information is rarely reported. In particular, all the existing field measurements of wave-formed ripples provide only an equivalent surface wave to describe the wave conditions.

76. This equivalent surface wave is either the significant wave height, $H_{1/3}$, or the root-mean-square wave height H_{rms}. Measurements given in one form can be converted to the other by assuming that the wave heights are Rayleigh distributed, a condition that is approximately satisfied in the field (Goda, 1985). $H_{1/3}$ is a traditional parameter used in applications such as wave forecasting. It was also suggested that using $H_{1/3}$ would result in a closer correspondence between ripples observed in the field and in the laboratory. However, Nielsen (1979, 1981) concluded that the results were not comparable even when $H_{1/3}$ was used.

77. The root-mean-square wave height of a train of irregular waves bears the same relationship to the total wave energy as the wave height of a train of regular waves. This makes it a more meaningful parameter with respect to the present study which is concerned with energy dissipation. It is found in Part IV that the use of H_{rms} results in a bed roughness and friction factor obtained from irregular wave experiments being similar to those seen with regular waves. Therefore H_{rms} and the average period will be used to represent irregular waves in the analysis presented here.

78. The near-bottom orbital amplitude is then obtained from the equation

$$A_{brms} = \frac{\frac{1}{2}H_{rms}}{\sinh(kh)} \qquad (22)$$

29

where h is the depth and k the wave number corresponding to the average period.

Experimental Methods and Conditions

Laboratory Experiments

79. The response of a movable sand bed to an imposed wave motion has been studied in the laboratory using three different apparatus. They are the oscillating bed, the wave flume and the wave tunnel. Each apparatus has its own advantages and disadvantages.

80. In the oscillating bed the sediment is placed on a movable tray which is oscillated in still water. The biggest disadvantage here is that since the grains are in motion here they will experience an additional acceleration force that would not be present in the prototype case. Madsen and Grant (1976a) and Nielsen (1979) analyze this difference and find that while the additional force is negligible up to the initiation of motion it is significant for flows strong enough to generate ripples.

81. This is supported by the experimental results obtained using this apparatus. Analysis by Vongvissesomjai (1984) shows that the ripple geometry is significantly different from the geometries obtained from wave flumes and tunnels. Therefore ripple data from oscillating beds will not be considered in this study.

82. In a wave flume waves are generated at one end, run over a sand bed, and break on an absorber beach at the other end. This apparatus has the advantages of a length very much larger than the ripple length and a depth that is large compared to the ripple height. The disadvantages of most wave flume experiments are that waves of prototype scale can not be generated due to the limited scale of the flume, e.g., waves in most facilities are limited to periods of 1-3 seconds. Another problem is that reflection from the beach can distort the wave field in the flume.

83. Wave tunnels are closed conduits with no free surface. The water in the tunnel is oscillated by a piston or some similar device at one end. Thus it is possible to obtain prototype scale flows with large velocities and periods. Another advantage is that the piston produces the bottom velocity directly whereas in the wave flume this must be calculated from

the observed surface displacement. Therefore with a wave tunnel it is possible to produce any kind of near-bottom flow.

84. Due to these factors the wave tunnel is probably the best apparatus in which to study the movable bed problem. Nevertheless some drawbacks imposed by the relatively small size of these devices should be kept in mind. The chief problem is that the height of the tunnel is often not large compared to the ripple height.

85. For example in the experiments conducted by Carstens et al. (1969) ripples of height 7 cm were measured in a tunnel that was 30.5 cm high. However the bottom velocity was calculated neglecting the ripples. Similarly, Sato (1988) measured ripples of height 5 cm in a tunnel 21 cm high. When the ripple height is such a large fraction of the tunnel height the flow field will not be the same as the prototype where the depth is assumed to be much larger than the ripple height. Another problem is caused by the limited length of the test section. In the measurements of Carstens et al. there were sometimes as few as six ripples on the sand bed. In this situation end effects may have a significant effect on ripple geometry.

86. The discussion above has shown that both wave flumes and wave tunnels have their drawbacks. These, together with differences in scale and the shape of sand grains contribute to the large scatter seen in the data on ripple geometry.

Field Measurements

87. There have been only a few field studies in which simultaneous measurements of ripples and the ambient wave conditions have been made. The obvious reason for this is that these field measurements are difficult to carry out, especially in deep water and under strong wave motions.

88. Inman (1957) published the first detailed field study. The ripple geometry was measured in water depths of up to 30 m by divers. The wave motion was recorded by a fathometer on a boat above the study site. Nielsen (1984) recorded ripple geometry in the near-shore region at depths of 1 to 2 m. He measured ripples under both breaking and non-breaking waves. Only the ripples formed by non-breaking waves are considered in this study. The wave conditions were measured using a pressure gauge placed on the bottom. Miller and Komar (1980b) measured ripples in water

depths of up to 30 m and measured the waves with a pressure gauge. However, they did not report the ripple heights as satisfactory measurement was not possible.

89. Field measurements are open to criticism on a number of fronts. Firstly, there is the question of whether the observed ripples are due to the ambient waves or whether they were established by some previous wave condition. All three of the studies reported above were carried out when there were fairly constant wave conditions with sediment motion on the bottom. This provides some basis for the belief that the ripples are due to the prevailing wave conditions.

90. Other problems are that in the field the waves could be from any direction and the effect of any steady currents that may be present. These drawbacks can be overcome by careful selection of the field sites. Furthermore the measurements, particularly of the ripple height, are likely to involve significant errors.

91. Despite all these sources of error, field observations can be carried out under conditions that are not obtainable with laboratory equipment. In addition since the ultimate aim of the analysis of ripple geometry is to make predictions in the field it is only logical that the laboratory results be compared with the field data.

Initiation of Motion

92. Since the formation of ripples from a flat bed requires the motion of the sand grains it is logical to first consider the flow conditions under which the grains first move. There are many criteria proposed for the initiation of motion in the literature. A review is given by Sleath (1984). Of these the most generally accepted criterion is the Shields curve.

93. The Shields parameter was first used to describe the initiation of motion in steady flows. It was shown by Madsen and Grant (1976b) that when the Shields parameter, ψ, was defined as in equation (14), i.e., using the grain diameter as the bed roughness scale, the Shields curve could also be used to describe the initiation of motion for unsteady flows. The critical value of ψ for the initiation of motion, ψ_c, is plotted against S_* in Figure

5 which is the modified Shields diagram as presented by Madsen and Grant.

94. The figure shows the curve that is drawn through the data points obtained from steady flow experiments. The initiation data from oscillatory flow is plotted along with this curve in Figure 1 of Madsen and Grant (1976b). It can be seen in that figure that the data do not show the minimum of the curve very well and for values of S_* greater than about 8 a straight line of ψ_c = 0.55 will fit the data well. However, the data do ·show an increase in ψ_c for S_* less than 8--which corresponds to sand grains of diameter 0.4 mm for room temperature. This effect.is due to the viscous sub-layer, which is present for these small diameters, shielding the grains from the turbulence of the outer flow.

95. The data used by Madsen and Grant (1976b) were obtained from materials with a wide range of specific gravities. That these data plot in the same region of the Shields diagram indicates that the effects of s are well described by including it in the definition of ψ. Furthermore the analysis indicated no significant effect of the acceleration parameter A_*. This means that the initiation of motion, which should in theory depend on four non-dimensional parameters, is quite well described by just two parameters.

96. It should be kept in mind that the definition of the initiation of motion is a very subjective one and may explain the large scatter of the data points around the curve. Mathisen (1989) defined three criteria-- grain motion at irregularities, propagation of bedforms, and grain motion on an initially flattened bed. He found that while the first two criteria corresponded quite well with the Shields curve the third criteria was met only at values of ψ significantly higher than ψ_c.

97. This is because these experiments were conducted in a wave flume with sand grains of diameter 0.12 mm. For these conditions the boundary layer was laminar, making the initiation of motion more difficult. In any event since sand beds in the field will have some irregularities the first criterion is the important one. The fact that bedform propagation occurs at slightly higher values of ψ means that ripple formation will begin soon after the initiation of motion.

98. Initiation of motion under combined steady and oscillatory flow was studied by Lee-Young and Sleath (1988) by oscillating a sediment bed at

33
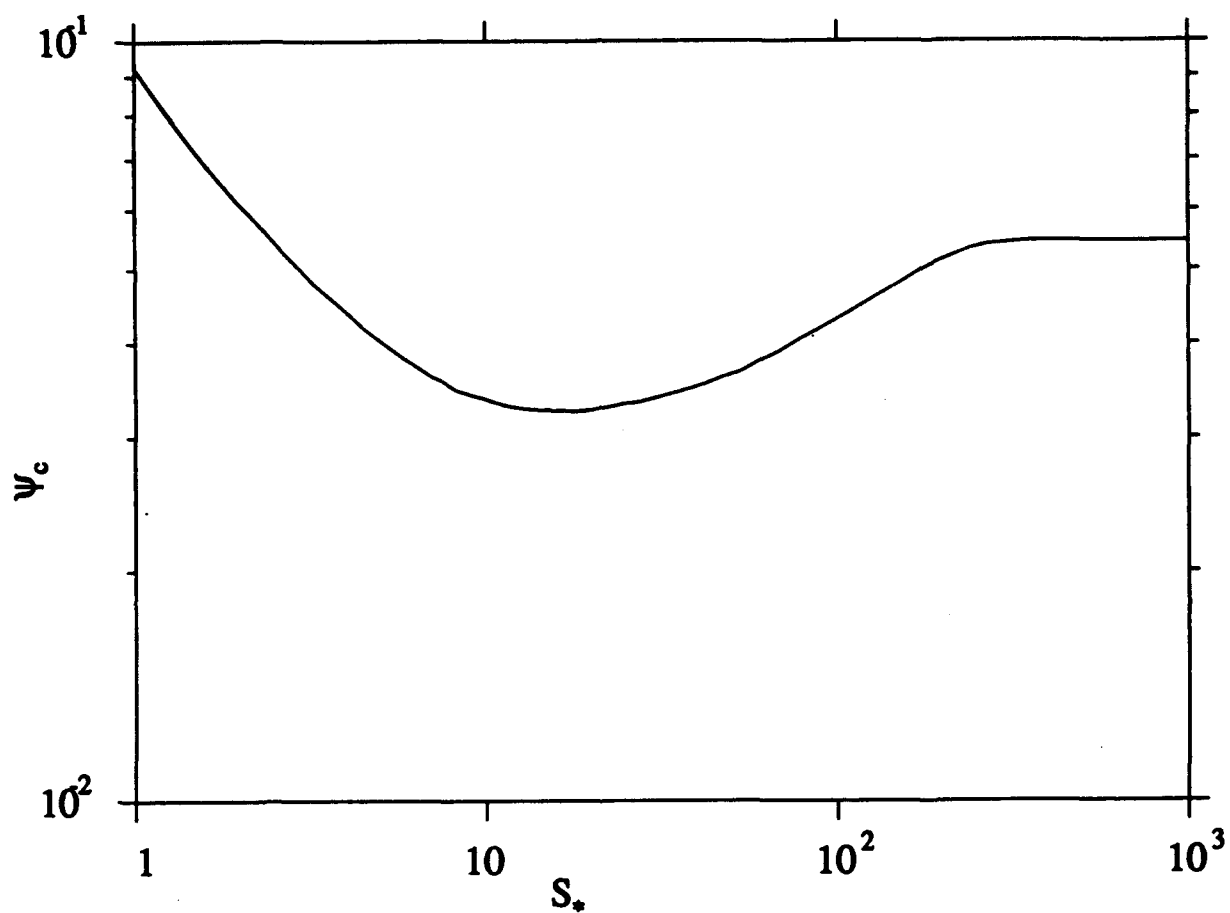
Figure 5. The Shields curve: critical Shields parameter for the initiation of motion, ψ_c, against S_*.

right angles to a steady current. It was found that the Shields curve predicted the initiation well when the bed shear stress was calculated as the vector sum of the current shear stress and the wave shear stress.

99. A field study on ripple generation in a depth of 22 m was reported by Amos et al. (1988). The bottom velocity and bed conditions were measured by an instrument package deployed on the bottom. The data show that ripples were observed well below the critical value of the Shields parameter.

100. However, examination of their Figure 6 shows that these ripples were characterized as poorly developed ripples with rounded crests and evidence of biodegradation. Thus it is likely that these are ripples that were created by earlier wave conditions. It is significant that none of what they refer to as well developed ripples lie below the Shields curve.

101. Thus it appears that existing data on initiation of motion under waves supports the use of the Shields curve as a criterion. Therefore this curve will be adopted as marking the lower limit of ripple formation. When ψ is greater than ψ_c then it will be assumed that the bed is rippled with the geometry to be found from the relations proposed in the next section.

Geometry of Wave-generated Ripples

102. The ripple data to be used in this study, from regular and irregular wave laboratory experiments and from field measurements, are summarized in Tables 1, 2, and 3 respectively. All these data are tabulated in Appendix A.

103. A preliminary analysis indicated that there were no significant differences between data from wave flumes and wave tunnels. It should be noted that the laboratory experiments cover the same range of sediment sizes observed in the field. However, only a few experiments have been conducted in the range of periods observed in the field.

104. The geometry of wave-generated sand ripples has been analyzed by many authors. In most of these analyses the objective has been to find the non-dimensional parameter that best correlated the data on a ripple parameter such as the steepness. A curve fit through the data was then proposed as a predictive relation.

Table 1

Summary of Available Ripple Data from Laboratory Experiments
with Regular Waves

Source of data	Diameter of sand (mm)	Range of periods (s)	Type of apparatus	Number of data points
Mathisen (1989)	0.12	2.6	WF	6
Sato (1988)	0.18	1-7	WT	12
	0.56	1.5-5	WT	10
Rosengaus (1987)	0.20	2.2-3	WF	9
Lambie (1984)	0.09	2.3-7.5	WT	20
	0.15	2.7-7.2	WT	27
Miller & Komar (1980)	0.178	3-5	WF	4
Nielsen (1979)	0.082	1.0-1.7	WF	24
	0.17	1.7	WF	10
	0.36	1.7	WF	10
Lofquist (1978)	0.18	3-8	WT	6
	0.55	2.5-12	WT	23
Mogridge & Kamphuis (1972)	0.36	1-2.5	WF	50
	0.36	2.5-14	WT	21
Carstens et al. (1969)	0.19	~3.53	WT	6
	0.297	~3.53	WT	17
	0.585	~3.53	WT	19
Kennedy & Falcon (1965)	0.095	1.07-2.34	WF	4
	0.32	1.39-1.57	WF	6
Inman & Bowen (1963)	0.2	1.4-2	WF	2

WT: wave tunnel   WF: wave flume

Table 2

Summary of Available Ripple Data from Laboratory Experiments
Using Irregular Waves

Source of data	Diameter of sand (mm)	Range of significant period (s)	Type of apparatus	Number of data points
Mathisen (1989)	0.12	~2.5	WF	9
	0.2	~2.5	WF	3
Sato (1988)	0.18	3-5	WT	21
	0.56	1.5-3	WT	13
Rosengaus (1987)	0.2	~2.5	WF	8

WT: wave tunnel   WF: wave flume

Table 3

Summary of Available Ripple Data from Field Measurements

Source of data	Range of grain diameters (mm)	Range of significant period (s)	Number of data points
Nielsen (1984)	0.11-0.62	5.7-12.9	39
Miller and Komar (1980)*	0.165-0.287	6-18.1	33
Inman (1957)	0.081-0.635	5-16	53

*Ripple wavelength only

105. Since it was shown earlier that the ripple geometry must depend on
at least four non-dimensional parameters this approach may seem
oversimplified. However, as shown in the previous section, it was found
that the initiation of motion could be described by two parameters (ψ and
S_*) with only a weak dependence on one (S_*). Furthermore, the variation in
the results from different experimental facilities is so great that a more
sophisticated approach involving more than two parameters does not appear
warranted.

106. Therefore, this approach will be adopted in the remainder of this
section in the analysis of ripple wavelength, height, and steepness. The
data from regular and irregular waves will be analyzed together for the
purpose of comparison. Before the analysis a brief description of the
mechanism of ripple formation will be given.

Ripple formation and disappearance

107. **Regular Waves.** It has been observed by Rosengaus (1987) and
Mathisen (1989) that grain motion begins at bed irregularities. The
process of ripple development from an initial irregularity has been
described in detail by Nielsen (1979) and Rosengaus (1987).

108. Initially, before the flow separates at the crest of the
irregularity, the jet flow down the side will tend to create a depression
in front and pile up sand in a hump beyond it. When the flow separates at
the crest a lee vortex is formed which acts to entrain sand from the lee
side and build up the original crest while making the trough deeper.

109. This mechanism acts on both sides of the original ripple creating
two new ones which in turn act as "originator" ripples. While the patch of
ripples thus formed spreads outwards the wavelength and height of the
ripples adjust until they reach an equilibrium.

110. For moderate flow intensities the result is a set of regular,
sharp-crested, two-dimensional ripples. The equilibrium height is the
balance between erosion of the crest by the flow over it and crest build-up
caused by the lee vortices.

111. As the flow intensity increases the ripple height and length
increase while the steepness remains essentially constant. The steepest
sections of the ripples have been observed to have slopes approximately
equal to the angle of repose of the bed material in water.

112. At higher flow intensities the lee vortices are not strong enough to maintain the crest leading to a decrease in steepness. The wavelength remains about the same while the ripple height decreases. The crests are more rounded and the ripples become three dimensional. The ripple ensions are also more variable.

113. Finally when the flow is sufficiently intense the ripples disappear altogether. The bed is essentially flat. However, the strong oscillatory motion causes a layer of sand grains to move to and fro on the bed. This is referred to as sheet flow.

114. <u>Irregular waves.</u> The above description was based on regular waves in the laboratory. The only description of the behavior of a bed under irregular field waves is given by Dingler and Inman (1976). They obtained instantaneous records of the bed profile using a high-resolution sonar.

115. Their results show that under strong irregular wave motion the bed can go from equilibrium ripples to a flat bed to developing ripples and back to a flat bed in a few minutes. This demonstrates the uncertainty that is present when it is attempted to apply observations made in small-scale laboratory experiments to the field.

116. Laboratory experiments with irregular waves were made by Rosengaus (1987), Mathisen (1989), and Sato (1988). Rosengaus and Mathisen did ripple measurements at moderate flow conditions and obtained ripple dimensions that were statistically steady. Sato (1988) increased the flow intensity up to sheet flow. He found that the ripple dimensions varied by about 10% during the run.

117. The variability between successive waves in Sato's wave record is about the same as in the wave record given by Dingler and Inman (1976). However, the longest period used by Sato was 5 seconds while the large waves measured by Dingler and Inman had periods of 10-12 seconds. This is probably the reason why Sato (1988) did not observe a flat bed during the run.

118. Mathisen (1989) found that even under moderate wave conditions the ripples under irregular waves were more variable than ripples formed by regular waves of a comparable intensity. A detailed analysis showed that while the differences in commonly measured characteristics, such as the ripple steepness, were small, ripples under irregular waves had crests that

were more rounded than ripples formed by regular waves.

119. These observations indicate that ripples formed by irregular field waves may be different from those observed in the laboratory under regular waves. Therefore the data on geometry of ripples formed by regular and irregular laboratory waves and by waves in the field will be compared in the next three sections to examine what differences, if any, are present.

Ripple wavelength

120. The ripple length, unlike the ripple height and steepness, is not generally regarded as being significant when estimating the equivalent roughness of a rippled bed. However, the analysis of this parameter may bring out the connection, or lack thereof, between laboratory and field ripples. This is especially true because measurements of ripple length in the field are more reliable than measurements of ripple height.

121. Since the bottom orbital diameter, A_b, is a measure of the horizontal displacement of a water particle due to the wave motion, it is natural to seek a relationship between A_b and the ripple wavelength λ. It has been observed by many authors, for example Mogridge and Kamphuis (1972), that λ is proportional to A_b up to a certain critical flow intensity. Mogridge and Kamphuis stated that beyond this point the ripple length is constant.

122. Regular waves. Figure 6 is a plot of the ratio λ/d against A_b/d for all the laboratory data listed in Table 1 on ripples formed by regular waves except those of Sato (1988), Mathisen (1989), and Rosengaus (1987). The data have been divided into four classes based on the value of the parameter D_*, which is defined by

$$D_* = 10^4 \frac{d\omega^2}{g} \tag{23}$$

123. The parameter D_* with an additional factor of $(s-1)$ in the denominator is the same as that suggested by Mogridge and Kamphuis (1972) to characterize the flow intensity at which λ ceased to be proportional to A_b. It is seen from Figure 6 that for low values of A_b/d the data are mostly on the straight line, given by

$$\lambda = 1.3A_b \tag{24}$$

41

Figure 6. Non-dimensional ripple wavelength, λ/d, plotted against the non-dimensional orbital amplitude, A_b/d, for ripples generated by regular laboratory waves. The data are grouped according to D_*.

that was suggested by Miller and Komar (1980a). As the value of A_b, which represents the strength of the flow, increases, the data points deviate from the line and attain maximum ripple length. Further increase in A_b results in a slight decrease in wave length, as pointed out by Nielsen (1979).

124. When the data are grouped according to D_* as in Figure 6, it is seen that the deviation from the straight line and the attainment of a maximum ripple length take place at progressively higher values of A_b/d for successively lower values of D_*. The data with the lowest values of D_*, marked by a + symbol, show an increase in λ as A_b increases with a constant of proportionality lower than that in equation (24). However, these data do not show a maximum ripple length.

125. Plots similar to Figure 6 were made with the data divided according to many dimensional and non-dimensional parameters, such as the wave period, grain diameter, and the Shields parameter. It was seen that data points that lay away from the straight line given by equation (24) were those for which the shear stress was high. However, D_* was found to be the best at indicating the maximum ripple length.

126. Miller and Komar (1980a) stated that this deviation depends on the grain diameter. This observation was based chiefly on their Figure 5 which shows the wave tunnel data of Carstens et al. (1969) and Mogridge and Kamphuis (1972). Since all the experiments of Carstens et al. were done at the same period of oscillation, D_* for their data depends only on the grain diameter. This would make it seem as though the deviation depended only on the grain diameter.

127. Figure 6 shows that the maximum wavelength observed on a sand bed is greater when D_* is small. The physical significance of D_* is not immediately apparent. The dependence on d is easily explained as smaller grains have lower fall velocities. Therefore smaller grains are more likely to follow the fluid motion resulting in the ripple length depending on A_b.

128. The presence of the wave frequency in D_* suggests that for two identical beds subject to the same orbital amplitude, the ripples on the bed subject to the lower frequencies will remain proportional to A_b up to a higher value of A_b. This may be because the bed has more time to react to

43

the lower frequency (longer period) motion leading to a greater dependence on A_b.

129. <u>Irregular field waves.</u> The available data on ripple length from field measurements is plotted, using the same axes as Figure 6, in Figure 7. It is seen that the data from the different investigations, while showing considerable scatter, plot in the same area of the graph. However, the trend is very different from the variation shown by laboratory waves.

130. Figure 8 shows the same data as Figure 7 grouped according to the value of D_*. The solid line is equation (24) while the dashed line is drawn to indicate the trend of the field data. An important point is that the range of D_* for the field measurements, 0.02 to 0.55, is quite different from the range in the laboratory experiments which was 0.07 to 14.5.

131. Figure 8 shows that several points lie considerably to the left of the solid line which represents the relationship of equation (24). The general trend of the field data is that λ decreases with increasing A_b. This behavior is most clearly shown by the data denoted by the + and * symbols, which mark the two lowest ranges of D_*. Only the data in the highest range of D_*--marked by an x--show an increasing trend similar to the data from regular wave experiments plotted in Figure 6.

132. Since the different ranges of D_* make the comparison of data in Figures 6 and 8 difficult, field and laboratory data are plotted together in Figure 9 for two ranges of D_*. These ranges are at the upper and lower ends of the region of overlap in the values of D_* for the two sets of data. This figure shows that for the range of D_* from 0.25-0.4 the laboratory and field data, shown by an x symbol and a * symbol, respectively, behave in the same way. However, for the lower range of D_* from 0.09-0.12 it is clear that the behavior of the field data, indicated by a +, is quite different from the laboratory data which are shown by circles. The field data show λ decreasing with increased A_b while the laboratory data follow equation (24).

133. Despite the large scatter in Figure 8 the data show some organization when grouped according to D_*. Therefore, it is difficult to explain the divergence from laboratory data as caused solely by the errors involved in making field measurements. One way in which the two data sets can be reconciled is by redefining the equivalent wave parameters for the
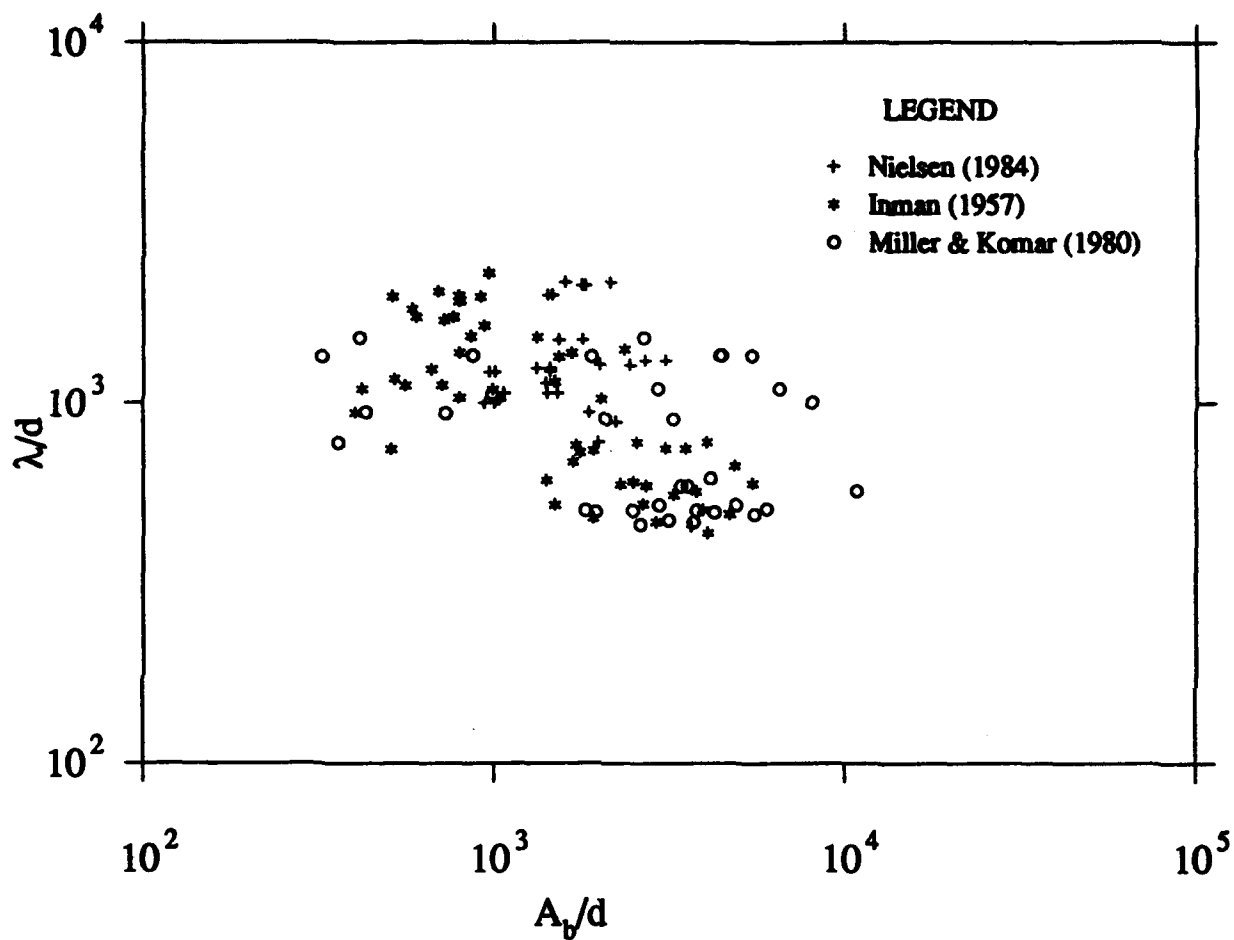
Figure 7. Non-dimensional ripple wavelength, λ/d, plotted against the non-dimensional orbital amplitude, A_b/d, for the field data of Inman (1957), Miller and Komar (1980), and Nielsen (1984)

45
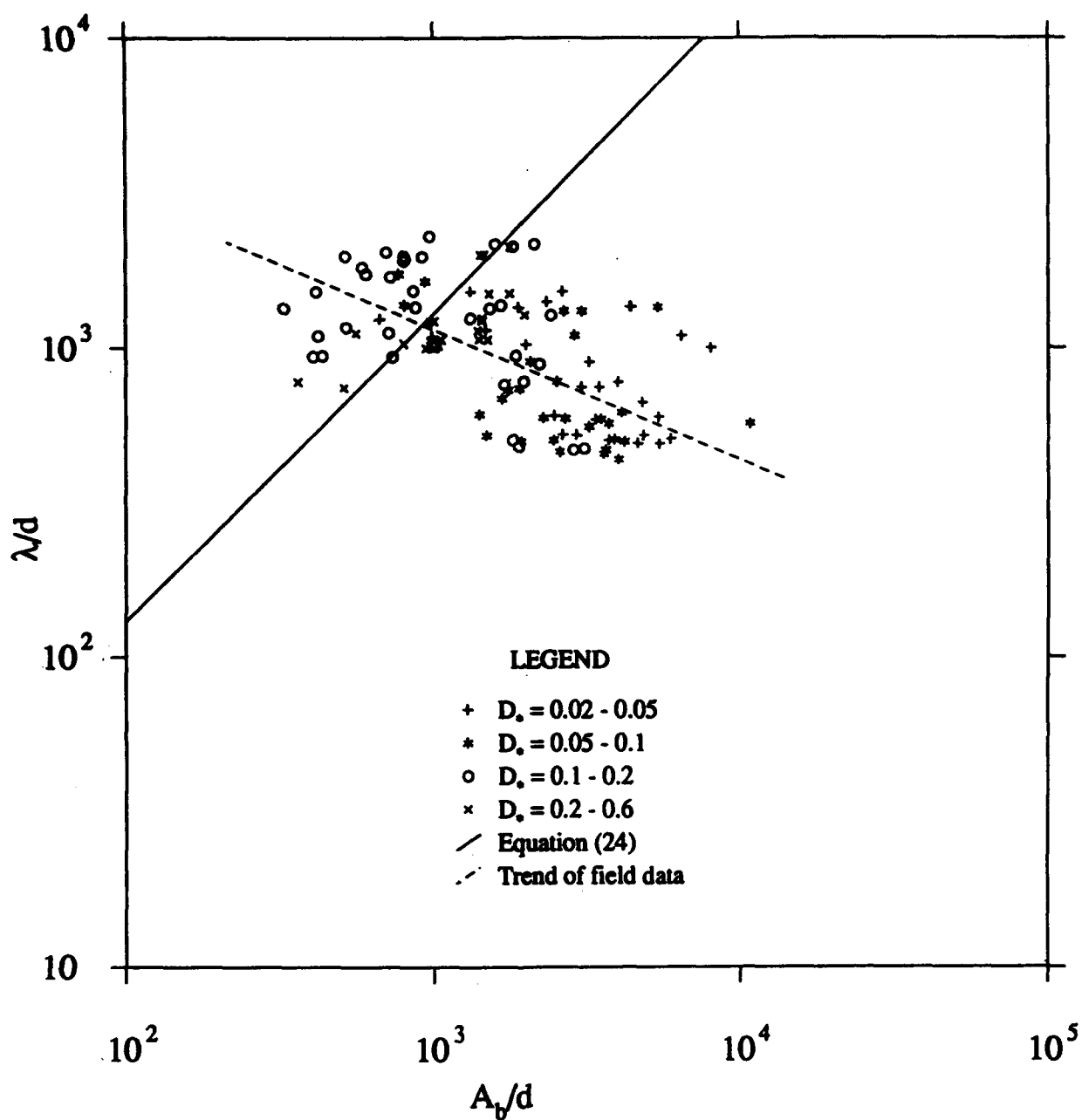
Figure 8. Non-dimensional ripple wavelength, λ/d, plotted against the non-dimensional orbital amplitude, A_b/d, for the field data grouped according to D_*.
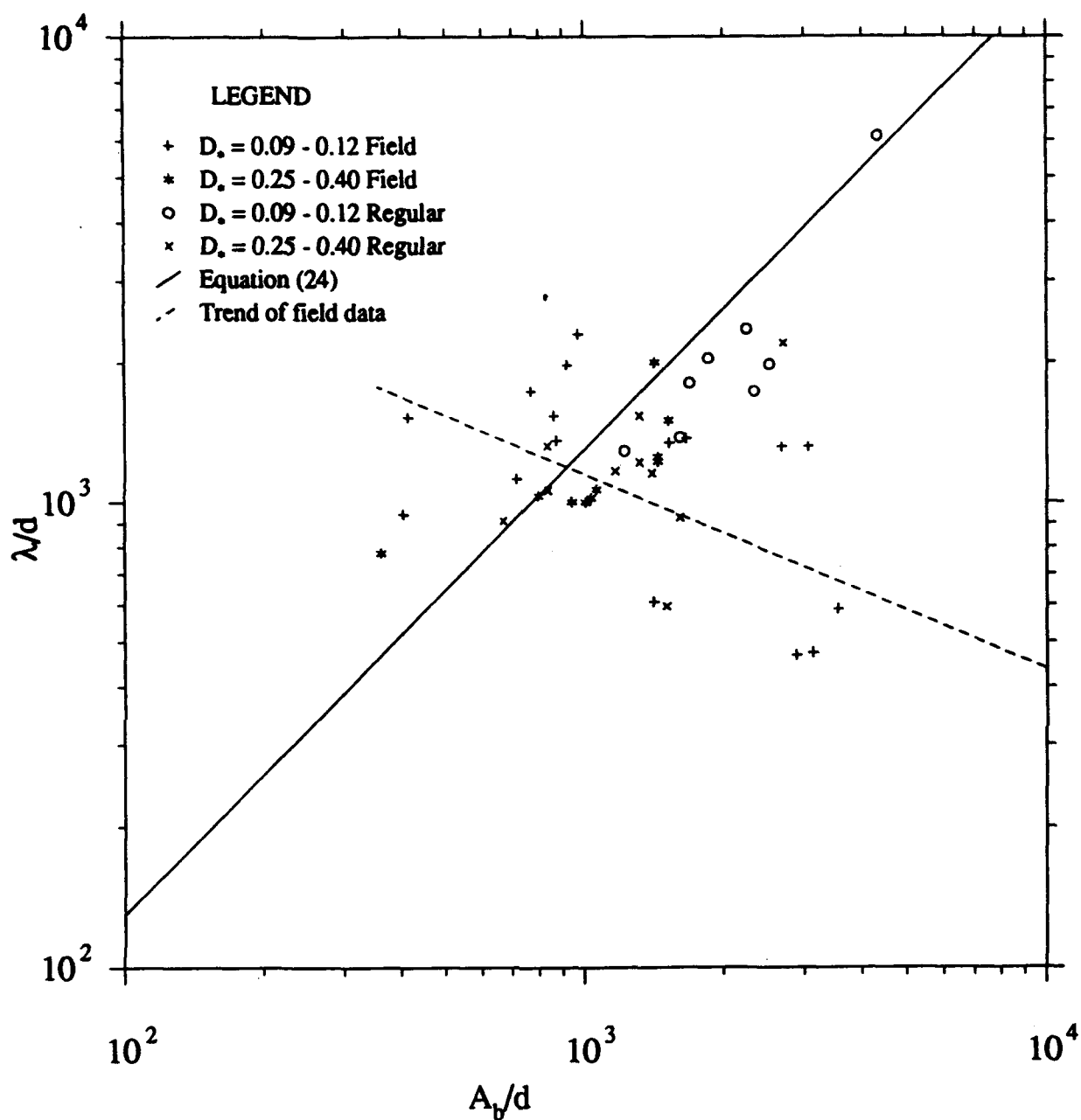
Figure 9. Comparison of laboratory data using regular waves and field data for two ranges of D_*.

field data. This could be done until the points that fall to the left of
the solid line in Figure 8, which is equation (24), are moved onto it. The
data that show a decrease of λ with increase in A_b could then be explained
as the result of flow intensities much higher than those required to cause
deviation from equation (24).

134. However, this would be an arbitrary process and would not
guarantee that the D_* values of field and laboratory data falling in the
same area would agree. Again, a satisfactory adjustment for the ripple
length may not be satisfactory for other ripple dimensions.

135. In any case since the only information known about the field waves
are the root-mean-square wave heights and the average period, an adjustment
of this kind would be a dubious proceeding. All that can be said is that
the ripple lengths observed in the field behave quite differently from
laboratory data. Whether this is due to the incorrect specification of the
equivalent wave or due to some mechanism that is present only when the
waves are irregular is unclear.

136. <u>Irregular laboratory waves.</u> The question of the validity of the
field data can be resolved by examining the data on ripples generated by
irregular waves in the laboratory. Table 2 shows that there are just three
data sets in which the ripple geometry generated by irregular waves has
been measured. Two of these, the data sets of Mathisen (1989) and
Rosengaus (1987), were conducted in the same wave flume and will be
considered together.

137. These data sets will be analyzed by plotting the results for
regular and irregular waves in the same manner as in Figure 6. It is
important to plot the data from regular waves using these experimental set-
ups separately because this will show whether the trend of the regular wave
data is changed by a particular apparatus. It was for this reason that the
regular wave data of Mathisen, Rosengaus, and Sato were not included in
Figure 6. Comparison of the plots of the regular and irregular wave data
will enable the effects of wave irregularity to be seen in isolation.

138. Figure 10 shows that data of Mathisen (1989) and Rosengaus (1987)
for regular and irregular waves. The values of D_* are 0.7-0.8 for the
0.12-mm sand and 1.1-1.3 for the 0.2-mm sand. The irregular waves are
represented by H_{rms} and the average period. The figure shows that while the
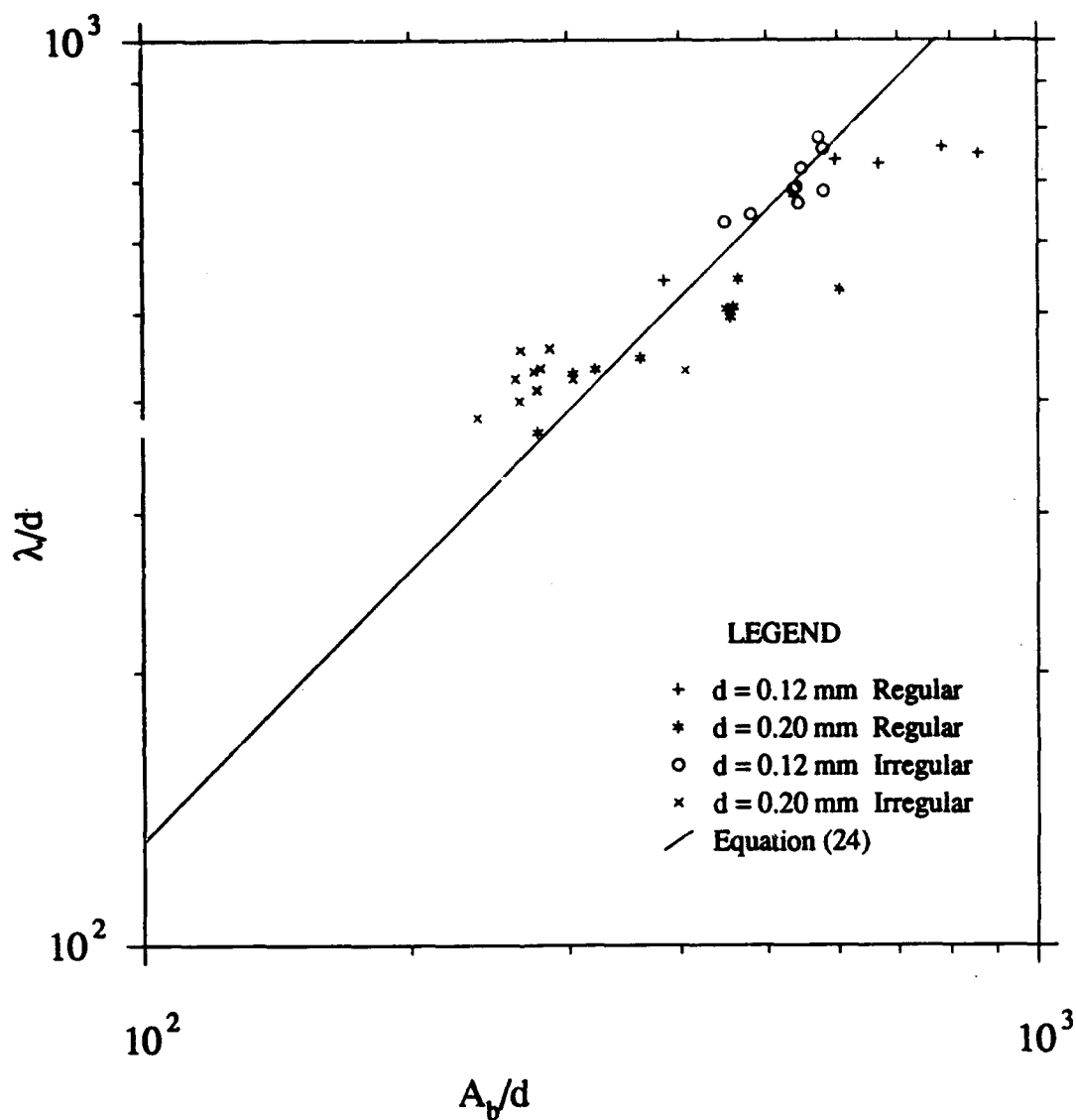
Figure 10. Non-dimensional ripple wavelength, λ/d, plotted against the non-dimensional orbital amplitude, A_b/d, for the regular and irregular wave laboratory experiments of Rosengaus (1987) and Mathisen (1989)

49

data from regular and irregular waves do not coincide they both agree quite
well with the trend for regular waves. The data lie on the solid line up to
about $A_b/d = 400$ and then deviate to the right. Data with a comparable
value of D_* are denoted in Figure 6 by circles. Comparing Figure 6 and 10
it is seen that the data of Mathisen and Rosengaus are in agreement with
the other regular wave data.

139. The ripple data of Sato (1988) from regular and irregular wave
laboratory experiments are plotted in Figures 11 and 12, respectively.
Figure 11 shows that the regular wave data deviate considerably from the
straight line equation (24). However, comparison with data that have
similar values of D_* in Figure 6 shows that the data in these higher ranges
of D_* in Figure 11 are consistent with the other regular wave data. The
data in the lowest range of D_*, while showing an increase in λ with
increasing A_b that is in agreement with the trend of the other regular wave
data, plot below the comparable data in Figure 6.

140. Figure 12 shows the data on ripples formed by irregular waves
using the same apparatus. Comparing with Figure 11 it is seen that there
is a difference in the trend of the two data sets. For example, data with
D_* around 0.8, marked by a *, lie a little below the corresponding regular
wave data and show a slight decrease in λ with increasing A_b. The greatest
difference is seen in the data with the lowest value of D_*, marked by a +
symbol. The irregular wave data do not show the increase in λ with A_b that
is shown by the regular wave data.

141. These observations must be regarded as tentative because they are
based on a very small number of data points. However, it does seem that
the irregular wave ripple data of Sato (1988) differ from the regular wave
data in a manner similar to the way in which the field data differ from the
regular wave data. For example the trend in Figure 11 is fairly close to
the solid line while the trend in Figure 12 seems to be more in agreement
with the dashed line which shows the trend of the field data. This
similarity lends support to the view that the difference between field and
laboratory data is due to the irregularity of the field waves and not
entirely to errors in measurement.

142. Comparing Figures 10 and 12 it is seen that even when the value of
D_* is comparable the irregular wave data of Mathisen and Rosengaus differ
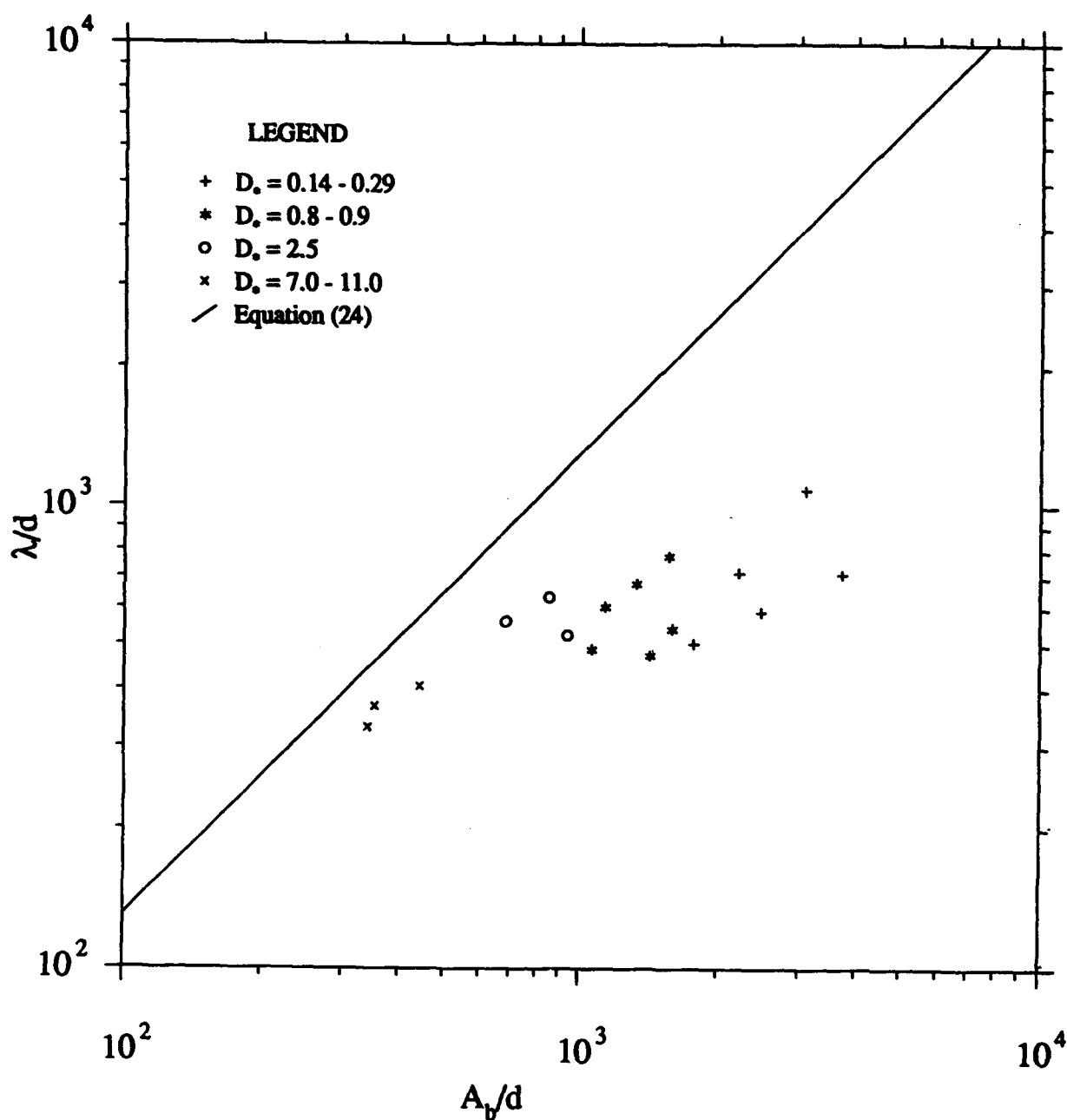
Figure 11. Non-dimensional ripple wavelength, λ/d, plotted against the non-dimensional orbital amplitude, A_b/d, for the regular wave laboratory experiments of Sato (1988)
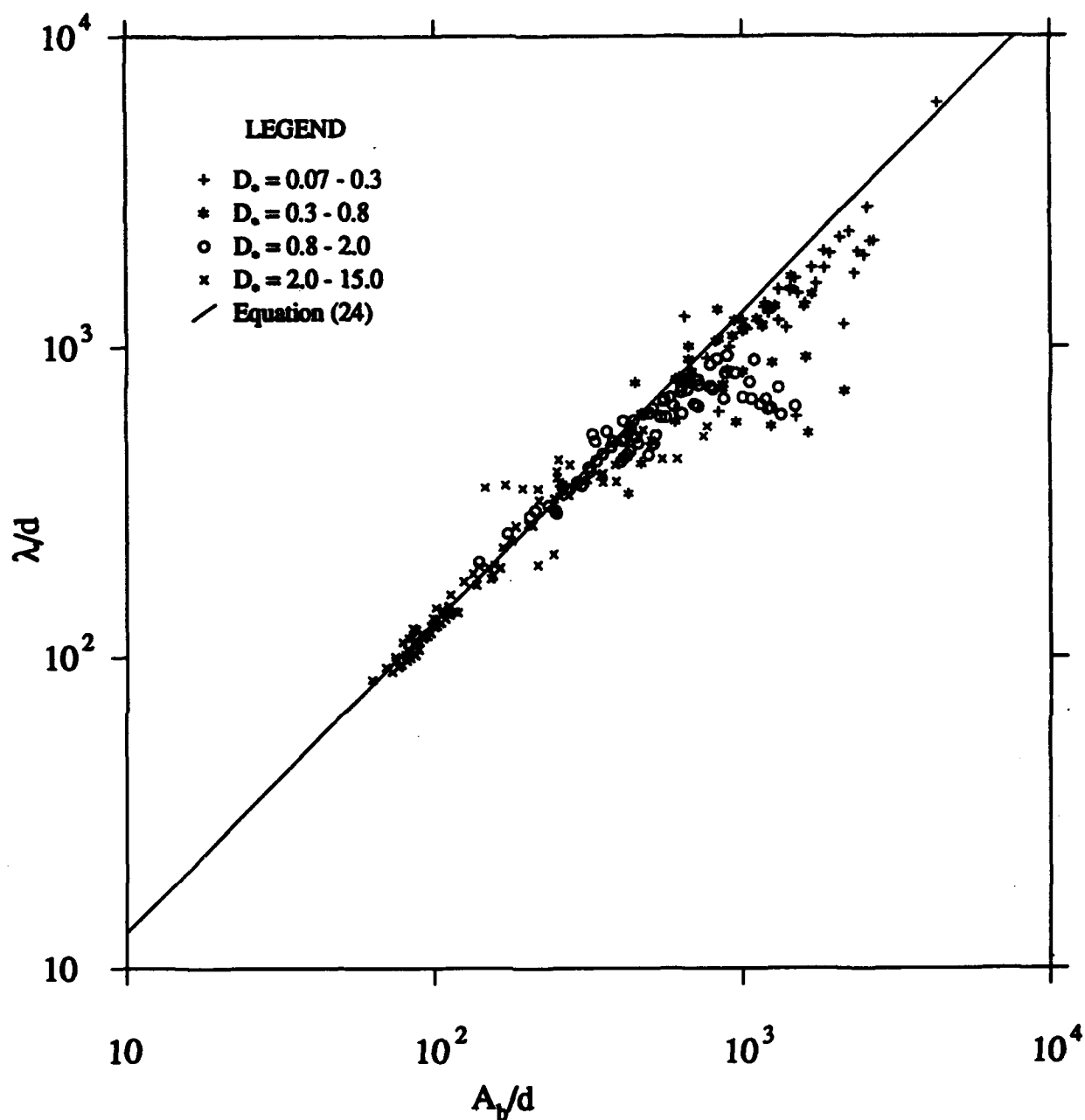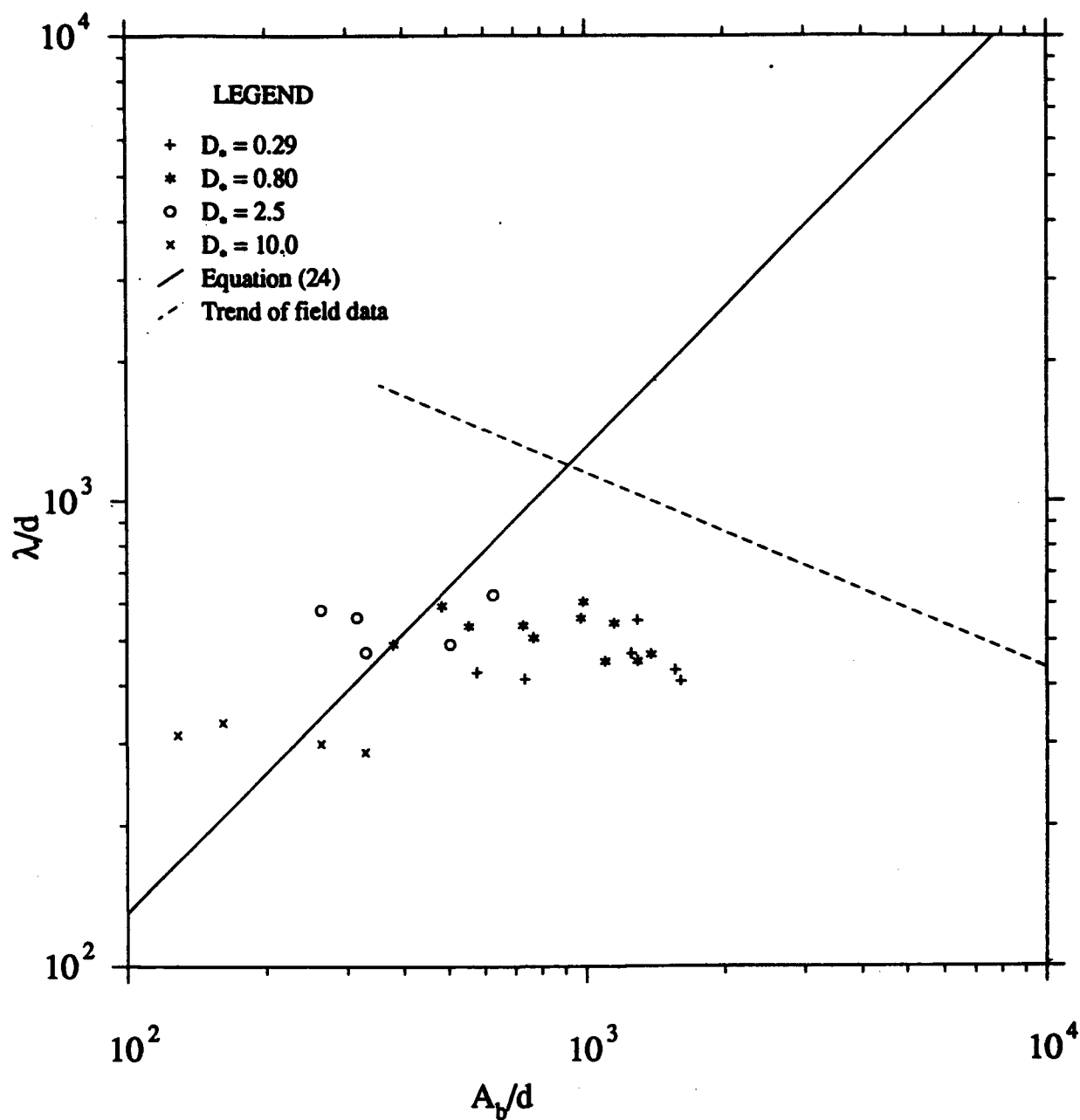
Figure 12. Non-dimensional ripple wavelength, $\tilde{\lambda}/d$, plotted against the non-dimensional orbital amplitude, A_b/d, for the irregular wave laboratory experiments of Sato (1988)

from those of Sato. The reason is that in the experiments of Sato the shear stress, as measured by the parameter ψ, was much higher than in the other experiments. Sato's experiments had ψ in the range 0.07-0.79 with an average of 0.36 while the experiments of Mathisen and Rosengaus had ψ ranging from 0.08 to 0.21 with an average of 0.16.

143. <u>Summary of λ-A_b relationship.</u> The analysis of the relationship between the ripple length and the orbital amplitude shows that most field data, with the waves specified by the root-mean-square wave height and average period, do not follow the simple relationship given by equation (24). This deviation is most marked for low values of D_*. Similar behavior was observed in the irregular wave data of Sato (1988) but not in the data of Mathisen (1989) and Rosengaus (1987).

144. These observations can be explained by the following argument. Since the range of grain diameters in all these experiments is 0.1-0.6 mm differences in D_* are mainly due to differences in the wave period. The differences in ripple geometry caused by regular and irregular waves of the same intensity has been attributed by Mathisen (1989) to the domination of the ripple generation process by the larger waves. This would explain why ripples generated by irregular waves do not follow equation (24).

145. However, the fact that the data with high values of D_* are quite close to this equation suggests that this change in the process is seen only when the wave period is large enough, i.e., when D_* is small. This is to be expected since the larger waves will have a more significant effect if they act for a longer time.

146. Comparing the data of Rosengaus and Mathisen with the data of Sato it is seen that there is also an effect of the Shields parameter. For a given period, a wave that, for example, is twice as large as the average will have a greater effect on the bed when the average wave intensity, as measured by the Shields parameter, is higher.

147. For a wave period of 8 seconds and a grain diameter of 0.2 mm, which are typical of the field, D_* is found to be 0.126. As shown in Figure 9 the field and laboratory data behave quite differently at this value of D_*. Therefore the use of relations based on regular wave laboratory data to predict ripple geometry in the field under these conditions could result in considerable error. Also the data from irregular wave laboratory

experiments are too few and conducted at too high a value of D_* to be applied to field conditions.

148.   Thus it can be concluded that the best method of predicting field ripple geometry, at the present time, is through relations based on field measurements. Simple equations for predicting the ripple length, height, and steepness for field ripples will be developed in the next three sections.

149.   Prediction of the ripple length. This is done by plotting the ratio λ/A_b against a non-dimensional parameter that represents the intensity of the flow. Nielsen (1979) suggested that the parameter θ, defined by

$$\theta = \frac{u_{bm}^2}{(s-1)gd} \qquad (25)$$

was able to correlate the data on ripple length successfully. He plotted the data of Inman (1957) and Dingler (1975) against θ and obtained a good correlation. However, when the data presented by Nielsen (1984), which were collected in shallow water, are plotted on the diagram they do not correspond with the earlier data.

150.   Before developing a predictive relation it is necessary to decide upon the method that is to be used to determine the expression that gives the best fit. A commonly used measure is root-mean-square error r, defined by

$$r = \left[\frac{\sum_{1}^{n}(y-\hat{y})^2}{n-1} \right]^{\frac{1}{2}} \qquad (26)$$

where y is the measured value and $\hat{y}$ the predicted value and n is the number of data points.

151.   The drawback of this measure is that while it gives an idea of how far the proposed line is from the data it does not give any measure of how much that difference is when compared to the actual value of the data point. A more suitable measure is the relative error e, defined by

$$\ln(e) = \left[\frac{1}{n}\sum_{1}^{n}(\ln(y) - \ln(\hat{y}))^2\right]^{\frac{1}{2}} \qquad (27)$$

152. When e is minimized the resulting fit is a least-squares fit on a log-log plot. A perfect correlation will result in e being equal to 1. This measure of the error is more suitable than r when the data span several orders of magnitude. A value of e = 1.2, for example, would indicate an error of ±20% in the curve fit.

153. It was found that the available field data on ripple length was well correlated by the non-dimensional parameter X, defined by

$$X = \frac{\theta}{S_*} \qquad (28)$$

where S_* is defined in equation (13). Figure 13 shows the ratio λ/A_b plotted against the parameter X for the field data. The solid line is the proposed relation for ripple lengths in the field and is given by

$$\frac{\lambda}{A_b} = \begin{array}{ll} 1.7X^{-0.5} & X < 3 \\ 2.2X^{-0.75} & X > 3 \end{array} \qquad (29)$$

The value of the relative error for this relation was 1.48. If the root-mean square error is used it results in a significant bias towards the larger values. Since equation (29) is an empirical fit it should only be applied in the range 0.2 < X < 50.

154. Another parameter that correlates the field data well is $\psi^{\frac{1}{2}}(A_b/d)$ which was suggested by Sato (1987). When a relation of the same form as equation (29) is fit to the data using this parameter e is found to be 1.55. If θ is used as the dependent variable, as suggested by Nielsen (1979), e is found to be 2.36. X is used in this report instead of the parameter of Sato because it is found to correlate other aspects of field ripple geometry as well as the friction factor observed in laboratory experiments.

155. The data from laboratory experiments with irregular waves are plotted in Figure 14 along with a line representing equation (29) and a dashed line showing the trend of the data obtained using regular waves.
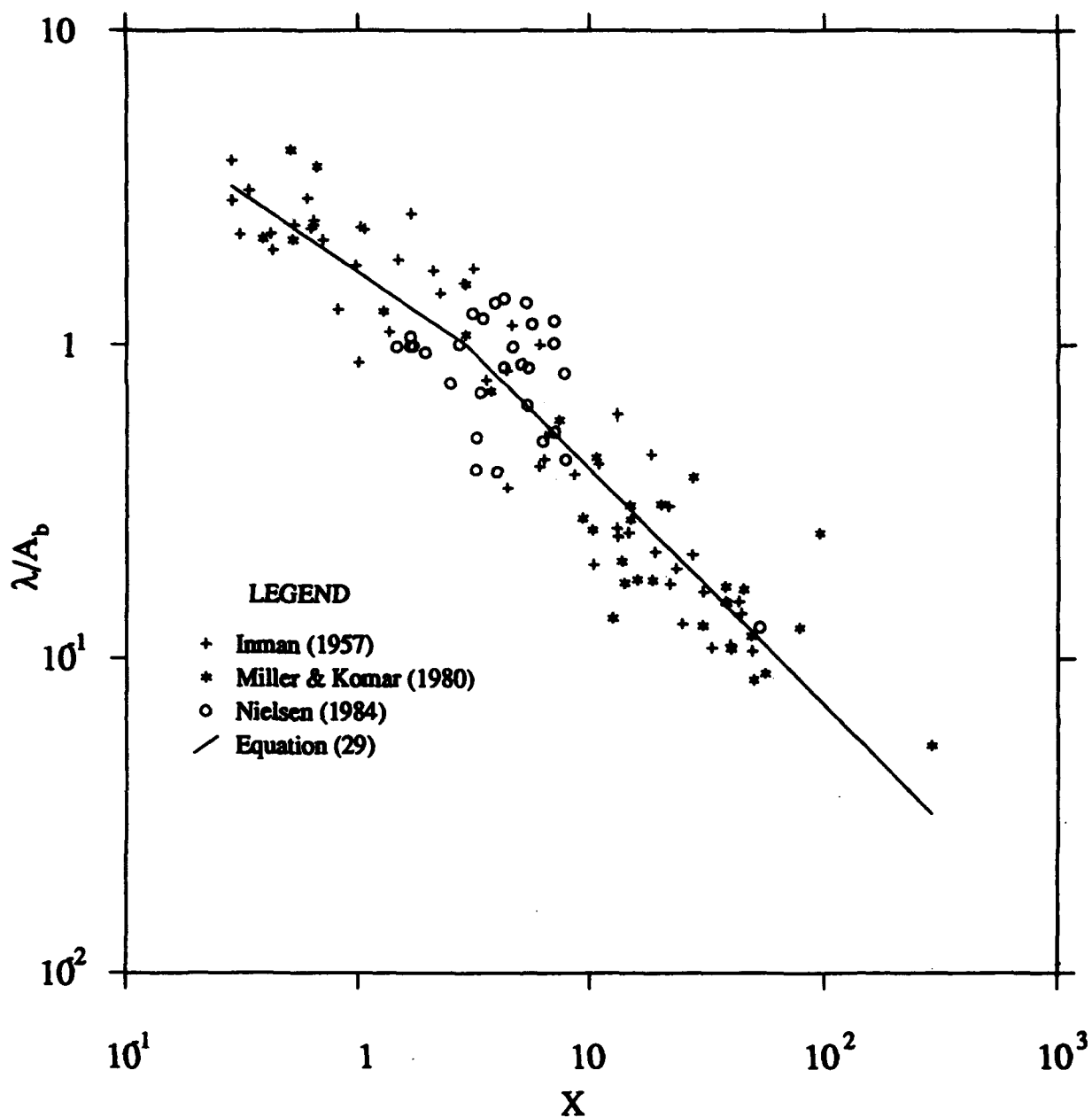
Figure 13. Non-dimensional ripple length, λ/A_b, against the parameter X for the field data of Inman (1957), Komar and Miller (1980), and Nielsen (1984) along with equation (29)

56
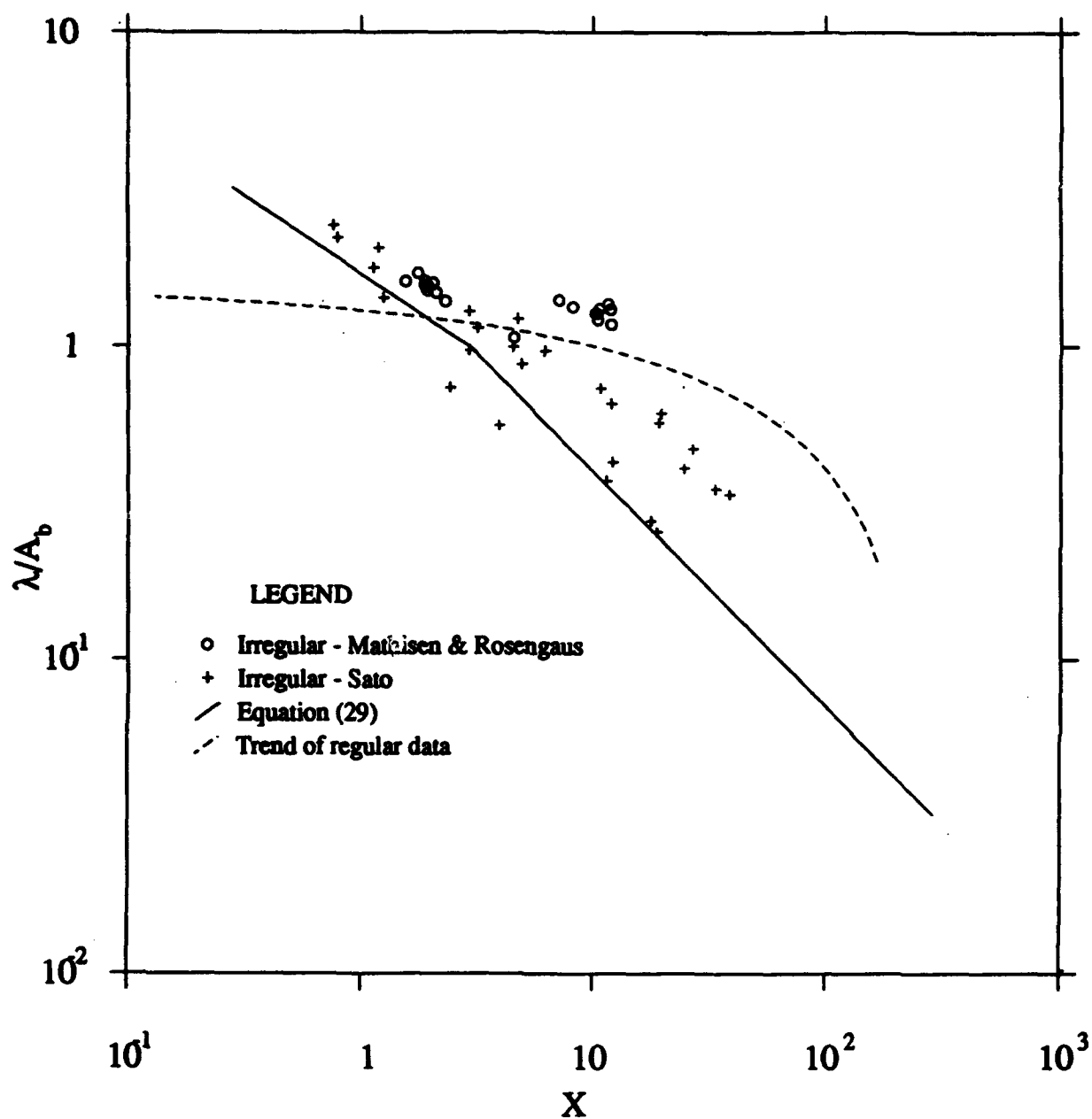
Figure 14. Non-dimensional ripple length, λ/A_b, against X for the irregular wave laboratory data of Mathisen (1989), Rosengaus (1987), and Sato (1988) along with equation (29) and a line showing the trend of the regular wave laboratory data

The data from Mathisen (1989) and Rosengaus (1987) plot slightly above the line for the regular wave data while the data of Sato (1988) lie between the curves for regular wave and field wave data. This is in agreement with the analysis in the preceding section.

156. Therefore equation (29) is proposed as a new relation for predicting the length of field ripples. For ripples formed by regular waves in the laboratory however, it is found that using the parameter X does not result in a better correlation than if the parameters suggested by Nielsen (1979) and Sato (1987) are used. For this reason, and also because the interest is in predicting ripples in the field, relations are not developed for ripples formed by regular laboratory waves.

157. Prediction of the ripple height. As in the case of the ripple length, the bottom orbital amplitude is selected to non-dimensionalize the ripple height. The ratio η/A_b is plotted against X in Figure 15 for the field data. The solid line is the proposed relation which is given by

$$\frac{\eta}{A_b} = \begin{array}{ll} 0.27X^{-0.5} & X < 3 \\ 0.47X^{-1.0} & X > 3 \end{array} \tag{30}$$

158. The data plotted at the bottom of Figure 15, i.e., with $\eta/A_b = 10^{-3}$, are the points where a flat bed was observed. This suggests that the disappearance of ripples occurs around the point X = 50. The value of the relative error obtained using equation (30) was 1.55.

159. The ripple heights obtained using irregular waves in the laboratory are plotted in Figure 16 along with the curve showing the trend of the regular wave data and the proposed relation given by equation (30). Here too it is seen that the data of Mathisen and Rosengaus lie somewhat above the curve for the regular wave data. However, comparing Figures 15 and 16 it is seen that the data of Sato plot only slightly above the region occupied by the field data. The flat-bed data points of Sato are also not in agreement with the field data.

160. Prediction of ripple steepness. Equations (29) and (30) can be combined to give a relation for the steepness as
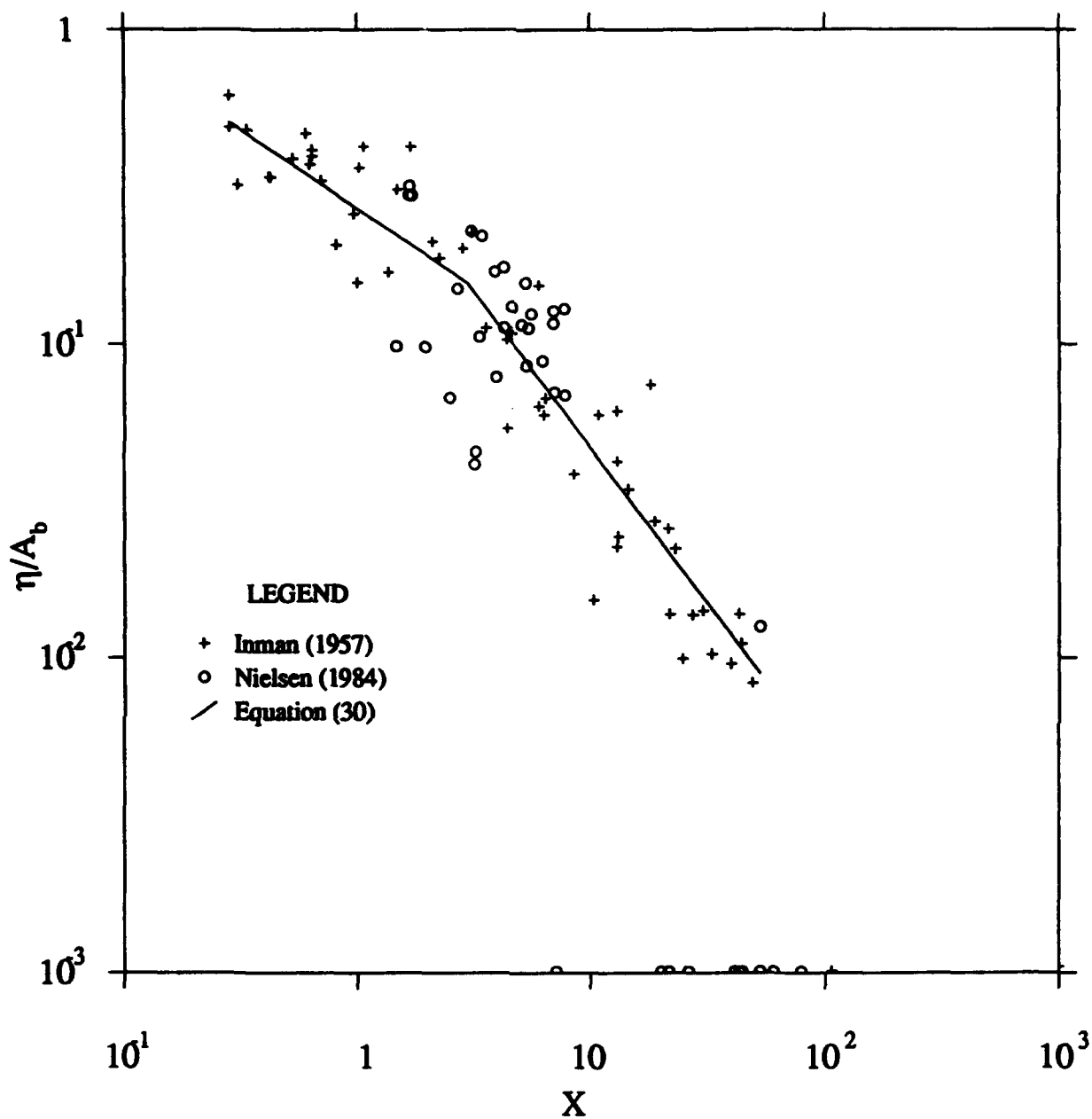
Figure 15. Non-dimensional ripple height, η/A_b, against X for the field data of Inman (1957), Komar and Miller (1980), and Nielsen (1984) along with equation (30)
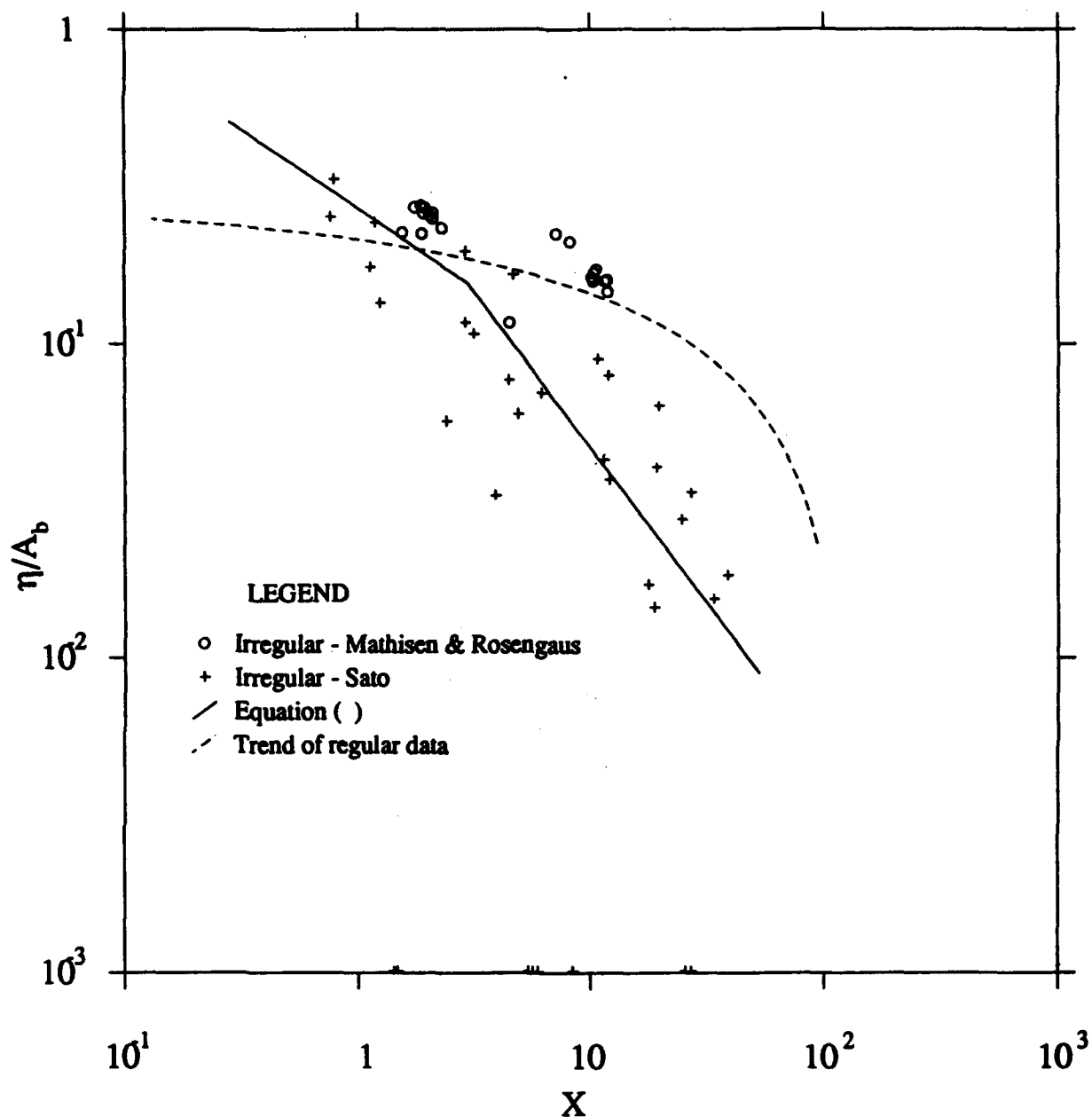
Figure 16. Non-dimensional ripple height, η/A_b against X for the irregular wave laboratory data of Mathisen (1989), Rosengaus (1987), and Sato (1988) along with equation (30) and a line showing the trend of the regular wave laboratory data

$$\frac{\eta}{\lambda} = \begin{cases} 0.16 & X < 3 \\ 0.21X^{-0.25} & X > 3 \end{cases} \qquad (31)$$

The value of the relative error for this relation is 1.27. Sato (1988) used the parameter $\psi(A_b/d)^{1/3}$ to correlate the field data on ripple steepness. When a relation of the form suggested by him is fit to the data the value of the relative error is 1.31.

161. Equation (31) is plotted in Figure 17 along with the trend of the regular wave data and the irregular wave data from the laboratory. It is seen that the steepness of the field ripples is only slightly lower than that of the ripples formed by regular waves. The data of Mathisen (1989) and Rosengaus (1987) lie close to the regular wave data as expected but the data of Sato (1988) show a lower steepness than the field data. This is because the data of Sato show longer ripple lengths and smaller ripple heights than the field data for comparable values of X. Sato (1988) used a wave tunnel that was 21 cm high. The largest ripple height measured under irregular wave conditions was 4.9 cm. It is possible that these ripples did not grow to their full height due to the limited tunnel height. This may be the reason for the low ripple heights observed by Sato.

162. <u>Disappearance of ripples.</u> Sato (1988) analyzed data from regular and irregular laboratory experiments and from the field and proposed a criterion for the disappearance of ripples based on the parameter ψ and A_b/d. However, examination of his Figure 12, which is a plot of the field data, reveals that while his criterion is good for laboratory ripples it is only approximately true for the field data.

163. A simpler relationship that is as accurate can be obtained by observing the flat bed data in Figure 15. From this figure an approximate criterion for the disappearance of ripples can be derived as

$$X > 50 \qquad (32)$$
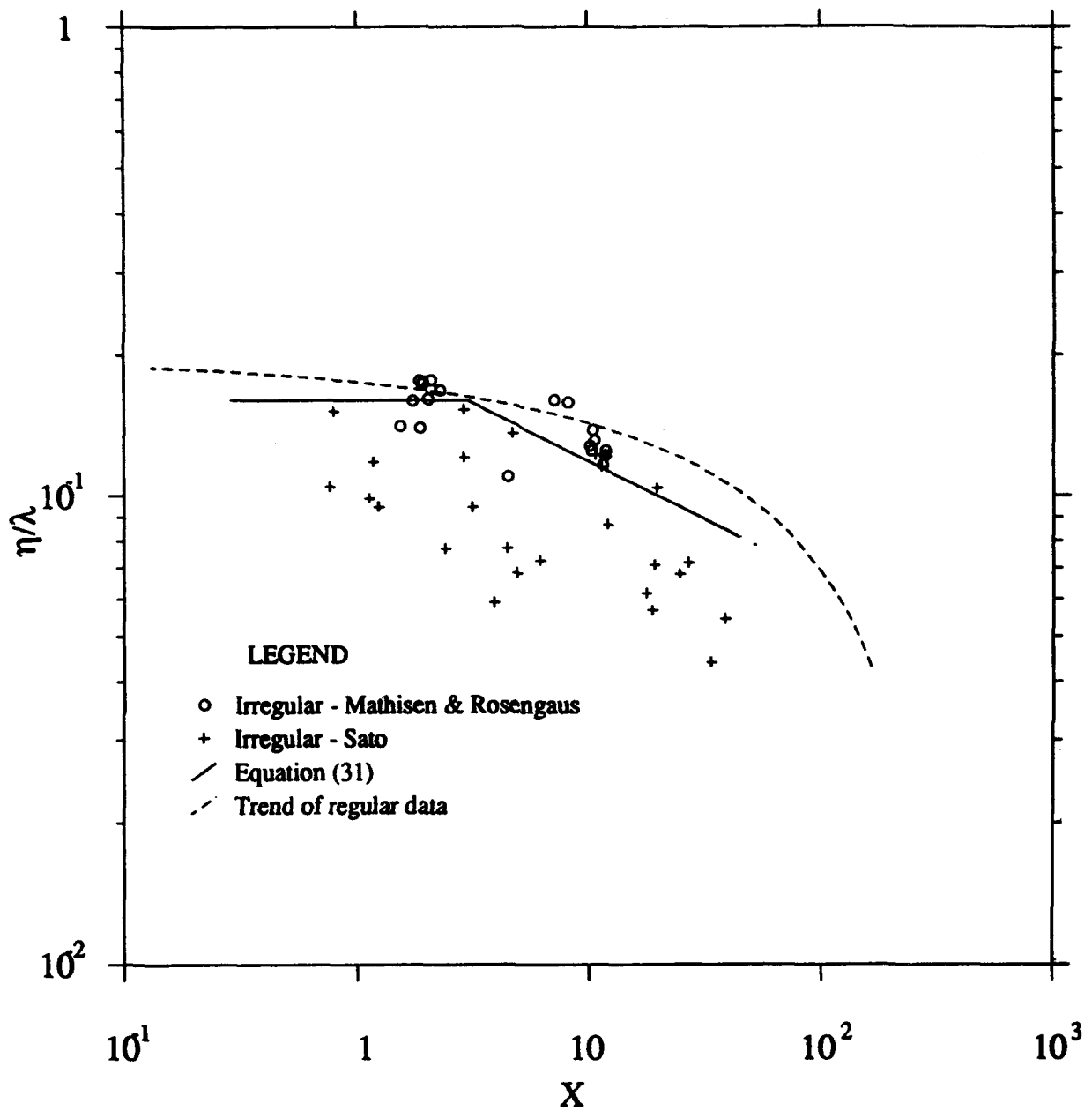
Figure 17. Ripple steepness, η/λ, against X for the irregular wave laboratory data of Mathisen (1989), Rosengaus (1987), and Sato (1988) along with equation (31) and a line showing the trend of the regular wave laboratory data

PART IV: MOVABLE BED ROUGHNESS

164. The relationship between the geometry of ripples and the wave motion that created them was investigated in the preceding section. Predictive relationships for the ripple geometry under field conditions, with the waves specified by the root-mean-square wave height, H_{rms}, and the average period, were proposed. The objective of this section will be to review the relationship between bed geometry and the friction factor in order to propose relations that could lead to the establishment of friction factor relationships to be applied in the field.

165. It was concluded in Part II that the only reliable method of measuring the friction factor on a movable bed was through measurements of the energy dissipation in the wave boundary layer. Therefore the investigation of the effects of the bed geometry on the friction factor requires the simultaneous measurement of the wave conditions, the associated bedform geometry, and the resulting energy dissipation.

166. Wave energy dissipation in the field is measured by recording the change in wave height between two points. After allowances are made for changes due to refraction and shoaling the dissipation is calculated from the wave attenuation ascribed to bottom friction. Such studies have been carried out by Iwagaki and Kakinuma (1963, 1967) and Treloar and Abernathy (1978). However, the ripple geometry was not recorded in any of these studies.

167. This means that the analysis in this chapter will rely entirely on laboratory experiments, most of which have been conducted using a regular wave motion. It was found in Part III that wave irregularity resulted in the ripple geometry differing from that formed by regular waves. This meant that ripple data from laboratory regular wave experiments were not applicable under field conditions.

168. Bearing this in mind it would seem overly optimistic to expect the results of energy dissipation experiments with regular waves in the laboratory to be relevant to irregular field waves. Nevertheless this is the only way in which the field ripple geometry relations developed in Part III can be used to predict the bed friction. The alternative is to rely on field studies that have been done without observations of the bottom

63

Table 4
Summary of Available Laboratory Data on Energy Dissipation under Waves

Sources of data	Type of apparatus and wave condition	Diameter of sand (mm)	Range of periods (s)	Number of data points
Mathisen (1989)	WF, R	0.12	2.6	6
	WF, IR	0.12	2.6	11
		0.2	2.6	5
Rosengaus (1987)	WF, R	0.2	2.2-3	17
	WF, IR	0.2	2.6	10
Lofquist (1986)	WT, R	0.18	3.9-14.2	20
		0.55	2.7-9.4	62
Sleath (1985)	OB, R	fixed bed	0.6-18.1	61
Carstens et al. (1969)	WT, R	0.19	3.5	5
		0.297	3.5	15
		0.585	3.5	20
Bagnold (1946)	OB, R	fixed bed	0.3-5.6	59

WF: wave flume; WT: wave tunnel; OB: oscillating bed
R: regular waves; IR: irregular waves

geometry.

169. The available experimental data on energy dissipation under waves are summarized in Table 4. The details of the experiments and the derivation of the friction factor from the measurements are discussed in Appendix A. It should be noted that the data sets of Sleath (1985) and Bagnold (1946) for energy dissipation over a fixed, rippled bed are included in Table 4. These data are included because the energy dissipation over a movable bed is due to a combination of the form drag due to the bedforms, the skin friction due to the sand grains, and the effect of a moving layer of grains. The analysis of the fixed bed data should help to determine the relative magnitude of these effects.

Energy Dissipation over a Fixed Bed

170. Bagnold (1946) and Sleath (1985) measured energy dissipation over beds with fixed artificial ripples using an oscillatory bed apparatus. These results have been analyzed in detail by Sleath (1985). For our purposes the chief use of these data is to establish a link between the ripple geometry and the equivalent bed roughness.

171. The simplest relation is to set the equivalent roughness, k_n, to be proportional to the ripple height, i.e.,

$$k_n \sim \eta \tag{33}$$

Grant and Madsen (1982) concluded that wave-generated ripples should be quantified by both their height and their concentration and suggested the form

$$k_n \sim \eta \frac{\eta}{\lambda} \tag{34}$$

172. The measured values of the friction factor over the fixed bed can be converted into a value of k_n using the Grant-Madsen friction factor relation in equation (7) and the known value of the bottom orbital amplitude. The ratio k_n/η is plotted in Figure 18 against the flow Reynolds number Re defined after equation (2). It should be noted that for a fixed

65
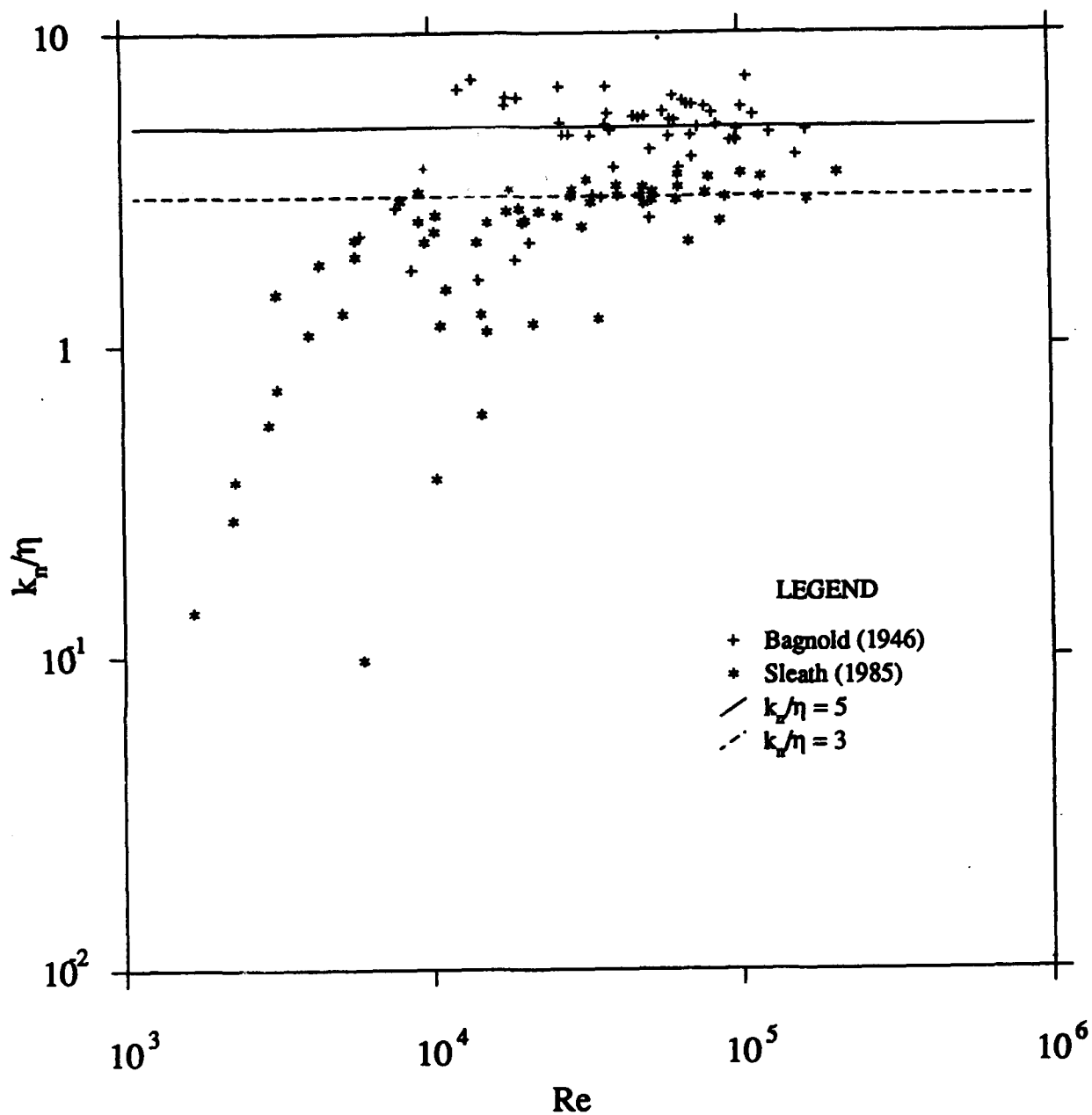
Figure 18. The ratio of equivalent roughness to ripple height, k_n/η, plotted against the near-bottom Reynolds number, Re, for the data of Bagnold (1946) and Sleath (1985), along with lines representing $k_n/\eta = 5$ and $k_n/\eta = 3$

bed the parameters s, d, and g are not present resulting in the flow being described by just one non-dimensional parameter.

173. The figure shows that while some points in each data set show a trend in increasing k_n/η with increasing Re most of the points are clustered around a constant value. This value, which is the constant of proportionality in equation (33), is seen to be around 5 for the data of Bagnold and about 3 for the data of Sleath.

174. Sleath (1985) used a sinusoidal profile for his artificial ripples with a steepness of 0.23 while Bagnold (1946) used a profile composed of circular arcs which formed sharp-crested ripples with a steepness of 0.15. Sleath (1985) found that the low values of the friction factor, and therefore of k_n/η, were observed during the transition from laminar flow when flow separation and vortex formation were just beginning.

175. Since the flow over sand ripples is most often rough turbulent these points are not important for this analysis. Sleath argued that the effect of transition was less apparent in the data of Bagnold because the sharp crest of the ripples in those experiments would have caused separation at the crests even at low flow velocities.

176. Both Sleath and Bagnold used a constant value of the ripple steepness throughout their experiments. Therefore it is not possible to determine which of equations (33) and (34) provides a better representation of the equivalent roughness. If the ratio $k_n/(\eta^2/\lambda)$ is plotted against Re the constant of proportionality in equation (34) is found to be 33 and 12.5 for the data of Bagnold and Sleath, respectively.

177. Equilibrium ripples formed by waves are sharp crested and have slopes of about 30°. In these respects they resemble the profile used by Bagnold (1946) which had a crest angle of 120°. However, these artificial ripples had a very sharp edge, a feature that sand ripples can not have. Observations of ripples under irregular waves by Mathisen (1989) have shown that the crests are more rounded than if the waves were regular. Thus the geometry of field ripples is probably somewhere in between the two extremes represented by the artificial beds used by Bagnold and Sleath. It should also be noted that both these authors used a smooth surface for their ripples while sand ripples have a rough surface. This may result in the skin friction felt by the sand ripples not being reproduced in the

laboratory. When the ripple height is much larger than the grain diameter the skin friction is expected to be much smaller than the form drag. However, the roughness of the ripple surface will influence the separation at the crest.

178. In summary it can be said that the analysis of the fixed bed experiments show that both equations (33) and (34) are plausible representations of the equivalent roughness of a rippled bed. The constant of proportionality for sand ripples can be expected to be between 3 and 5, and 12.5 and 33 for equations (33) and (34), respectively.

Energy Dissipation over a Movable Bed

179. The results of energy dissipation measurements over movable sand beds will be analyzed to determine the appropriate equivalent bed roughness scales in this case. It is seen in Table 4 that there are only four data sets where simultaneous measurements of ripple geometry and energy dissipation have been made. Some aspects of these experiments are discussed in Appendix A.

180. Of these four data sets the largest is the set presented in Lofquist (1986). Some of these measurements were made under conditions that resulted in the end effects having significant effects on the ripple geometry. For this reason these data were not used in the analysis of ripple geometry.

181. However, our purpose in this section is to quantify the energy dissipation over ripples whose geometry is known. Analysis by Lofquist (1986) has shown that there are no significant differences between the shear stresses observed over the "natural" and the "distorted" ripples. Therefore all the equilibrium measurements of Lofquist will be used here.

182. Lofquist also measured the shear stress during ripple growth from an initially flat bed. These ripples are not in equilibrium with the flow and it could be expected that this would affect the energy dissipation. The results show that it takes from 30 to 100 wave cycles to increase the ripple height by 1 cm. Since this is quite a slow rate of growth the effect of disequilibrium on the shear stress is likely to be small. Furthermore these data increase the ranges of ripple height and steepness over which

dissipation has been measured. For these reasons the results from the growing ripples will also be considered in the analysis though they will not be used to establish predictive relations.

183. The best fit relations established in this section will be based on the relative error defined in equation (27). Since the ultimate objective is to predict the friction factor and also because it is the friction factor that is measured, the relative errors given will be those for the predicted friction factor and not for the equivalent roughness. To avoid the analysis being dominated by the large number of data in Lofquist (1986) the best-fit coefficient for the other sets will also be reported in most cases.

Regular Waves

184. The four data sets on energy dissipation over equilibrium ripples under regular waves are those of Carstens et al. (1969), Lofquist (1986), Rosengaus (1987), and Mathisen (1989). Since Mathisen used the same apparatus as Rosengaus these two data sets will be considered together.

185. The data from fixed bed experiments suggested that either equation (33) or (34) could be used to define the equivalent roughness. The ratio k_n/η is plotted against the Shields parameter, ψ, in Figure 19 for the data on equilibrium ripples together with the data from the growing ripples. The value of k_n was calculated using equation (7) along with the measured values of f_w and A_b.

186. Although the scatter of the data is quite high the figure shows that the ratio k_n/η is well represented by a constant value. The scatter of the data is higher at low flow intensities for reasons discussed in Appendix A. The best-fit values of the constant of proportionality in equation (33) are 5.2, 4.0, and 3.0 for the equilibrium ripple data of Carstens et al., Lofquist, and Mathisen and Rosengaus, respectively. The overall best fit value is 4.0. The data from the growing ripples are consistent with the equilibrium ripple data of Lofquist.

187. When equation (34) is used to scale the equivalent roughness the overall best fit constant is 26.0. However, the value of e is 1.35 while it was 1.27 for the overall fit using equat⁵   ´33). When the individual best fits for each data set are compared the   ues obtained using equations (33) and (34) are 1.27 to 1.46, 1.22 to 1.28, and 1.25 to 1.22

69
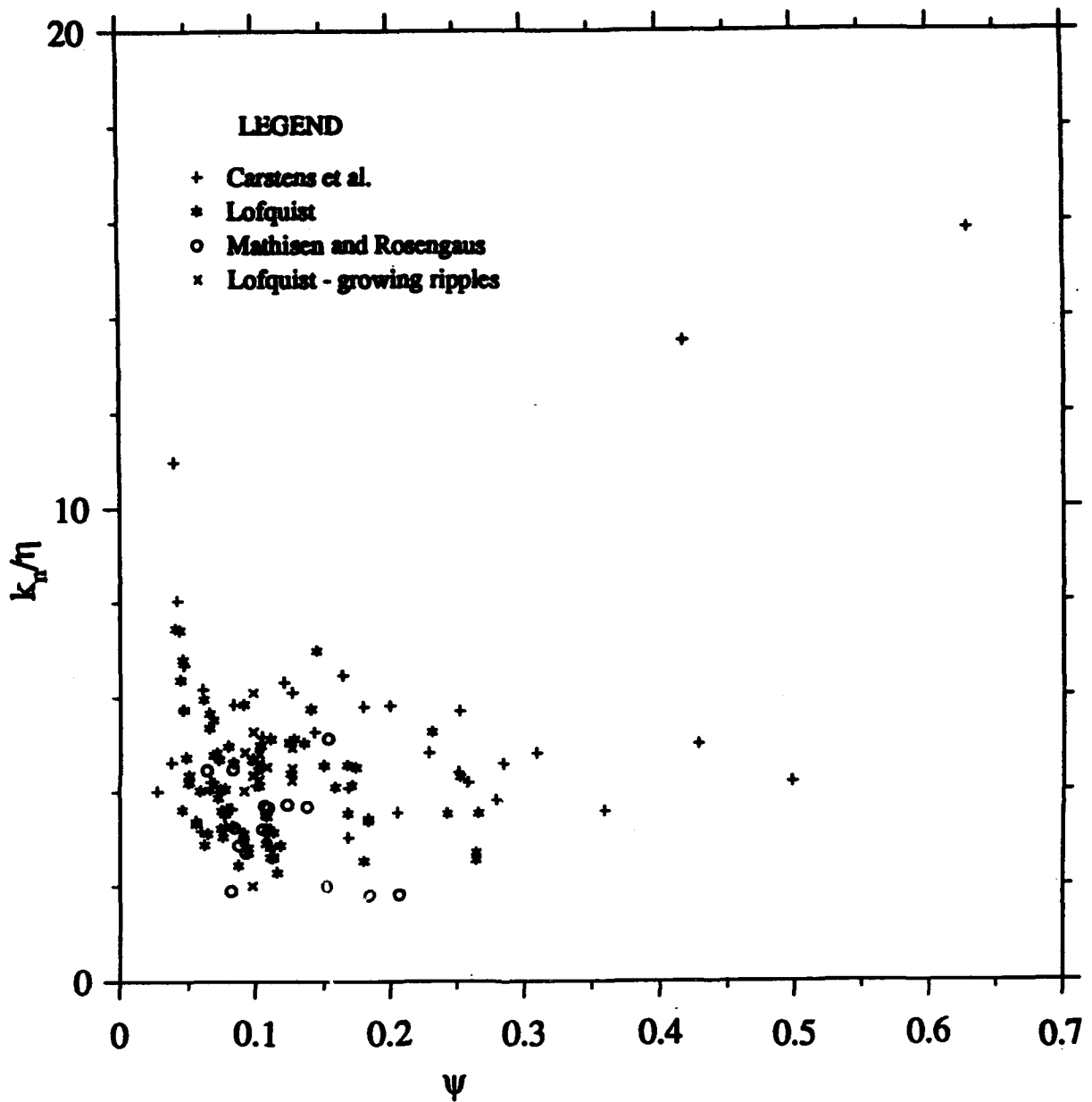
Figure 19. The ratio of equivalent roughness to ripple height, k_n/η, plotted against the Shield parameter, ψ, for the regular wave data of Carstens et al. (1969), Lofquist (1986), Rosengaus (1987), and Mathisen (1989)

for the data of Carstens et al., Lofquist, and Mathisen and Rosengaus, respectively.

188. These two representations are compared in Figure 20 which is a plot of k_n/η against the ripple steepness η/λ. It is seen that the solid line representing the equation

$$k_n = 4\eta \tag{35}$$

is a better fit than the dashed line which is equation (34) with a constant of 26. The use of an expression that had the form of equation (35) multiplied by some power of the ripple steepness did not improve the fit given by equation (35). Therefore this simple expression is proposed to predict the equivalent roughness of a rippled bed for regular waves.

189. The measured values of the friction factor are plotted against A_b/k_n in Figure 21 with k_n calculated from equation (35), along with the Grant-Madsen friction factor relationship of equation (7). If equation (35) is a perfect correlation all the points should fall on this curve. It is encouraging that the data from growing ripples measured by Lofquist (1986) are also well represented by the curve even though they were not used to find the best-fit coefficient in equation (35).

190. It should be recalled that the fixed bed experiments of Sleath (1985) and Bagnold (1946) gave values of 3 and 5, respectively, for the constant in equation (36). The range is the same as was obtained for the three data sets for movable sand beds. This indicates that the bulk of the energy dissipation over a rippled sand bed is due to the form drag created by the ripples and not to the skin friction caused by the sand grains, contrary to the results obtained by Vitale (1979).

191. Jonsson (1980b) suggested that the equivalent roughness, k_n, for a movable bed could be represented by $k_n = 250$ d. The ratio k_n/d is plotted against the Shields parameter ψ in Figure 22. The overall fit to the equilibrium ripple data results is a relative error of 1.44 for the relation $k_n = 480$ d. While this value is different from that suggested by Jonsson (1980b) it should be remembered that he used a different friction factor relation to calculate k_n. It could be argued that the data in Figure 21 could be fit better by a relation of the form $k_n/d = f(\psi)$.

Figure 20. The ratio of equivalent roughness to ripple height, k_n/η, plotted against the ripple steepness, η/λ, for the regular wave data of Carstens et al. (1969), Lofquist (1980), Rosengaus (1987), and Mathisen (1989)
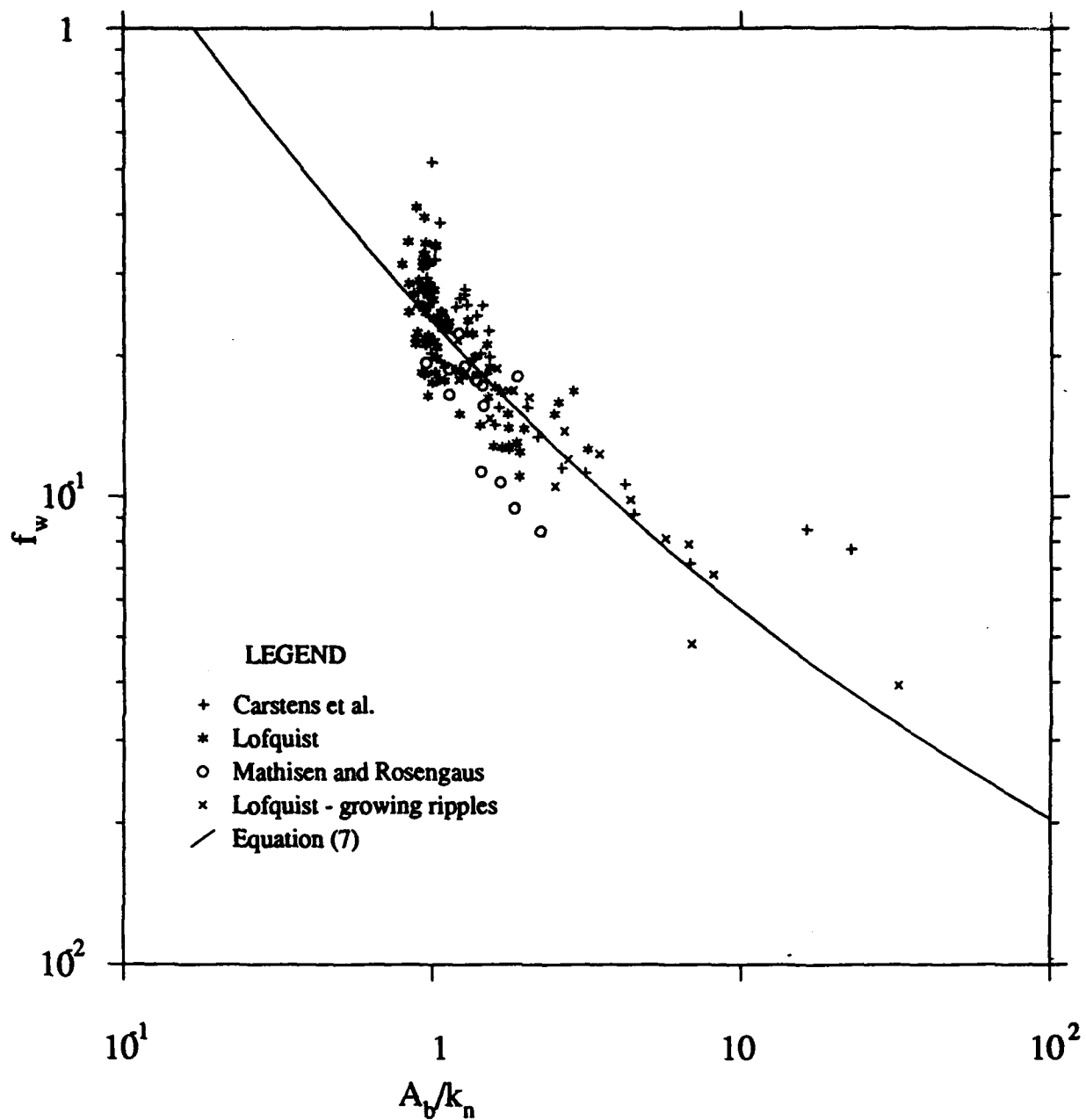
Figure 21. The measured friction factor, f_w, plotted against the relative roughness, A_b/k_n, for the regular wave data of Carstens et al. (1969), Lofquist (1980), Rosengaus (1987), and Mathisen (1989) along with a line representing equation (7). k_n is calculated from equation (35).

73

However, it was found that using an expression $f(\psi) = a\psi^b$ only decreased the relative error to 1.43. This is greater than the error of 1.27 obtained using equation (35). Therefore it was concluded that k_n was not well represented by a function of d.

192. Figure 22 shows that while the data as a whole show considerable scatter, some individual data sets are well represented by a constant value of k_n/d. When this relation is fit to the individual data sets the resulting errors are 1.25, 1.44, and 1.23 for the data of Carstens et al., Lofquist, and Mathisen and Rosengaus, respectively. It is seen that the errors for the data of Carstens et al. and Mathisen and Rosengaus compare favorably with the fit using equation (33). However, it was also found that the error obtained with k_n/d set to a constant was 1.75 for the growing ripple data of Lofquist. Thus it is seen that k_n correlates well with the grain diameter only for the data sets that had equilibrium ripples with a "natural," i.e., not affected by end conditions, geometry.

193. This indicates that the correlation between k_n and d for "natural" ripples occurs because there is a correlation between d and the ripple geometry for "natural" ripples formed by regular waves. It was found in Part III that this geometry is quite different from that seen in the field. Therefore the use of regular wave laboratory data to develop a relation between the grain diameter and the equivalent roughness would result in an expression that is not applicable in the field.

Effect of Sediment Transport

194. Figure 19 shows that there are two data points, from experiments with a large value of ψ, that show roughnesses much larger than what is predicted by equation (35). These points correspond to the two points in Figure 21, marked by + symbols, that lie above the solid line at a value of A_b/k_n of around 15. This was attributed by Grant and Madsen (1982) to the increased sediment transport that takes place when the shear stress, and therefore ψ, is high. It is seen from the figure that only Carstens et al. have carried out measurements of dissipation in the range $\psi > 0.3$.

195. Grant and Madsen (1982) derived an expression for the equivalent roughness due to a near-bottom layer of intensive sediment transport. Their analysis suggested that this roughness, indicated by k_{ns}, was of the form

74
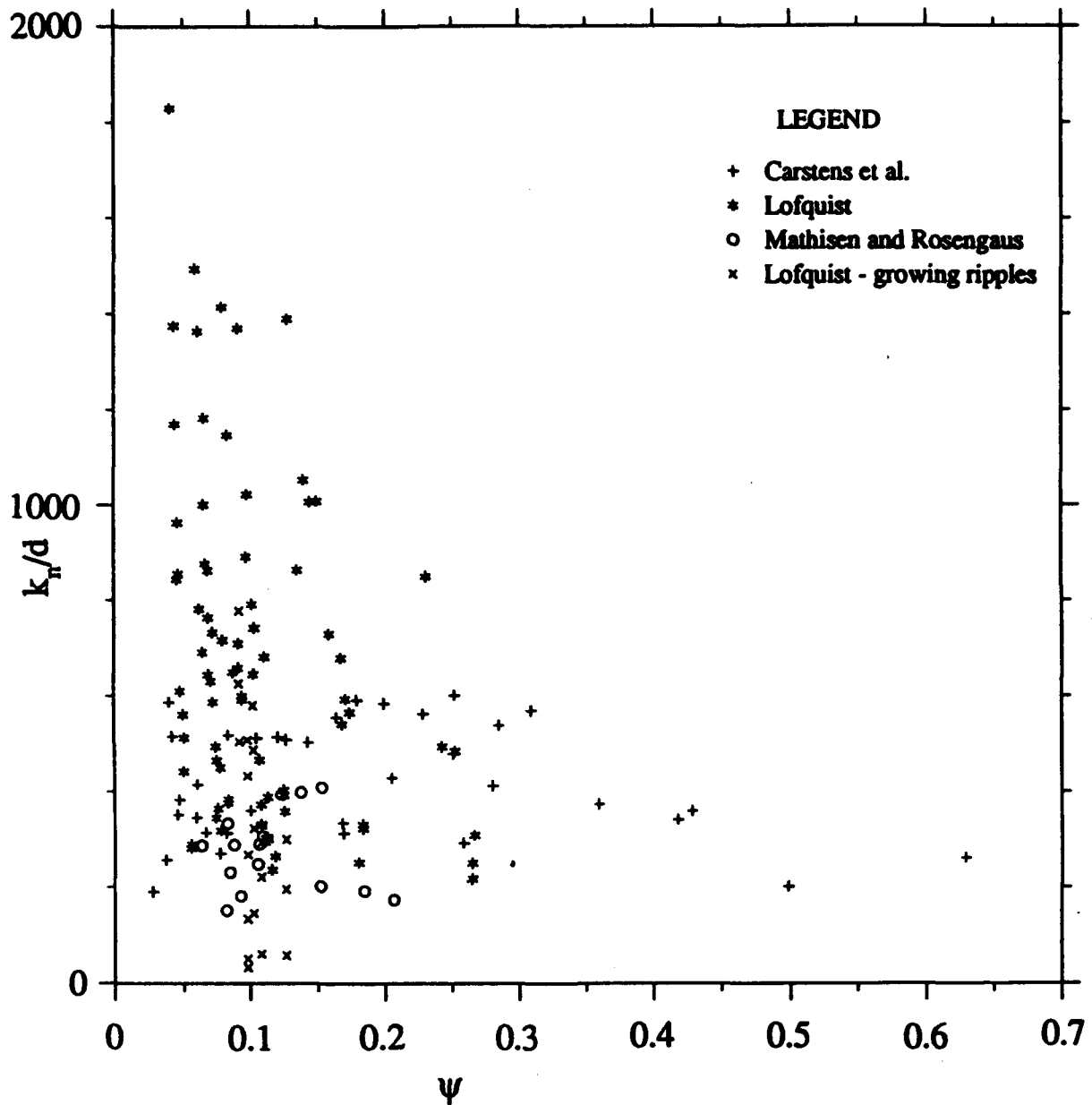
Figure 22. The ratio of equivalent roughness to grain diameter, k_n/d, plotted against the Shield parameter, ψ, for the regular wave data of Carstens et al. (1969), Lofquist (1980), Rosengaus (1987), and Mathisen (1989)

$$k_{ns} \sim d(\sqrt{\psi} - 0.7\sqrt{\psi_c})^2 \qquad (36)$$

where ψ_c is the critical Shields parameter for the initiation of motion. Nielsen (1983) suggested a relation of the form

$$k_{ns} \sim d(\psi - \psi_c)^{\frac{1}{2}} \qquad (37)$$

Another equation for k_{ns} was suggested by Raudkivi (1988). It is shown in Appendix A that the friction factors he derived from the data of Carstens et al. are open to question. Therefore his equation will not be analyzed here. Wilson (1989) suggested an expression of the form

$$k_{ns} \sim d\psi \qquad (38)$$

that was based on the results of experiments using steady flow. Although it was not clear what shear stress is to be used to calculate the Shields parameter in this equation, the fact that it corresponds to sheet flow conditions indicated that the total bed shear stress should be used here.

196. In order to examine the validity of these three equations it is necessary to have energy dissipation measurements made under conditions of sheet flow. The only measurements known that approximate these conditions are five runs from Carstens et al. (1969). These were flat bed runs performed at orbital amplitudes much higher than those required for the spontaneous formation of ripples. This means that a moving layer of sand must have been present on the bed.

197. The ratio k_{ns}/d obtained from these five runs is plotted against ψ in Figure 23 along with the best-fit forms of equations (36) and (37). These best-fit forms have multiplicative constants of 850 and 360 for equations (36) and (37), respectively. It is seen from the figure that equation (37) is the best at matching the trend of the data. Since the measured friction factor can be used to obtain the total shear stress for these runs a best-fit coefficient for equation (38) can also be obtained. This was found to be 60, which was larger than the value of 5 obtained by Wilson (1989) from steady flow measurements.

198. However, it should be noted that laboratory data on ripple
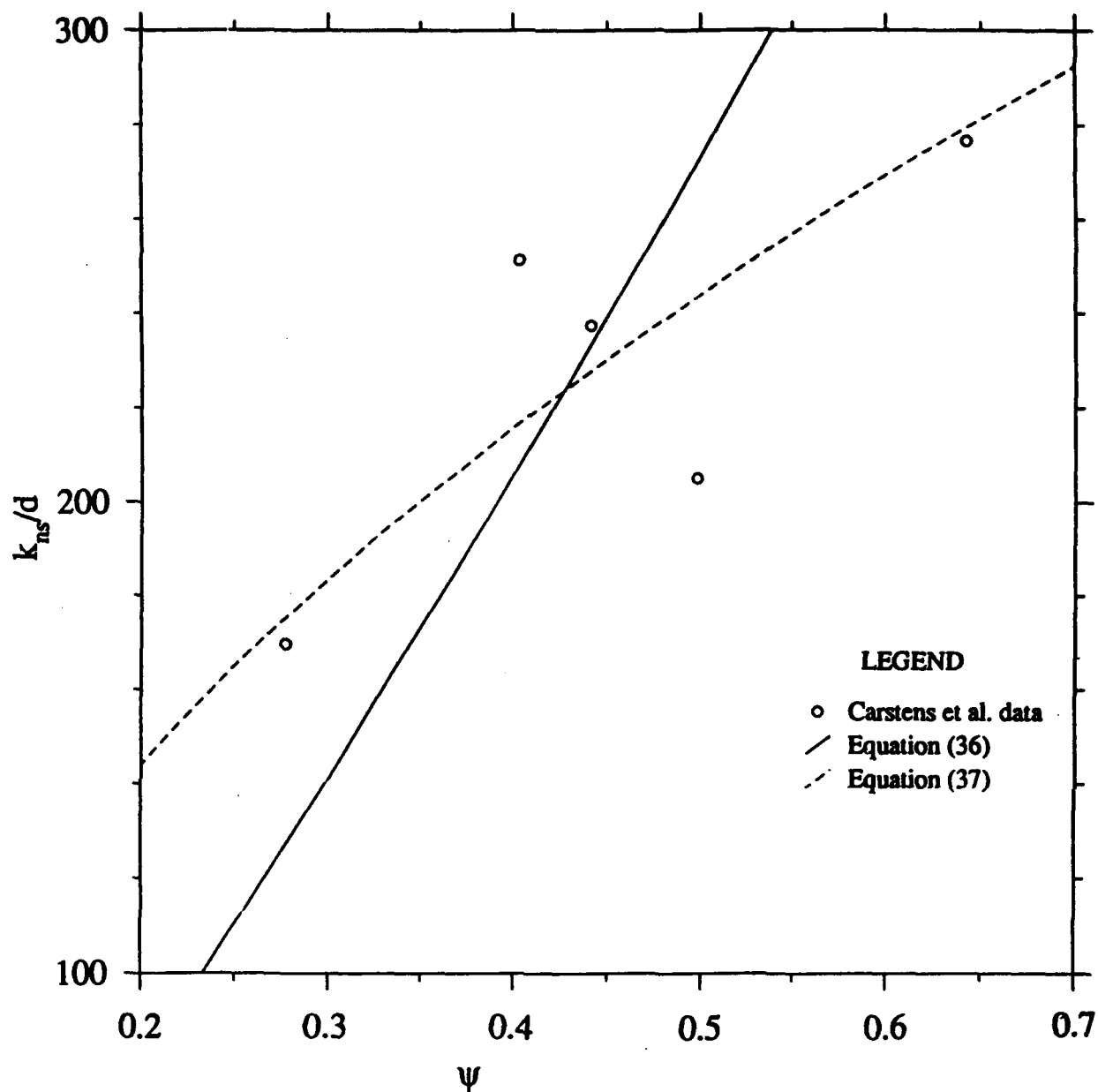
Figure 23. The ratio of equivalent roughness due to sediment transport, k_{ns}, to the grain diameter, d, plotted against the Shields parameter, ψ, for the unstable flat bed data of Carstens et al. (1969), along with the best fit forms of equations (36) and (37)

geometry show that sheet flow actually begins after the Shields parameter exceeds a value of about 0.8. Therefore if these runs had been continued they would ultimately have resulted in a rippled bed being formed. A final decision on the validity of these expressions should not be made until data from the real sheet flow region are available.

199. Thus it appears that the movement of grains on a flat bed can cause an effective roughness that is more than two orders of magnitude greater than the grain diameter. The effect of grain motion on a rippled bed can then be accounted for by defining the equivalent roughness as

$$k_n = k_{nf} + k_{ns} \tag{39}$$

where k_{nf} is the roughness due to the bedforms and is quantified by equation (35). It was attempted to fit the observed values of k_n using equation (39) with k_{ns} calculated using each of equations (36), (37), and (38).

200. The best fit was obtained when equation (36) with a modified coefficient was used to represent the roughness due to grain motion. The resulting equation is

$$k_n = 4\eta + 340d(\sqrt{\psi} - 0.7\sqrt{\psi_c})^2 \tag{40}$$

The value of the relative error was 1.26 for the data from equilibrium ripples. This is only a small improvement over the value of e when the grain motion was disregarded due to there being only a few data points in the region of high shear stress. The coefficient used for the sediment transport term has been reduced to 340 from the value of 850 that was the best fit to the flat bed data. This may be because the sediment transport flat bed runs included some bed form drag as the bed becomes slightly rippled during those runs.

201. When equation (37) is used to calculate k_{ns} in equation (39) the resulting best fit has an error of 1.29. The fit is not as good as with equation (36) because it dies down more slowly at small values of ψ. It is necessary for the function used for k_{ns} to be small at low ψ because it is only the fit to the data of Carstens et al., which were over a large range of ψ, that are improved by the inclusion of the sediment transport term.

The fits to the other data sets were not improved by the addition of this term as they were mostly at very low values of ψ.

202. Figure 24 shows the measured values of the friction factor plotted against A_b/k_n with k_n calculated from equation (40). The solid line represents equation (7). Comparing Figures 21 and 24 it is seen that the most important difference is that the two points that were above the solid line in Figure 21 with $A_b k_n$ around 15 are moved to the left in Figure 24 and lie closer to the solid line. All the other data points have been shifted a small distance to the left due to the inclusion of the sediment transport term in equation (40).

203. Therefore the only significant effect of the sediment transport correction is to account for the two aberrant points in Figure 19. It should be noted that Figure 19 shows that there are two other data points in the set of Carstens et al. with the Shields parameter between 0.4 and 0.5 that do not show an increased roughness. This raises the question of whether the two aberrant points are due to experimental error.

204. Thus both equations (35) and (40) are proposed as predictive relations to calculate the equivalent roughness of a rippled sand bed. Equation (35) has the advantage of simplicity and ease of calculation. Equation (40) includes a correction for the effect of sediment transport that has some support from the experimental data but is more complicated in form. The final decision on which equations should be applied is deferred until they are compared over a range of flow conditions in Part V.

Irregular Waves

205. The only measurements of energy dissipation over a rippled sand bed by irregular waves are those of Rosengaus (1987) and Mathisen (1989) in a wave flume. Before discussing these results it is necessary to define energy dissipation and the friction factor under an irregular wave motion. The energy dissipation factor under regular waves was defined in equation (11) which relates the bottom velocity to the energy dissipation.

206. In this report irregular waves are considered to be represented by the root-mean-square wave height, H_{rms}, and the average period. Using these values along with the flow depth it is possible to calculate a bottom velocity, u_{brms}, that represents the bottom wave motion. The energy dissipation that is relevant is the total loss of energy from all
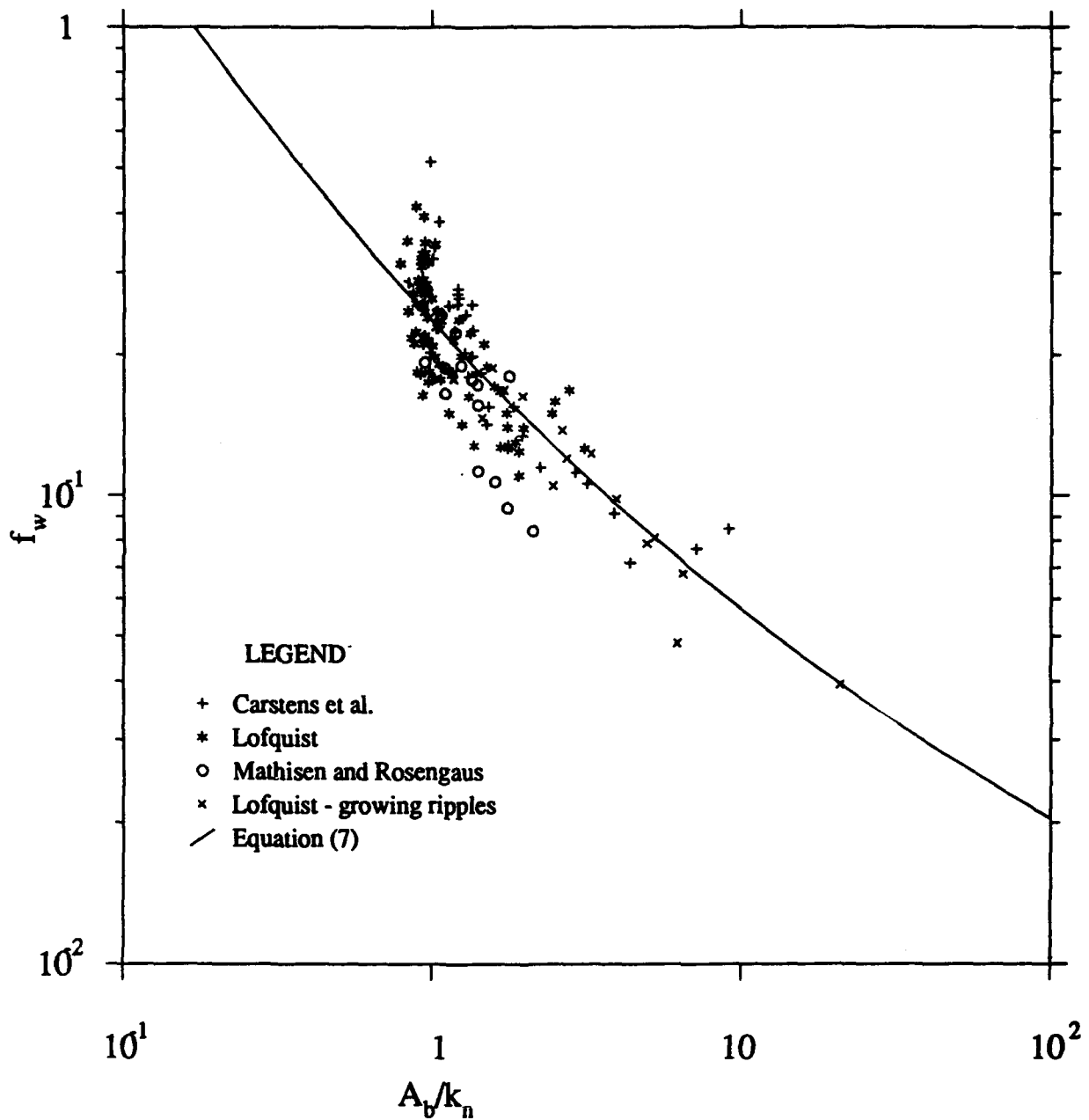
Figure 24. The measured friction factor, f_w, plotted against the relative roughness, A_b/k_n, with k_n calculated from equation (40), for the regular wave data of Carstens et al. (1969), Lofquist (1980), Rosengaus (1987), and Mathisen (1989) along with a line representing equation (7)

80

components of the wave field that is due to bottom friction. With these definitions an energy dissipation factor, f_{erms}, for irregular wave motion can be defined by

$$E_d = \frac{2}{3\pi}\rho f_{erms} u_{brms}^3 \qquad (41)$$

where E_d is the total energy dissipation.

207. Rosengaus (1987) and Mathisen (1989) measured the energy dissipation for each of several frequency components they combined to obtain an irregular wave motion. Thus the total dissipation can be obtained by summing these values. The value of H_{rms} is found from the amplitudes of the components. The value of the representative friction factor can then be calculated from equation (41).

208. This value together with the representative bottom orbital amplitude A_{brms} defined in equation (28) are used to calculate the equivalent bottom roughness for these experiments. The ratio k_n/η is plotted against the Shields parameter, ψ, for the regular and irregular wave data of Rosengaus and Mathisen in Figure 24. The representative wave was used to calculate the Shields parameter.

209. Figure 25 shows that the values of k_n/η for the irregular waves are slightly less than those for the regular waves. The best fit value for this ratio is 2.5 with a relative error of 1.39 for the irregular wave data while it is 3.0 for the regular wave data. Use of $k_n/\eta = 3$ for the irregular wave data results in the relative error increasing to 1.41. This shows that the relative error is not very sensitive to the constant of proportionality used due to the scatter of the data.

210. It should be noted here that if the significant wave had been used as the representative wave the bottom velocity used in equation (41) would have been greater than u_{brms} by a factor of $\sqrt{2}$. This would have resulted in the calculated friction factors being reduced by a factor of $2\sqrt{2}$ leading to equivalent roughnesses that would be much lower than those obtained with H_{rms} as the representative wave and also much lower than the values obtained with regular waves. Therefore it is seen that the use of H_{rms} leads to a scaling of the equivalent bottom roughness that is much closer to that obtained from regular waves than the scaling calculated using the
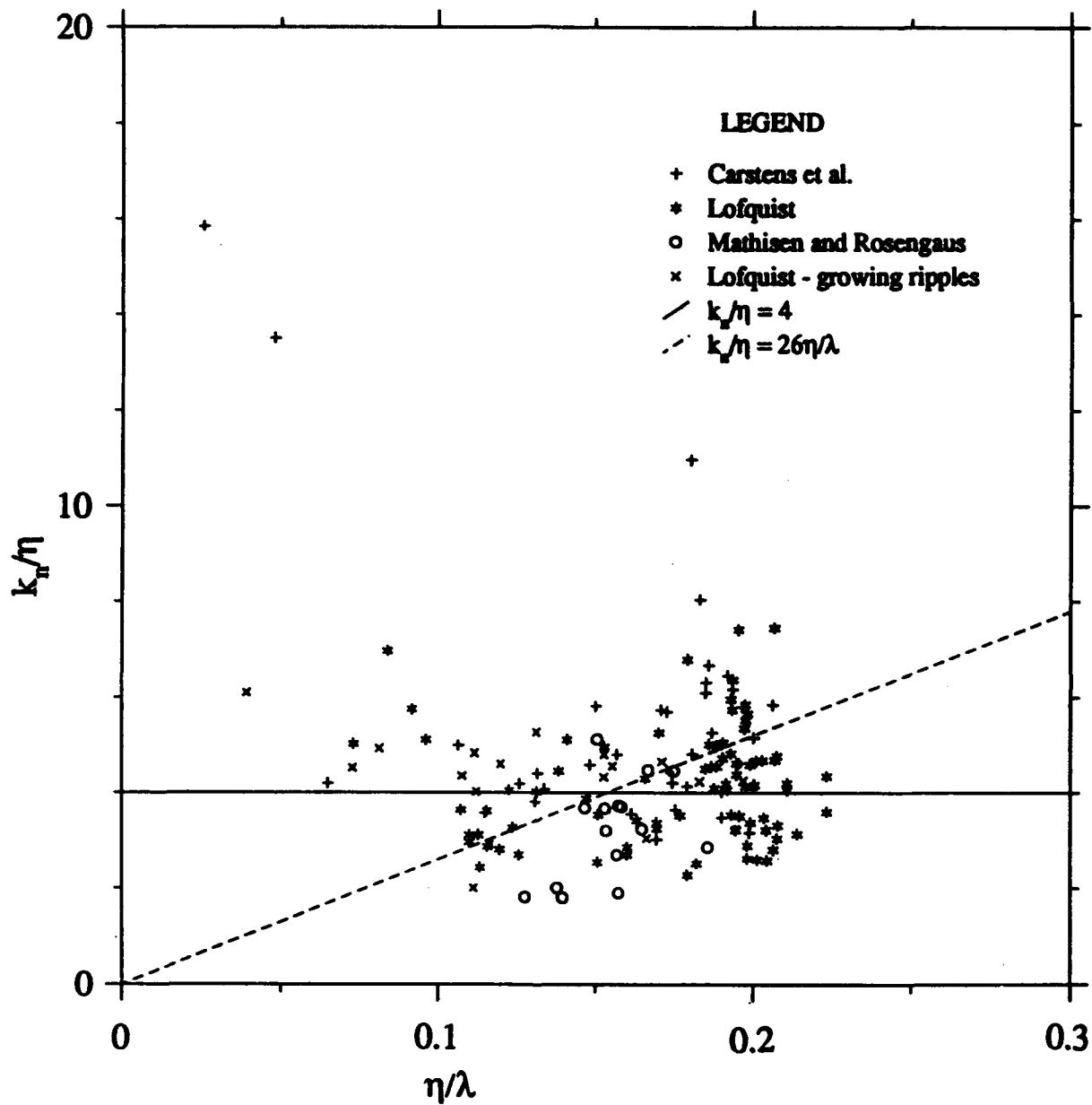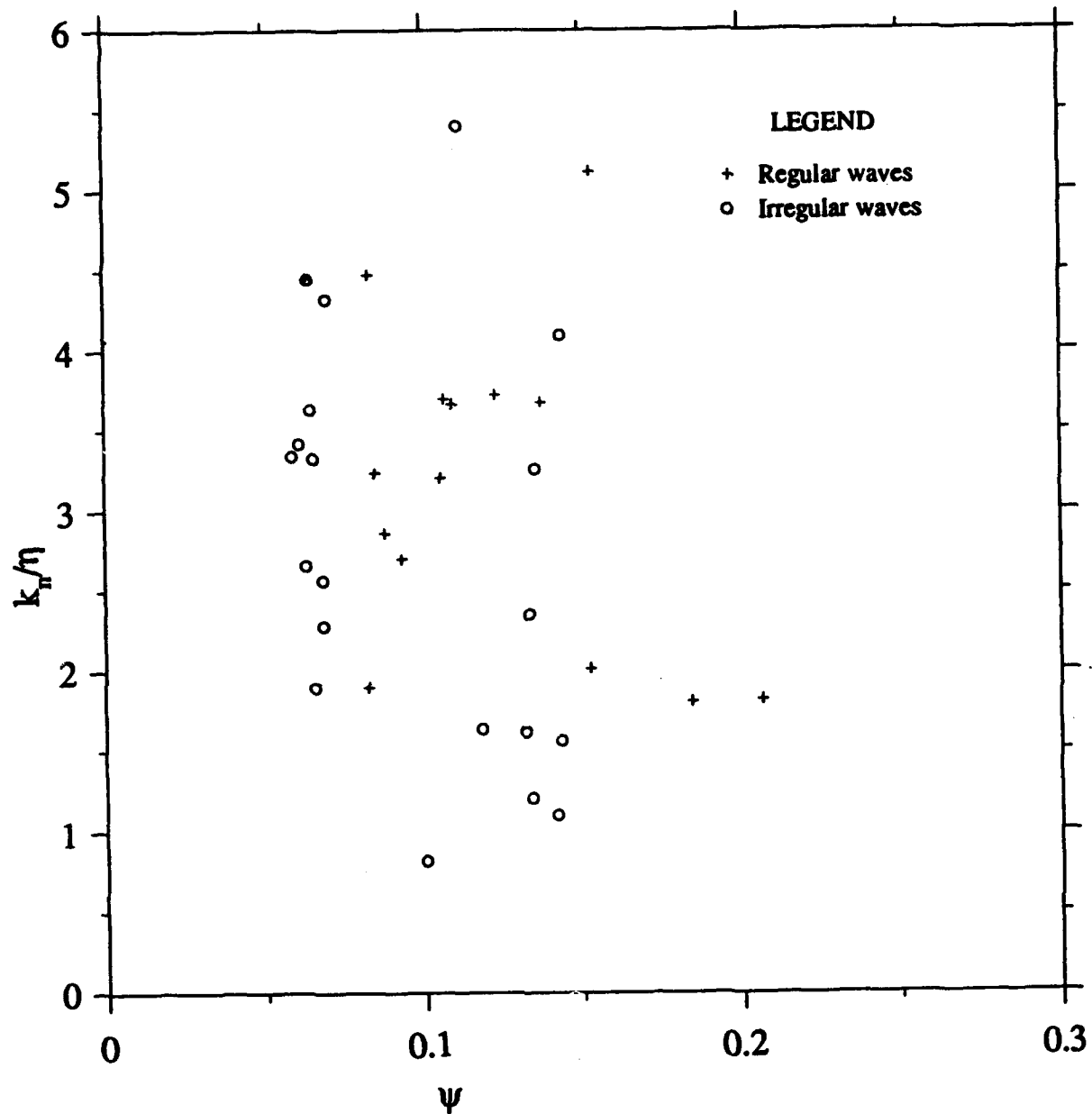
Figure 25. The ratio of equivalent roughness to ripple height, k_n/η, plotted against the Shields parameter, ψ, for the irregular wave data of Rosengaus (1987) and Mathisen (1989)

significant wave.

211. The objective of this part is to develop a relation between ripple geometry and the equivalent bottom roughness that would be applicable under irregular field waves. Expressions for the equivalent roughness under regular waves were proposed in equations (35) and (40). The data plotted in Figure 24 are the only data available at present that can be used to decide whether this relationship is applicable for irregular waves as well.

212. While the best-fit value for k_n/η is smaller for the irregular wave data the use of the best-fit value for the regular wave data does not change the relative error significantly. Therefore, bearing in mind that both the number of data and the range of ψ are limited, and considering the errors involved in predicting the ripple geometry in the field, it seems reasonable to ignore this difference and consider that the equivalent roughnesses under the irregular and regular waves in these experiments are the same.

213. The best-fit value for the ratio k_n/η obtained from the data of Mathisen and Rosengaus is smaller than the value in equations (35) and (40). However, the data of Carstens et al. suggest a higher value than what is used in these expressions. These differences can be ascribed to the differences in experimental technique. Thus, it can be concluded that these equations are the best relations for the prediction of the equivalent roughness that can be made using the available measurements of energy dissipation over a movable bed. It should be kept in mind that these are based mainly on regular wave data at low values of ψ and that their extension to high values of ψ and irregular waves is based on the very small number of measurements made under these conditions.

PART V: EXAMPLE CALCULATIONS AND COMPARISON WITH OTHER RELATIONS

Proposed Models

214. The predictive relations for ripple geometry in the field that were developed in Part III can be combined with the expression for the equivalent roughness proposed in Part IV to calculate the friction factor that can be expected in the field over a sand bed. The required parameters are the root-mean-square wave height, the averaged period, the water temperature, and the sand grain diameter.

215. It was found that the field ripple geometry was well correlated by the parameter X, defined by

$$X = \frac{4\nu u_{brms}^2}{d((s-1)gd)^{3/2}} \qquad (42)$$

where u_{brms} is the bottom velocity obtained from the representative wave that has a height equal to H_{rms}, the root-mean-square wave height, and a period equal to the averaged wave period.

216. The ripple height is given by

$$\frac{\eta}{A_{brms}} = \begin{array}{ll} 0.27X^{-0.5} & X < 3 \\ 0.47X^{-1.0} & X > 3 \end{array} \qquad (43)$$

where A_{brms} is the orbital amplitude based on the representative wave. This relationship is observed to exist for the range $0.2 < X < 50$. The equivalent roughness k_n is then found from either the simple form of equation (35), i.e.,

$$k_n = 4\eta \qquad (44)$$

or from the more complicated form given by equation (40), i.e.,

$$k_n = 4\eta + 340d(\sqrt{\psi} - 0.7\sqrt{\psi_c})^2 \qquad (45)$$

84

which includes a correction for the effect of sediment transport. The use of k_n and A_{brms} in equation (7) results in a friction factor that can be used to predict the total energy dissipation by the use of equation (41).

Example Calculation

217. For example let us consider a wave field with a root-mean-square height of 1.5 m and an average period of 6 seconds propagating in a water depth of 10 m over a sand bed that has a diameter of 0.2 mm. The bottom orbital amplitude is found to 0.44 m from equation (24). Assuming $\nu =$ 0.01 cm^2/s this gives the value of X from equation (42) as 23.0. The ripple height corresponding to this value of X is 0.9 cm from equation (43).

218. The Shields parameter for these conditions is found to be 0.25 from equation (15) while the critical Shields parameter is 0.05 from Figure 5. Using these values k_n is calculated as 3.6 cm and 4.4 cm from equations (44) and (45) respectively. The Grant-Madsen friction factor relationship (equation (7) or Figure 2) is then used to calculate the friction factor. The values for this case are 0.051 and 0.057 when equations (44) and (45) are used to calculate the equivalent bottom roughness.

219. This example can also be used to get an idea of how much uncertainty there will be in the final predicted value of the friction factor. The relative error in the ripple height prediction was found to be 1.55 in Part III. Thus the calculated ripple height could range from 0.58 cm to 1.4 cm. The friction factors corresponding to these ripple heights are found to be 0.0414 and 0.065 respectively, when equation (44) is used. Since the relative error in calculating the friction factor from the geometry is 1.27 from Part IV, this would result in range of values from 0.0326 to 0.0826 for the friction factor about the calculated value of 0.051. This range corresponds to a relative error of around 1.6. Thus we see that the total relative error is less than the multiple of the two component errors because the friction factor is not very sensitive to errors in the equivalent roughness.

220. For the remainder of this section the prediction of the friction factor using equations (44) and (45) will be referred to as models 1 and 2, respectively.

Other Existing Models

Model 3

221. Grant and Madsen (1982) suggested that the equivalent roughness for a rippled bed was given by

$$k_n = 28\eta\frac{\eta}{\lambda} + 504d(\sqrt{\psi} - 0.7\sqrt{\psi_c})^2 \tag{46}$$

This equation will also be used to calculate the friction factor with the geometry obtained from the field relations equations (30) and (31) in order to see how the results compare with those obtained from equations (44) and (45).

Model 4

222. The only previous model proposed for the friction factor under field conditions was that of Nielsen (1983). He based his formulation on the significant wave height and used equation (6) with an upper limit of 0.3 as his friction factor expression. This model calculated k_n by the equation

$$k_n = 8\frac{\eta^2}{\lambda} + 190(\psi - \psi_c)^{1/2} \tag{47}$$

The ripple height was predicted by the relation

$$\frac{\eta}{A_b} = 21\theta^{-1.85} \tag{48}$$

where θ is defined by equation (25) and the ripple steepness was calculated from

$$\frac{\eta}{\lambda} = 0.342 - 0.34\psi^{0.25} \tag{49}$$

with ψ calculated assuming $k_n = 2.5d$ in equation (6).

223. Equations (48) and (49) for field ripple geometry were put forward by Nielsen (1981) and were based on the significant wave height. However, when considering energy dissipation Nielsen (1983) suggests the

86

root-mean-square wave height as the equivalent wave height for irregular waves. In other words the energy dissipation is calculated from equation (41) using the friction factor derived from equations (47), (48), (49), and (6). This means that as far as the energy dissipation is concerned this friction factor can be compared directly with the value obtained from the model developed here.

Model 5

224. Another type of predictive relation for the friction factor is a direct prediction from the wave and sediment parameters, i.e., a prediction that does not consider the ripple geometry. An example is the equation proposed by Vongvissesomnjai (1987, 1988). He obtained this relation by fitting it to the data of Carstens et al., and Lofquist (1980) along with data where the friction factor was not measured directly. The result was the relation

$$f_w = 0.077\theta^{-0.31}\left[\frac{a}{d}\right]^{0.16}S_*^{0.42} \tag{50}$$

Model 6

225. Madsen et al. (1990) obtained a formula similar to equation (48) based solely upon their laboratory measurements of energy dissipation under irregular waves. They used the equivalent bottom orbital velocity and amplitude defined in equations (18) and (20) to define the equivalent wave conditions, a method that is different from the root-mean-square wave approach. However, if the comparison is done for a specified bottom orbital diameter and period the resulting friction factors will be comparable as far as energy dissipation and shear stress are concerned. The equation suggested by Madsen et al. is

$$f_w = 0.29(\psi/\psi_c)^{-1.5} \tag{51}$$

with ψ calculated from equation (15).

Comparison of Models

226. Thus we have outlined six models that could be used to predict the

87

friction factor in the field. The first three are based on the ripple geometry as given by equations (30) and (31) with the equivalent roughness calculated from equations (44), (45), and (46) respectively. The friction factor is then found by using equation (7) or from Figure 2.

227. The fourth model is the formulation of Nielsen (1983) with the geometry calculated using equations (48) and (49), the roughness from equation (47), and the friction factor from equation (6) with an upper limit of 0.3. The fifth and sixth models are the direct predictions of equations (50) and (51). It should be remembered that with the exception of model 4, which uses the significant wave parameters, all these models are to be used with the root-mean-square wave parameters.

228. These relations will be compared under conditions for which ripples are known to exist in the field in order to see how the predictions behave over a range of conditions. Since the models are formulated in terms of different non-dimensional parameters it is not possible to plot all the predicted values against the same non-dimensional variable. Instead, the comparison will be done for a specific sand grain diameter. It was decided to select d = 0.2 mm because this is a typical value seen in the field.

229. Two further parameters are needed to specify the wave motion. This will be done by specifying an average period and calculating the friction factor from each model for a range of values of A_{brms} such that the value of X is always in the range $0.2 < x < 50$. Since the model of Nielsen (1983) was formulated using the significant wave height, A_{brms} was multiplied by $\sqrt{2}$ before it was used in equations (47)-(49).

230. The parameter X was used to define the limits of the range of A_{brms} because it was the empirical parameter used to correlate the field data. However, unlike the Shields parameter, it is not a physically significant parameter in defining the initiation of motion and the disappearance of ripples. In this calculation the values of Shields parameter corresponding to X = 0.2 were found to be as low as 0.018 which was well below the critical values for the initiation of motion of 0.05 for this particular grain diameter. Therefore it was decided to set the lower limit of A_{brms} as the greater of the values corresponding to X = 0.2 and $\psi = 0.5\psi_c$. Similarly the upper limit of A_{brms} was defined by X = 50 and $\psi = 1.0$. For the

calculations shown here the largest values of ψ were about 0.5.

231. The results of models 1, 2 and 3 are shown as a plot of friction factor against A_{brms} for the case with d = 0.2 mm and an average period of 6 seconds in Figure 26. This period is at the lower end of the range observed in the field. The ripple geometry is calculated from equations (30) and (31) using the root-mean-square wave height. For this period a value of A_{brms} = 30 cm means values of the root-mean-square wave height of 0.37 m, 0.68 m, and 5.75 m in water depths of 5 m, 10 m, and 30 m, respectively.

232. The figure shows that the predictions of models 1 and 2 are identical for small values of A_{brms}. This is because the sediment transport correction is negligible at low flow intensities. The kink in the curves corresponds to the value X = 3.0 above which a different relation is used for the ripple geometry. The curve from model 3 is above the other curves for X < 3.0. This is because the coefficient 28.0 in equation (46) is slightly higher than the best-fit value of 26.0 obtained in Part IV. However, once X is greater than 3.0 this curve decreases faster than the other two curves because equation (46) includes the ripple steepness as well as the height, and the steepness decreases with increased X after X > 3.0.

233. At larger values of A_{brms} the curve from model 1 continues to decrease due to the continued decrease of the ripple height while the other two curves flatten out as the sediment transport term increases in importance. It is seen that for flow conditions corresponding to X = 50, with ψ = 0.5, the predictions of f_w from models 1 and 2 are 0.035 and 0.047, respectively.

234. Figure 27 shows the predicted curves from the same three models for the case of d = 0.2 mm and a period of 12 seconds. This period is chosen from the upper end of the range observed in the field. A value of A_{brms} = 60 cm is equivalent to waves with a root-mean-square height of 0.4 m, 0.58 m, and 1.28 m in water depths of 5 m, 10 m, and 30 m, respectively. The behavior of the three curves is similar to the case with a period of 6 seconds. It is seen that in this case the effect of the sediment transport term, shown by the difference between the curves from models 1 and 2, is smaller than before. When X = 50, and the corresponding
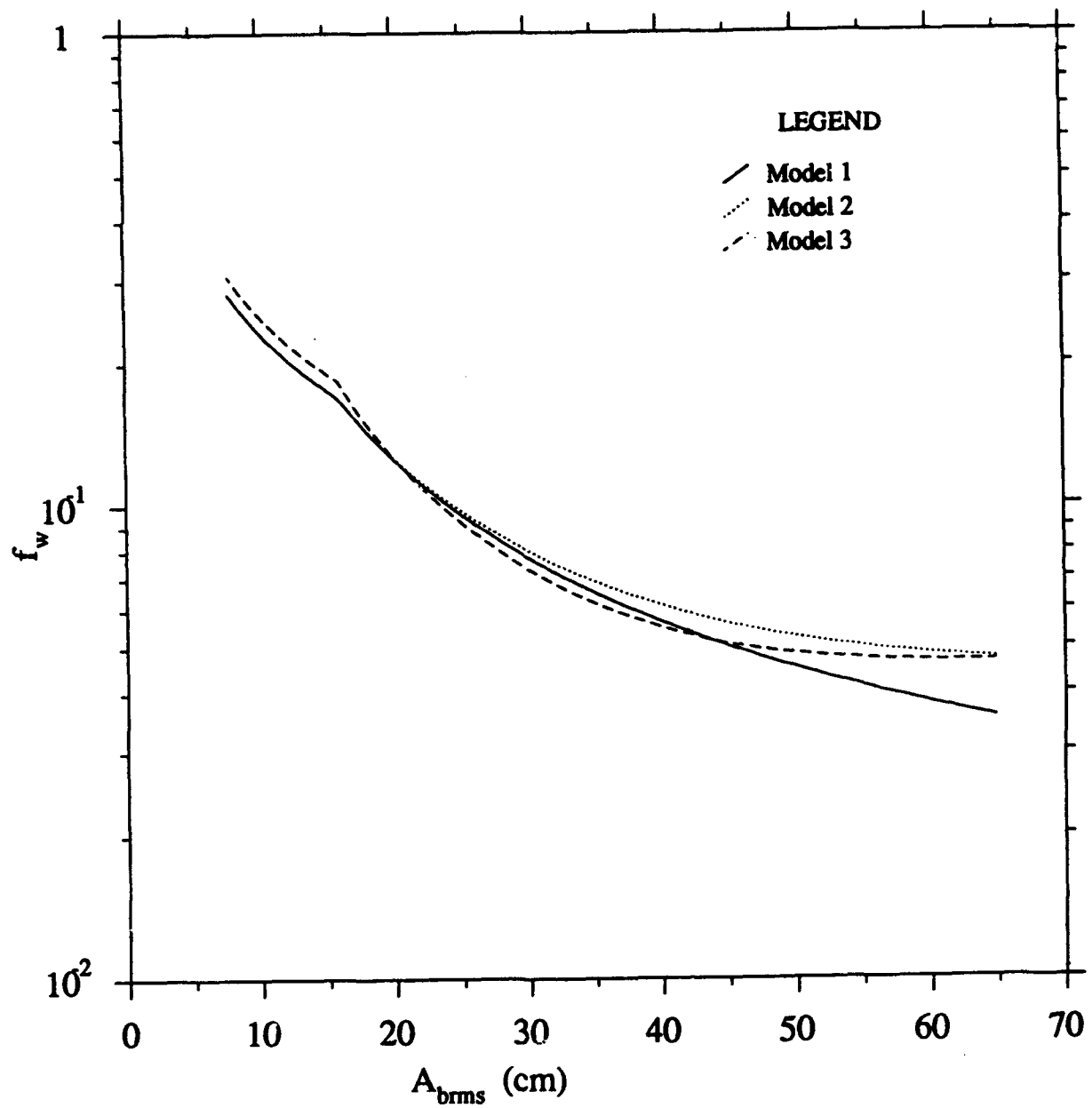
Figure 26. The friction factor, f_w, calculated using models 1, 2, and 3, against A_{brms} for the case with d = 0.2 mm and an average period of 6 seconds
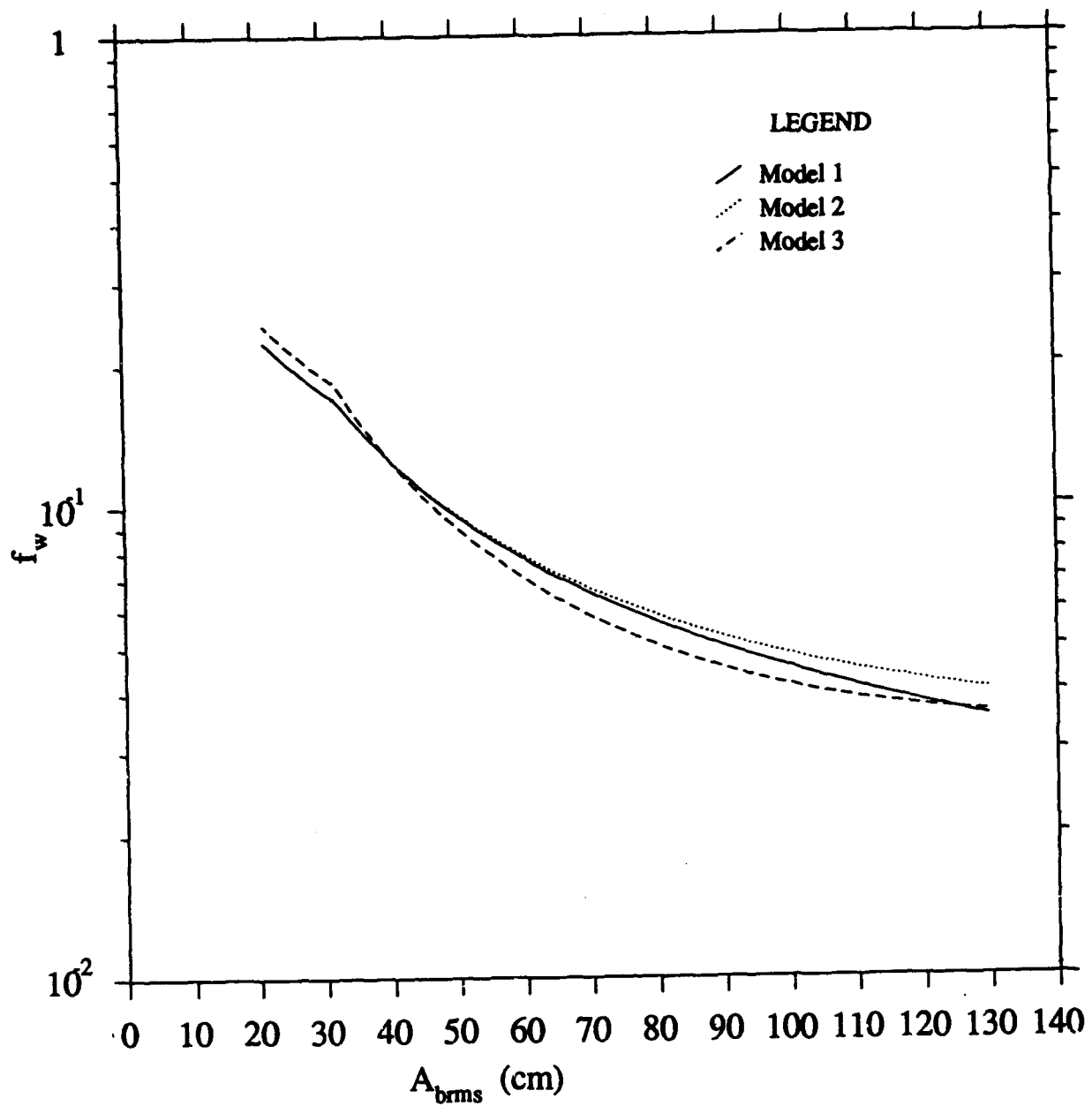
Figure 27. The friction factor, f_w, calculated using models 1, 2, and 3, against A_{brms} for the case with d = 0.2 mm and an average period of 12 seconds

value of ψ is 0.41, the predicted values of f_w are 0.035 and 0.041 from models 1 and 2 respectively.

235. Figure 28 shows the results from models 1, 4, 5, and 6 for the case with d = 0.2 mm and a period of 6 seconds. The four models show considerable differences in the predicted friction factors. For most of the range of A_{brms} the curve from model 5, which is based on regular wave laboratory data, lies above the curves from models 1 and 4, which are based on field ripple geometry. This is due to the differences in ripple geometry between the laboratory and the field. At the higher values of A_{brms} model 5 predicts friction factors that are greater than those predicted by model 1 by a factor of about 1.9.

236. The curve from the Nielsen model, model 4, begins a little higher than the curve from model 1 but drops off much more quickly with increasing A_{brms}. This is because the relation for the ripple height used in this model, equation (48), causes a more rapid decrease of ripple height with increasing flow intensity than does equation (43). The curve from model 4 reaches a constant at higher values of A_{brms}. This is because the sediment transport term in equation (48) yields a constant value of k_n/A_b when A_{brms} is high.

237. The curve obtained using model 6 decreases more steeply than all the other curves. The range of experimental conditions upon which this equation is based is given by Madsen et al. (1990) as $1.2 < (\psi/\psi_c) < 2.5$. In this case these values correspond to A_{brms} between 17 cm and 28 cm. It is seen that in this region the values predicted by model 6 are within the range predicted by the other equations. However, use of this model at large values of A_{brms} results in predicted friction factors that are much lower than those predicted by the other models.

238. Figure 29 shows the curves predicted by model 1, 4, 5, and 6 for the case of d = 0.2 mm and an average period of 12 seconds. It is seen that the curves behave in a manner similar to the preceding case.

239. Since there are no field data against which to compare these predictions the figures discussed above do not give any idea of which method is the best. The comparison serves to highlight the differences between the models. Figures 26 and 27 shows that the inclusion of the sediment transport term in equation (45) resulted in the friction factor
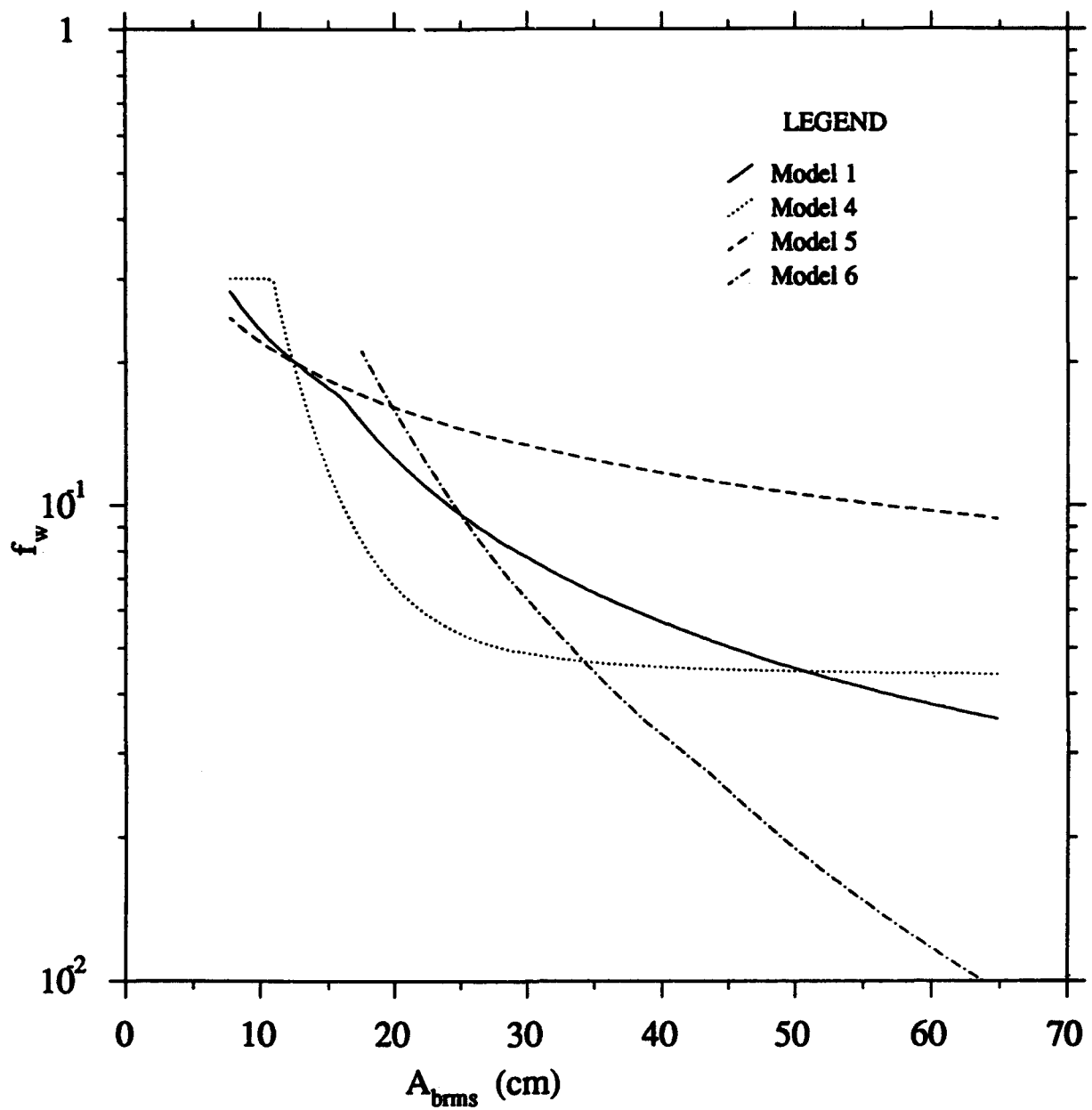
Figure 28. The friction factor, f_w, calculated using models 1, 4, 5, and 6, against A_{brms} for the case with $\measuredangle$ = 0.2 mm and an average period of 6 seconds
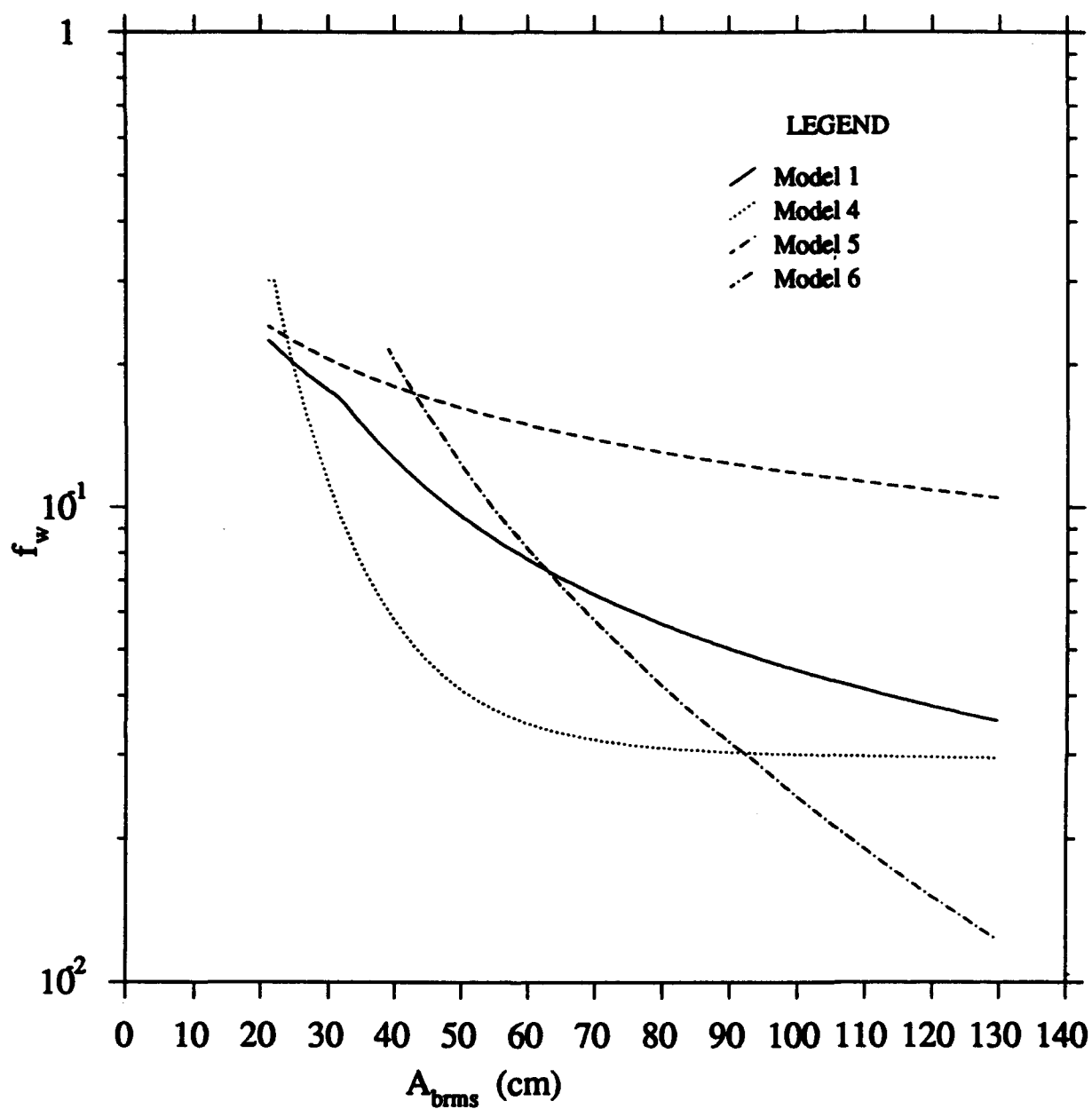
Figure 29. The friction factor, f_w, calculated using models 1, 4, 5, and 6, against A_{brms} for the case with d = 0.2 mm and an average period of 12 seconds

changing from 0.035 to 0.047 in the most extreme instance. The overall
relative error in calcula⁷   ⁻ the friction factor from the flow and
sediment parameters was f   to be about 1.6 in the example equation.
Therefore it is seen that the difference caused by the sediment transport
term, at the most a factor of 1.35, is considerably smaller than the total
error involved in determining the friction factor. Bearing in mind that
the experimental support of the sediment transport correction is very
limited it seems reasonable to neglect this term at the present time.

240. Figures 28 and 29 show that a model based on field ripple geometry
can lead to predictions that are signif⁷ ⁻antly different from formulations
based entirely on regular and irregul   a⁻ laboratory data. The
predictions are different by a factor of 2 for large values of A_{brms}.

241. The curves from model 1 and model 4, which are both based on field
geometry, also show significant differences. The main cause of this is the
difference between the equations used to predict the ripple height. As the
parameter X is found to be superior to θ in correlating the ripple heights,
equation (43) is probably more reliable than equation (46). The equations
used to link the ripple geometry to the friction factor will give similar
results because the model of Nielsen (1983), i.e., model 4, is based on the
data of Carstens et al. (1969) and Lofquist (1980) which were also used in
the present study.

242. Therefore model 1 which has the equivalent roughness calculated by
equation (44), with the ripple height calculated using equation (43) using
the root-mean-square wave height and the average period, is proposed as a
predictive relation for the equivalent bottom roughness over a movable bed
under field conditions. It is emphasized once again that use of the model
should be limited to the range $0.2 < X < 50$.

PART VI: SUMMARY AND CONCLUSIONS

243. The objective of this study was to develop a simple, physically realistic model to predict the friction factor over a movable sand bed under field conditions. Since reliable field measurements are available only for the ripple geometry it was found necessary to use laboratory data in order to formulate some aspects of this model.

244. Laboratory experiments are usually conducted with regular waves while the wave condition in the field is nearly always irregular. The wave motion in the field is also at larger scales than are usually obtainable in the laboratory. Thus it is necessary to investigate how far data from small-scale, regular wave laboratory experiments are applicable in the field. To this end recent data from irregular wave laboratory experiments were included in this study.

245. After discussing the various methods of measuring the friction factor it was concluded that the only reliable method was through measurements of the energy dissipation. Analysis of the data of Lofquist (1986) showed that the friction factor, f_w, defined using the maximum shear stress in equation (1) was nearly equal to the energy dissipation factor, f_e, defined in equation (11) for rippled sand beds. Therefore it was decided to assume that f_w and f_e were equal and to calculate f_w from energy dissipation measurements using equation (11).

246. It was decided to formulate the model in two stages. The first step involved deriving predictive relations for the ripple geometry for a given bottom sediment and a given wave condition. The next step was to develop a relationship between the flow, the ripple geometry, and the resulting friction factor. Combining the two models would lead to the prediction of the friction factor from the wave and sediment parameters.

Summary of Ripple Geometry Analysis

247. The objective of Part III was to compare the existing data on ripples from the laboratory and the field in order to determine the applicability of the laboratory experiments to the field. It was noted that there were only three sets of data on ripples generated by irregular

96

waves in the laboratory while waves in the field are almost always irregular.

248. The ripple length was analyzed in detail because it can be measured in the field with greater reliability than the ripple height. Furthermore the ripple lengths observed in the laboratory under regular waves have a well-defined relationship to the bottom orbital amplitude. The analysis showed that this relationship was quite different for the field ripples when the parameter D_* was sufficiently small. It was found that the few data points from ripples formed by irregular waves in the laboratory at low values of D_* tended to support this conclusion.

249. Thus it was concluded that the differences between laboratory data from regular waves and field data were due to scale effects and the irregularity of the field waves. The data indicated that these differences were significant as D_* decreased below about 0.2 and the Shields parameter increased. Since these conditions are the norm for the field it appears that the present laboratory data cannot be applied to field conditions.

250. This makes it necessary to rely exclusively on field data when proposing predictive relations for field ripple geometry. New relations were proposed for the ripple length, height, and steepness that were improvements on the existing ones. The parameter X, defined in equation (28), was found to correlate the field ripple data well.

251. Previous models for field ripple geometry have been formulated using the significant wave height representation of the wave condition. However, it is seen that the root-mean-square wave height representation is more relevant to energy dissipation. Furthermore it is found in Part IV that use of the root-mean-square wave height results in the equivalent roughness under irregular waves being nearly the same as that under regular waves. For these reasons it was decided to base the predictive relations for a field ripple geometry on the root-mean-square wave height and the average period.

252. Ripple data have been criticized on the grounds that the observed ripples may have been caused by different wave conditions from those recorded. However, the laboratory experiments of Rosengaus (1987) show that when waves are run over an initially rippled bed, the final state is independent of the initial state if the waves are strong enough to cause

motion of the sediment. Also the field data of Dingler and Inman (1976) show that under strong wave conditions the equilibrium ripples can be formed in a few dozen cycles. The fact that data from different investigators correlate provides further evidence of the reliability of the field data.

253. Therefore equations (29), (30), and (31) are put forward as the most reliable predictive relations for field ripple geometry at the present time. It should be remembered that these are empirical relations and as such are only valid in the range of the original data, i.e., for $0.2 < X < 50$.

The Equivalent Roughness

254. In Part IV it was attempted to develop a relation between the flow, the ripple geometry, and the friction factor. This required experiments with the simultaneous measurement of the flow, the ripples, and the energy dissipation. Since such experiments have been done only in the laboratory this section was restricted to the analysis of laboratory data.

255. Analysis of the fixed bed data of Bagnold (1946) and Sleath (1985) showed that for fully rough turbulent flow the equivalent roughness was well represented by the simple relations in equations (33) and (34). The ripple geometries used in these two experiments were thought to represent two extremes between which the geometry of real sand ripples would fall.

256. The analysis of the energy dissipation data over sand ripples showed that the simple relations given by equations (33) and (34) were applicable for the case of a movable bed. The constant of proportionality obtained fell between the values obtained for the fixed bed data, as would be expected from consideration of the geometry in these experiments.

257. The fact that the constants were similar for the flow over smooth field ripples and over sand ripples indicated that most of the flow resistance seen over sand ripples is due to form drag and not to the skin friction drag. The relation between the equivalent roughness and the grain diameter observed by Jonsson (1980b) and Rosengaus (1987) was found to hold only for equilibrium ripples. Since ripples under irregular field waves are not at equilibrium it was decided not to use this correlation. The

equivalent roughness relation given by equation (35) was found to hold for both equilibrium and growing ripples.

258. The corrections for the effect of sediment motion suggested by Grant and Madsen (1982) and Nielsen (1983) were reviewed. It was seen that none of the recently performed experiments were carried out at values of the Shields parameter that were high enough to allow the confirmation of these expressions . Furthermore the steady flow experiments of Wilson (1989) suggest that this correction is likely to be small. Therefore, while the sediment transport term was included in equation (40), it was decided to use both equations (35) and (40) for the comparisons and example calculations.

259. There were only a small number of data, from experiments conducted at small values of the Shields parameter, in which energy dissipation over a rippled sand bed with irregular waves had been measured. The best-fit coefficient for equation (35) using these data was found to be less than that for the regular wave data from the same apparatus. However, the use of the value from the regular wave data resulted in a very small change in the relative error. Therefore it was decided to apply the expressions derived from regular wave data to the case of irregular waves with no change in the coefficients.

Comparison of Models

260. The two models developed in Parts III and IV were compared with each other and with existing models in Part V for a range of conditions typical of the field. It was found that the largest difference caused by the inclusion of the sediment transport term was small compared to the overall errors involved in the prediction of the friction factor. The models based on field ripple geometry were found to give results that were significantly different from the predictions of models based entirely on laboratory data.

261. Therefore the proposed model for the prediction of the friction factor in the field is as follows. The wave conditions are represented by the root-mean-square wave height and the average period. The ripple geometry is found from

$$\frac{\eta}{A_{brms}} = \begin{array}{ll} 0.27X^{-0.5} & X < 3 \\ 0.47X^{-1.0} & X > 3 \end{array} \qquad (52)$$

for $0.2 < X < 50.0$ with X defined by equation (42). The equivalent roughness is given by

$$k_n = 4\eta \qquad (53)$$

and the friction factor is calculated from equation (7) or found from Figure 2.

262. This model is based primarily on ripple geometry measurements made in the field and energy dissipation measurements in the laboratory using regular waves. The experimental basis of the model would be strengthened if more energy dissipation measurements are made with irregular waves, particularly at high values of the shear stress. However, the best way to check the validity of the model is by a carefully conducted field study where the wave attenuation and bottom ripple geometry are measured simultaneously.

REFERENCES

Amos, C. L., Bowen, A. J., Huntley, D. A., and Lewis, C. F. M. 1988. "Ripple Generation under the Combined Action of Waves and Currents on the Canadian Continental Shelf," Continental Shelf Research, Vol. 8, No. 10, pp 1129-1153.

Bagnold, R. A. 1946. "Motion of Waves in Shallow Water, Interaction between Waves and Sand Bottoms," Proceedings of the Royal Society of London, Ser. A, Vol. 187, pp 1-18.

Carstens, M. R., Neilson, F. M., and Altinbilek, H. D. 1969. "Bed Forms Generated in the Laboratory under an Oscillatory Flow: Analytical and Experimental Study," TM-28, U.S. Army Corps of Engineers, Coastal Engineering Research Center.

Dingler, J. R. 1975. "Wave Formed Ripples in Nearshore Sands," Ph.D. thesis, University of California, San Diego.

Dingler, J. R., and Inman, D. L. 1976. "Wave Formed Ripples in Nearshore Sands," Proceedings of the 15th Coastal Engineering Conference, pp 2109-2126.

Goda, Y. 1985. Random Seas and Design of Maritime Structures, University of Tokyo Press.

Grant, W. D. 1975. "Discussion of 'Friction Factor under Oscillatory Waves' by J. W. Kamphuis," Journal of Waterways, Harbors and Coastal Engineering Division, ASCE, Vol. 101, No. WW4, pp 466-467.

Grant, W. D., and Madsen, O. S. 1979. "Combined Wave and Current Interaction with a Rough Bottom," Journal of Geophysical Research, Vol. 84, No. C4, pp 1797-1808.

_____. 1982. "Movable Bed Roughness in Unsteady Oscillatory Flow," Journal of Geophysical Research, Vol. 87, No. C1, pp 469-481.

Inman, D. L. 1957. "Wave Generated Ripples in Nearshore Sands," TM-100, U.S. Army Corps of Engineers, Beach Erosion Board.

Inman, D. L., and Bowen, A. J. 1963. "Flume Experiments on Sand Transport by Waves and Currents," Proceedings of the 8th Coastal Engineering Conference, pp 137-150.

Iwagaki, Y., and Kakinuma, T. 1963. "On the Bottom Friction Factor off the Akita Coast," Coastal Engineering in Japan, Vol. 6, pp 83-91.

_____. 1967. "On the Bottom Friction Factor off Five Japanese Coasts," Coastal Engineering in Japan, Vol. 10, pp 13-22.

Jensen, B. L. 1989. "Experimental Investigation of Turbulent Oscillatory Boundary Layer," Series Paper No. 45, Institute of Hydrodynamic and Hydraulic Engineering, Technical University of Denmark, Lyngby.

Jonsson, I. G. 1966. "Wave Boundary Layers and Friction Factors," Proceedings of the 10th Coastal Engineering Conference, Tokyo, pp 127-148.

_____. 1980a. "A New Approach to Oscillatory Rough Turbulent Boundary Layers." Series Paper 17, Institute of Hydrodynamic and Hydraulic Engineering, Technical University of Denmark.

_____. 1980b. "Discussion of 'Sand Bed Friction Factors for Oscillatory Flow' by P. Vitale," <u>Journal of the Waterways, Port, Coastal and Ocean Division, ASCE</u>, Vol. 105, No. WW3, pp 423-424.

Jonsson, I. G., and Carlsen, N. A. 1976. "Experimental and Theoretical Investigations in an Oscillatory Turbulent Boundary Layer," <u>Journal of Hydraulic Research</u>, Vol. 14, No. 1, pp 45-60.

Kajiura, K. 1964. "On the Bottom Friction in an Oscillatory Current," <u>Bulletin of the Earthquake Research Institute</u>, Vol. 42, pp 147-174.

_____. 1968. "A Model of the Bottom Boundary Layer in Water Waves," <u>Bulletin of the Earthquake Research Institute</u>, Vol. 46, pp 75-123.

Kennedy, J. F., and Falcon, M. 1965. "Wave Generated Sediment Ripples," Report No. 86, Hydrodynamics Laboratory, Dept. of Civil Engineering, Massachusetts Institute of Technology.

Lambie, J. M. 1984. "An Experimental Study of the Stability of Oscillatory Flow Bed Configurations," M.S. thesis, Massachusetts Institute of Technology.

Lee-Young, J. S., and Sleath, J. F. A. 1988. "Initial Motion in Combined Wave and Current Flows," <u>Proceedings of the 21st Coastal Engineering Conference</u>, pp 1140-1151.

Lofquist, K. E. B. 1978. "Sand Ripple Growth in an Oscillatory Flow Water Tunnel," TP-78-5, U.S. Army Corps of Engineers, Coastal Engineering Research Center.

_____. 1980. "Measurements of Oscillatory Drag on Sand Ripples," <u>Proceedings of the 17th Coastal Engineering Conference</u>, pp 3087-3106.

_____. 1986. "Drag on Naturally Rippled Beds under Oscillatory Flows," MP-86-13, U.S. Army Corps of Engineers, Coastal Engineering Research Center.

Madsen, O. S., and Grant, W. D. 1976a. "Sediment Transport in the Coastal Environment," Report No. 209, Ralph M. Parsons Laboratory for Water Resources and Hydrodynamics, Massachusetts Institute of Technology.

_____. 1976b. "Quantitative Description of Sediment Transport by Waves," <u>Proceedings of the 15th Coastal Engineering Conference</u>, pp 1093-1112.

Madsen, O. S., Mathisen, P. P., and Rosengaus, M. M. 1990. "Movable Bed Friction Factors for Spectral Waves," to appear in <u>Proceedings of the 22nd Coastal Engineering Conference</u>.

Madsen, O. S., Poon, Y.-K., and Garber, H. C. 1988. "Spectral Wave Attenuation by Bottom Friction: Theory," <u>Proceedings of the 21st Coastal Engineering Conference</u>, pp 492-504.

Madsen, O. S., and Wikramanayake, P. N. 1990. "Simple Models for Turbulent Wave-Current Bottom Bondary Layer Flow," Technical Progress Report submitted to the U.S. Army Corps of Engineers, Coastal Engineering Research Center.

Mathisen, P. P. 1989. "Experimental Study on the Response of Fine Sediments to Wave Agitation and Associated Wave Attenuation," M.S. thesis, Massachusetts Institute of Technology.

Miller, M. C., and Komar, P. D. 1980a. "Oscillation Sand Ripples Generated by Laboratory Apparatus," Journal of Sedimentary Petrology, Vol. 50, No. 1, pp 173-182.

_____. 1980b. "A Field Investigation of the Relationship between Oscillation Ripple Spacing and the Near-Bottom Water Orbital Motion," Journal of Sedimentary Petrology, Vol. 50, No. 1, pp 183-191.

Mogridge, G. R., and Kamphuis, J. W. 1972. "Experiments on Bed Form Generation by Wave Actio_," Proceedings of the 13th Coastal Engineering Conference, pp 1123-1134.

Nielsen, P. 1979. "Some Basis Concepts of Wave Sediment Transport," Series Paper No. 20, Institute of Hydrodynamics and Hydraulic Engineering, Technical University of Denmark.

_____. 1981. "Dynamics and Geometry of Wave Generated Ripples," Journal of Geophysical Research, Vol. 86, No. C7, pp 6467-6472.

_____. 1983. "Analytical Determination of Nearshore Wave Height Variation due to Refraction, Shoaling and Friction," Coastal Engineering, Vol. 7, pp 233-251.

_____. 1984. "Field Measurements of the Time-Averaged Suspended Sediment Concentration under Waves," Coastal Engineering, Vol. 8, pp 51-72.

Raudkivi, A. J. 1988. "The Roughness Height under Waves," Journal of Hydraulic Research, Vol. 26, No. 5, pp 569-584.

Riedel, H. P., Kamphuis, J. W., and Brebner, A. 1972. "Measurement of Bed Shear Stresses under Waves," Proceedings of the 17th Coastal Engineering Conference, pp 587-603..

Rosengaus, M. 1987. "Experimental Study on Wave Generated Bedforms and Resulting Wave Attenuation," Ph.D. thesis, Massachusetts Institute of Technology.

Sato, S., Mitani, K, and Watanabe, A. 1987. "Geometry of Sand Ripples and Net Sand Transport Due to Regular and Irregular Oscillatory Flows," Coastal Engineering in Japan, Vol. 30, No. 2, pp 89-98.

Sato, S., and Horikawa, K. 1988. "Sand Ripple Geometry and Sand Transport Mechanism Due to Irregular Oscillatory Flows," Proceedings of the 21st Coastal Engineering Conference, pp 1748-1762.

Schlichting, H. 1968. Boundary Layer Theory, 6th ed., McGraw-Hill.

Sleath, J. F. A. 1984. Sea Bed Mechanics, Wiley-Interscience.

_____. 1985. "Energy Dissipation in Oscillatory Flow over Rippled Beds," Coastal Engineering, Vol. 9, pp 159-170.

Stefanick, T. A. 1979. "A Realistic Model of Wave Attenuation Due to Bottom Friction," M.S. thesis, Massachusetts Institute of Technology.

Treloar, P. D., and Abernethy, C. L. 1978. "Determination of a Bed Friction Factor for Botany Bay, Australia," Coastal Engineering, Vol. 2, pp 1-20.

Vitale, P. 1979. "Sand Bed Friction Factors for Oscillatory Flow," Journal of Waterway, Port, Coastal and Ocean Division, ASCE, Vol. 105, No. WW3, pp 229-245.

Vongvisseiomjai, S. 1984. "Oscillatory Ripple Geometry," ASCE Journal of Hydraulic Engineering, Vol. 110, No. 3, pp 247-267.

_____. 1987. "Wave Friction Factor on Sand Ripples," Coastal Sediments '87: ASCE Specialty Conference, pp 393-407.

_____. 1988. "Time Dependent Wave Shear Stress," Proceedings of the 21st Coastal Engineering Conference, pp 1084-1097.

Wilson, K. C. 1989. "Friction of Wave Induced Sheet Flow," Coastal Engineering, Vol. 12, pp 371-379.

APPENDIX A: THE EXPERIMENTAL DATA

1. The experimental data used in this study are tabulated in this appendix. A blank in any column indicates that the data were not reported. When the water temperature was not given it was assumed to be 20°C for the purposes of this report. The derivation of the friction factor and equivalent wave parameters for some particular data sets are discussed in detail.

The Data of Carstens et al. (1969)

2. This was the first data set in which the energy dissipation over a movable bed was measured and these data have been the basis for nearly all the analyses of the problem. Carstens et al., measured the energy dissipated in the tunnel by monitoring the air pressure and the water level in the risers of their water tunnel. All the tests were conducted at approximately the same period with the orbital amplitude being varied.

3. They calculated the energy dissipation in the tunnel by carrying out a series of tests with a smooth flat bed. This resulted in a set of points through which they fit a calibration curve that gave the energy dissipation and amplitude. The energy dissipation measurements made with a rippled bed are accompanied by the corresponding smooth bed value that is obtained from this curve.

4. Let us denote by E_{ds} the total dissipation in the tunnel with a smooth flat bed. This value is composed of contributions E_{dt} which is the dissipation due to the curvature of the tunnel and the tunnel walls and E_{dsb} which is the dissipation on the smooth test bed itself. This can be written

$$E_{ds}(A_b) = E_{dt}(A_b) + E_{dsb}(A_b) \qquad (A.1)$$

since all these values depend on A_b, the orbital amplitude.

5. Similarly the total dissipation with a rippled bed, E_{dr}, can be written as

$$E_{dr}(A_b) = E_{dt}(A_b) + E_{drb} \qquad\qquad (A.2)$$

where E_{drb} is the dissipation due to rippled test bed. Subtracting (A.2) from (A.1) gives E_{drb} as

$$E_{drb}(A_b) = E_{dr}(A_b) - E_{ds}(A_b) + E_{dsb}(A_b) \qquad\qquad (A.3)$$

The first quantity on the right-hand side is measured during the rippled bed run while the second is known from the smooth bed curve. Carstens et al. neglected the third term as did most investigators, for example Nielsen (1983), Sleath (1985), and Vongvissesomjai (1987).

6. However, it is possible to estimate the value of this term by using the friction factor for a smooth bed as given by Figure 1. For example, for run 31B the reported values of E_{dr} and E_{ds} are 89.4 and 43.6 ft-lbs per cycle, respectively (121.21 and 62.77 meter-newtons). Ignoring E_{dsb} results in f_e being calculated as 0.07. At this orbital amplitude E_{dbs} is estimated as 4.18 ft-lb (5.67 meter-newtons) per cycle. Using this value changes f_e to 0.077, a difference of 10%. Therefore this method of estimating E_{dsb} was used to calculate f_e for this data set. These values are given in Table A.1.

7. Carstens et al. did not carry out an error analysis of their results. It can be seen from equation (A.3) that the error in E_{drb} is likely to be significant whenever E_{dr} and E_{ds} are comparable in value.

8. For example, in run 21 E_{dr} is 3.53 ft-lb and E_{ds} is given as 2.33 ft-lb, giving a difference of 1.22. Considering the scatter in the calibration curve for E_{ds} it can be estimated that the uncertainty in the value of E_{ds} is 0.2 which is about 15% of the calculated difference. This effect decreases when the amplitude of the flow is large because the difference between E_{dr} and E_{ds} is large. In Figure 19 it was noted that the greatest scatter in the values of k_n, which are derived from f_e, is seen at the lowest flow intensities.

9. Raudkivi (1988) also attempted to include an estimate of E_{dsb} when calculating f_e. However, it appears that he used a value of E_{dsb} that was representative of the whole tunnel and not of the smooth test bed. The result was that his derived values of f_e were too high.

Table A.1(a)

Wave Tunnel Data on Ripple Geometry and Energy Dissipation
under Regular Waves from Carstens at al. (1969)
d = 0.19 mm, s = 2.66

Orbital amplitude A_b	Radian frequency ω	Water temperature	Ripple length λ	Ripple height η	Energy dissipation factor f_e
(cm)	(s⁻¹)	(°C)	(cm)	(cm)	
9.00	1.74	17.2	11.6	2.1	–
11.87	1.75	25.3	15.2	2.5	–
18.16	1.77	26.2	10.9	1.5	0.112
23.70	1.78	24.8	10.6	1.3	0.0914
31.33	1.78	23.9	10.0	0.5	0.0849
8.18	1.77	24.4	10.4	2.1	0.202
11.23	1.77	23.9	–	–	0.219

A3

Table A.1(b)

Wave Tunnel Data on Ripple Geometry and Energy Dissipation
under Regular Waves from Carstens et al. (1969)
d = 0.297 mm, s = 2.47

Orbital amplitude A_b	Radian frequency ω	Water temperature	Ripple length λ	Ripple height η	Energy dissipation factor f_e
(cm)	(s⁻¹)	(°C)	(cm)	(cm)	
8.92	1.77	26.1	10.6	1.8	0.265
11.99	1.77	24.4	12.7	2.2	0.198
13.66	1.77	23.9	14.5	2.6	0.180
15.37	1.77	25.0	14.5	2.6	0.183
20.85	1.77	22.8	19.4	3.3	0.142
23.39	1.77	22.8	22.1	3.6	0.155
26.11	1.78	22.8	24.5	3.23	0.155
32.39	1.77	22.8	27.0	3.1	0.115
35.6	1.78	22.2	20.1	2.1	0.106
44.5	1.78	22.2	19.1	0.5	0.077
39.05	1.78	21.9	22.0	1.4	0.0717
28.08	1.77	22.8	24.5	3.2	0.134
8.00	1.76	23.9	10.4	1.9	0.385
8.64	1.83	23.9	10.9	1.7	–
7.35	1.899	23.3	8.8	1.6	–
9.53	1.71	22.8	11.8	2.1	–
7.76	1.66	24.2	10.5	1.8	–
5.97	1.77	21.1	–	–	0.342
38.57	1.77	18.3	–	–	0.0911

Table A.1(c)

Wave Tunnel Data on Ripple Geometry and Energy Dissipation
under Regular Waves from Carstens et al. (1969)
d = 0.585 mm, s = 2.66

Orbital amplitude A_b	Radian frequency ω	Water temperature	Ripple length λ	Ripple height η	Energy dissipation factor f_e
(cm)	(s⁻¹)	(°C)	(cm)	(cm)	
8.13	1.77	27.2	11.8	2.2	–
10.11	1.76	25.8	14.6	2.8	0.254
12.01	1.77	25.6	16.7	3.3	0.279
13.77	1.77	24.4	18.1	3.4	0.340
16.07	1.77	23.9	20.4	3.9	0.321
18.54	1.78	25.0	23.9	4.5	0.211
19.65	1.761	24.4	25.2	5.2	0.326
22.35	1.77	25.0	29.0	5.8	0.293
24.19	1.77	25.0	25.7	4.8	0.277
24.77	1.78	25.0	26.4	4.9	0.270
26.64	1.78	22.2	30.0	5.6	0.254
29.08	1.77	22.8	26.2	5.0	0.256
30.80	1.76	22.8	30.4	6.0	0.257
32.68	1.77	22.8	39.1	5.6	0.244
35.18	1.78	22.8	37.8	6.8	0.225
37.43	1.77	22.8	35.7	6.2	0.226
39.22	1.81	22.8	46.3	6.9	0.202
42.35	1.77	23.3	44.11	6.9	0.199
12.45	1.78	22.8	17.4	3.1	0.517
12.26	1.76	22.8	–	–	0.553
14.12	1.78	24.7	–	–	0.215

The Data of Lofquist (1986)

10. Lofquist measured the energy dissipation in a wave tunnel by means of pressure taps at either end. With the records from these taps he was able to calculate the instantaneous shear stress on the test bed. The effect of the sidewalls was accounted for by splitting the tunnel longitudinally and having a sand bed on one side and a smooth bed on the other.

11. The results are presented as curves of the instantaneous friction factor from the shear stress and also as time averages of the product of the shear stress and the bottom velocity. This allows the calculation of the f_e and f_w values plotted in Figure 3.

12. In order to measure the pressure it was found necessary to have a sand barrier at either end of the tunnel in the form of a rigid crest. This crest constrains the profile in the tunnel to an integer number of crests thereby affecting the spacing. To avoid this problem the flow conditions used were such that the resulting ripple length was the same as what was observed in tests with no barriers. Some runs were done with the flow chosen so that the ripple profile was different from the profile observed in an unconstrained bed in order to see what effect the distortion had on the energy dissipation.

13. Tests were also carried out with no barriers beginning from an initially flat bed. The friction factor during various stages of ripple growth was recorded along with the geometry.

14. All these data are given in Table A.2.

The Data of Rosengaus (1987) and Mathisen (1989)

15. These experiments were done in a wave flume with the energy dissipation measured by recording the change in wave height along the flume. The effects of non-linearity and sidewall friction were accounted for by doing preliminary runs with a smooth flat bed. Rosengaus and Mathisen also conducted experiments with irregular waves. These are the only experiments reported where energy dissipation in irregular waves has been measured.

Table A.2(a)

Wave Tunnel Data on Energy Dissipation over Equilibrium Ripples with Regular Waves from Lofquist (1986)
d = 0.18 mm, s = 2.65

Orbital amplitude A_b	Radian frequency ω	Water temperature	Ripple length λ	Ripple height η	Energy dissipation factor f_e
(cm)	(s⁻¹)	(°C)	(cm)	(cm)	
26.9	0.86	–	31.8	3.8	0.126
30.7	0.75	–	36.4	4.1	0.130
29.9	0.63	–	36.4	4.0	0.130
29.3	0.53	–	36.4	4.2	0.150
30.7	0.75	–	36.4	4.0	0.124
33.5	0.89	–	36.0	3.3	0.159
36.7	0.63	–	42.4	4.8	0.110
34.7	0.54	–	42.4	4.9	0.128
39.3	0.76	–	42.2	3.1	0.126
44.3	0.52	–	50.9	6.3	0.140
42.7	0.44	–	50.9	6.7	0.171
48.3	0.62	–	50.9	4.9	0.150
26.9	0.86	–	31.8	4.0	0.127
25.9	0.73	–	31.8	3.9	0.167
29.5	1.01	–	31.0	2.6	0.168
19.6	1.18	–	23.1	3.2	0.189
19.0	1.00	–	23.1	3.4	0.183
14.4	1.61	–	17.0	2.4	0.211
14.0	1.35	–	17.0	2.6	0.223
55.3	0.42	–	65.3	7.0	0.139

Table A.2(b)

Wave Tunnel Data on Energy Dissipation over Equilibrium Ripples
with Regular Waves from Lofquist (1986)
d = 0.55 mm, s = 2.65

Orbital amplitude A_b	Radian frequency ω	Water temperature	Ripple length λ	Ripple height η	Energy dissipation factor f_e
(cm)	(s⁻¹)	(°C)	(cm)	(cm)	
23.9	1.13	–	31.8	7.1	0.285
23.9	1.69	–	31.8	6.8	0.218
23.9	1.38	–	31.8	7.1	0.248
31.9	1.04	–	42.4	8.5	0.255
25.5	1.30	–	31.8	6.7	0.247
22.0	1.51	–	31.8	6.1	0.258
20.6	1.60	–	31.8	5.4	0.211
27.7	1.20	–	34.0	6.9	0.264
17.4	1.56	–	23.1	4.6	0.218
17.4	1.90	–	23.1	4.5	0.269
17.4	2.33	–	23.1	4.4	0.283
17.4	2.33	–	23.1	4.3	0.277
31.9	1.04	–	42.4	8.8	0.289
31.9	0.849	–	42.4	8.2	0.315
23.9	1.69	–	31.8	6.5	0.184
25.9	2.01	–	31.8	5.2	0.181
28.9	2.21	–	31.8	4.8	0.163
23.3	1.42	–	31.8	6.6	0.212
23.3	1.16	–	31.8	6.7	0.271
23.7	1.70	–	31.8	6.3	0.183
25.5	2.04	–	31.8	5.4	0.186
28.9	2.21	–	31.8	5.1	0.142
17.2	1.93	–	23.1	4.6	0.275
17.2	1.57	–	23.1	4.8	0.224
17.6	2.31	–	23.1	4.5	0.257
24.1	1.68	–	31.8	6.4	0.182
25.5	1.59	–	31.8	6.4	0.175
22.0	1.84	–	31.8	5.7	0.164
20.8	1.95	–	31.8	5.1	0.184
27.5	1.47	–	31.8	6.3	0.177
31.9	1.27	–	43.5	8.2	0.283
31.9	1.63	–	39.5	7.9	0.240
38.3	0.71	–	52.2	10.1	0.348
38.3	0.87	–	58.0	11.5	0.351
38.3	1.06	–	58.0	12.0	0.314
31.1	1.68	–	37.3	6.9	0.236
33.9	1.88	–	37.3	6.2	0.199
28.33	1.43	–	37.3	7.3	0.220
27.9	1.18	–	37.3	7.2	0.277
27.5	0.98	–	37.3	7.1	0.273

Table A.2(b)
cont'd

Orbital amplitude A_b	Radian frequency ω	Water temperature	Ripple length λ	Ripple height η	Energy dissipation factor f_e
(cm)	(s^{-1})	($^\circ$C)	(cm)	(cm)	
33.92	1.54	–	43.5	8.4	0.215
35.1	1.49	–	43.5	8.2	0.247
38.7	1.65	–	43.5	7.7	0.184
32.3	1.25	–	43.5	8.6	0.253
31.9	1.03	–	43.5	8.6	0.317
31.9	0.85	–	43.5	7.8	0.345
38.3	0.86	–	52.2	10.3	0.309
38.3	0.70	–	52.2	10.2	0.395
38.7	1.05	–	52.2	10.5	0.281
41.9	1.25	–	52.2	9.8	0.229
46.3	1.38	–	52.2	8.9	0.238
47.9	0.69	–	65.3	12.6	0.330
47.9	0.56	–	65.3	13.5	0.415
48.3	0.84	–	65.3	12.9	0.329
51.9	1.01	–	65.3	12.2	0.248
24.3	1.65	–	28.1	5.8	0.178
24.3	1.35	–	28.9	5.9	0.198
24.3	1.11	–	30.3	5.8	0.236
26.7	1.95	–	30.2	5.5	0.150
29.5	2.17	–	31.2	4.7	0.128
24.3	1.63	–	28.8	5.6	0.191
24.3	1.63	–	29.0	5.9	0.209

Table A.2(c)

Wave Tunnel Data on Energy Dissipation over Growing Ripples with Regular Waves from Lofquist (1986)
d = 0.18 mm, s = 2.65

Orbital amplitude A_b	Radian frequency ω	Water temperature	Ripple length λ	Ripple height η	Energy dissipation factor f_e
(cm)	(s⁻¹)	(°C)	(cm)	(cm)	
30.7	0.76	–	25.0	2.8	0.120
30.7	0.76	–	26.0	2.9	0.138
30.7	0.76	–	26.7	3.1	0.105

Table A.2(d)

Wave Tunnel Data on Energy Dissipation over Growing Ripples with Regular Waves from Lofquist (1986)
d = 0.55 mm, s = 2.65

Orbital amplitude A_b	Radian frequency ω	Water temperature	Ripple length λ	Ripple height η	Energy dissipation factor f_e
(cm)	(s⁻¹)	(°C)	(cm)	(cm)	
24.3	1.63	–	10.3	0.75	0.0679
24.3	1.63	–	24.0	4.0	0.147
24.3	1.63	–	25.7	5.0	0.177
30.3	1.32	–	14.6	1.75	0.0983
30.3	1.32	–	24.2	3.7	0.163
30.3	1.32	–	32.0	6.3	0.216
30.3	1.32	–	45.0	7.0	0.245
17.6	2.32	–	8.0	0.65	0.0789
17.6	2.32	–	13.8	2.4	0.168
17.6	2.32	–	21.3	3.9	0.226
38.7	1.05	–	7.6	0.3	0.0393
38.7	1.05	–	12.6	1.4	0.0483
38.7	1.05	–	15.8	1.7	0.0811
38.7	1.05	–	21.3	2.8	0.123
38.7	1.05	–	36.0	5.5	0.168
38.7	1.05	–	35.0	6.0	0.188

16. As a first step towards a random wave motion Rosengaus (1987) used two waves of different frequency which when superimposed gave rise to an amplitude-modulated carrier wave. The energy decrease along the flume was measured for each component separately by transforming the observed surface displacement to a frequency spectrum. The errors that arose due to the transfer of energy among the component waves were accounted for by conducting runs with a smooth flat bed.

17. A full spectrum was then simulated by increasing the number of component waves--ten in the case of Rosengaus and five in the case of Mathisen. The amplitude of each of the components, which were at different frequencies, was adjusted to obtain the required spectral shape.

18. The analysis in this report used an equivalent surface wave with the root-mean-square height and the average period. The root-mean-square height was taken to be the root mean square of the heights of the component waves. For the wave group experiments the average period was taken as the carrier wave period while for the spectral waves the average period was taken to be 0.95 of the period of the spectral peak as recommended by Goda (1985). The total energy dissipation was obtained by summing the measured dissipation for each component.

19. The derived values are given in Tables A.4 and A.5.

The Data of Sato (1988)

20. Sato (1988) studied ripple geometry created by regular and irregular waves in a wave tunnel. The irregular wave motion was created as follows. First a realization of the surface displacement was generated based on the Brechtschneider-Mitsuyasu spectrum. Linear wave theory was used to convert this into a time history of the bottom velocity which was simulated in the wave tunnel.

21. The spectrum that was used to generate the surface signal was specified by means of a significant wave height and a significant wave period. Therefore the equivalent wave condition needed for this report was obtained by dividing the significant height by $\sqrt{2}$ to obtain H_{rms} and by taking the average period to be equal to the significant wave period. The values obtained in this way are given in Tables A.6 and A.7.

Table A.3(a)

Wave Flume Data on Ripple Geometry and Energy Dissipation under Regular Waves from Mathisen (1989) and Rosengaus (1987)
d = 0.12 mm, s = 2.65

Orbital amplitude A_b	Radian frequency ω	Water temperature	Ripple length λ	Ripple height η	Energy dissipation factor f_e
(cm)	(s⁻¹)	(°C)	(cm)	(cm)	
4.61	2.39	–	6.5	1.2	0.193
6.44	2.39	–	8.1	1.3	0.190
8.00	2.39	–	8.8	1.2	0.107
9.39	2.39	–	9.2	1.3	0.094
10.3	2.39	–	9.0	1.2	0.084
7.16	2.39	–	8.9	1.3	0.178

Table A.3(b)

Wave Flume Data on Ripple Geometry and Energy Dissipation under Regular Waves from Mathisen (1989) and Rosengaus (1987)
d = 0.2 mm, s = 2.65

Orbital amplitude A_b	Radian frequency ω	Water temperature	Ripple length λ	Ripple height η	Energy dissipation factor f_e
(cm)	(s⁻¹)	(°C)	(cm)	(cm)	
5.52	2.39	–	–	–	0.272
6.94	2.39	–	–	–	0.171
8.56	2.39	–	–	–	0.176
10.42	2.39	–	–	–	0.166
11.73	2.39	–	–	–	0.149
12.59	2.39	–	–	–	0.111
14.04	2.39	–	–	–	0.110
9.42	2.39	–	–	–	0.174
9.08	2.39	–	9.9	1.6	0.173
5.55	2.39	–	7.4	1.3	0.243
7.23	2.39	–	8.9	1.5	0.223
12.05	2.39	–	10.6	1.6	0.180
6.07	2.90	–	8.6	1.3	0.165
9.16	2.03	–	10.2	1.6	0.113
6.43	2.62	–	8.7	1.4	0.187
9.27	2.39	–	10.9	1.7	0.177
9.01	2.39	–	10.1	1.6	0.156

Table A.4(a)

**Wave Flume Data on Ripple Geometry and Energy Dissipation
under Irregular Waves from Mathisen (1989) and Rosengaus (1987)
d = 0.12 mm, s = 2.65**

Orbital amplitude A_b	Radian frequency ω	Water temperature	Ripple length λ	Ripple height η	Energy dissipation factor f_e
(cm)	(s⁻¹)	(°C)	(cm)	(cm)	
6.43	2.51	–	8.2	1.1	0.0981
6.50	2.51	–	7.9	1.1	0.0840
6.86	2.51	–	9.4	1.1	0.0772
6.93	2.51	–	9.1	1.1	0.0950
5.76	2.51	–	7.7	1.2	0.116
6.48	2.51	–	8.3	1.0	0.122
6.56	2.51	–	8.7	1.1	0.159
5.42	2.51	–	7.6	1.2	0.271
6.95	2.51	–	8.2	1.0	0.166
7.21	2.51	–	–	–	0.159
6.04	2.51	–	–	–	0.197

Table A.4(b)

Wave Flume Data on Ripple Geometry and Energy Dissipation under Regular Waves from Mathisen (1989) and Rosengaus (1987)
d = 0.2 mm, s = 2.65

Orbital amplitude A_b	Radian frequency ω	Water temperature	Ripple length λ	Ripple height η	Energy dissipation factor f_e
(cm)	(s⁻¹)	(°C)	(cm)	(cm)	
4.51	2.51	–	–	–	0.258
4.75	2.51	–	7.7	1.1	0.195
8.10	2.51	–	8.6	1.0	0.0557
6.91	2.51	–	–	–	0.104
5.24	2.51	–	8.5	1.2	0.205
5.53	2.51	–	8.2	1.5	0.165
5.28	2.51	–	8.0	1.4	0.214
5.53	2.51	–	8.2	1.4	0.174
5.32	2.39	–	–	–	0.183
5.21	2.39	–	–	–	0.467
5.59	2.39	–	8.7	1.5	0.272
5.31	2.39	–	9.1	1.5	0.225
5.73	2.39	–	9.1	1.5	0.144
6.07	2.39	–	8.5	1.4	0.238
5.49	2.39	–	8.6	1.5	0.190

Table A.5(a)

Wave Tunnel Data on Ripple Geometry under Regular Waves from Sato (1988)
d = 0.18, s = 2.65 (fb: flat bed)

Orbital amplitude A_b	Radian frequency ω	Water temperature	Ripple length λ	Ripple height η
(cm)	(s^{-1})	(°C)	(cm)	(cm)
6.37	6.28	–	6.6	0.7
7.96	6.28	–	7.3	0.8
9.55	6.28	–	fb	fb
19.1	2.09	–	8.8	1.2
23.9	2.09	–	12.2	1.34
28.7	2.09	–	9.8	1.0
31.8	1.26	–	9.1	1.5
39.8	1.26	–	12.9	1.9
44.5	0.90	–	10.6	1.5
55.7	0.90	–	19.5	3.1
66.8	0.90	–	12.8	1.4
78.0	0.90	–	fb	fb

Table A.5(b)

Wave Tunnel Data on Ripple Geometry under Regular Waves from Sato (1988)
d = 0.56, s = 2.65 (fb: flat bed)

Orbital amplitude A_b	Radian frequency ν	Water temperature	Ripple length λ	Ripple height η
(cm)	(s⁻¹)	(°C)	(cm)	(cm)
19.1	4.19	–	18.5	2.5
23.9	4.19	–	fb	fb
38.2	2.09	–	31.4	5.6
47.8	2.09	–	35.5	5.7
52.5	2.09	–	29.3	2.9
57.3	2.09	–	fb	fb
63.7	1.26	–	33.8	4.7
79.6	1.26	–	26.5	2.2
87.5	1.26	–	43.6	5.3
95.5	1.26	–	fb	fb

Table A.6(a)

Wave Tunnel Data on Ripple Geometry under Irregular Waves from Sato (1988)
d = 0.18, s = 2.65 (fb: flat bed)

Orbital amplitude A_b	Radian frequency ν	Water temperature	Ripple length λ	Ripple height η
(cm)	(s^{-1})	(°C)	(cm)	(cm)
13.8	2.094	–	9.1	1.1
17.5	2.094	–	10.0	0.7
20.7	2.094	–	9.8	0.7
24.9	2.094	–	8.4	0.5
13.1	2.094	–	9.7	1.2
17.7	2.094	–	10.9	1.1
19.8	2.094	–	8.1	0.5
23.2	2.094	–	8.1	0.4
6.8	2.094	–	8.8	1.4
8.7	2.094	–	10.7	1.5
10.0	2.094	–	9.6	0.7
11.6	2.094	–	fb	fb
23.2	1.257	–	9.9	0.9
28.8	1.257	–	7.3	0.4
34.6	1.257	–	fb	fb
22.6	1.257	–	8.4	1.0
28.0	1.257	–	7.8	0.5
33.6	1.257	–	fb	fb
10.4	1.257	–	7.7	0.6
13.2	1.257	–	7.4	0.4
15.9	1.257	–	fb	fb

Table A.6(b)

Wave Tunnel Data on Ripple Geometry under Irregular Waves from Sato (1988)
d = 0.56, s = 2.65 (fb: flat bed)

Orbital amplitude A_b	Radian frequency ω	Water temperature	Ripple length λ	Ripple height η
(cm)	(s^{-1})	(°C)	(cm)	(cm)
14.7	4.189	–	16.8	1.6
18.4	4.189	–	16.1	1.1
20.2	4.189	–	fb	fb
7.2	4.189	–	17.5	1.8
9.0	4.189	–	18.6	2.2
9.9	4.189	–	fb	fb
28.2	2.094	–	27.5	3.3
35.1	2.094	–	35.0	2.7
38.6	2.094	–	fb	fb
14.7	2.094	–	32.6	4.9
17.6	2.094	–	31.4	3.1
18.5	2.094	–	26.4	2.5
20.1	2.094	–	fb	fb

Table A.7

Oscillating Bed Data on Energy Dissipation over Fixed Ripples with Regular Waves from Bagnold (1946)

Orbital amplitude A_b	Radian frequency ω	Water temperature	Ripple length λ	Ripple height η	Energy dissipation factor f_e
(cm)	(s^{-1})	(°C)	(cm)	(cm)	
5.0	3.13	–	10.0	1.5	0.206
5.0	3.88	–	10.0	1.5	0.254
5.0	5.86	–	10.0	1.5	0.300
5.0	8.20	–	10.0	1.5	0.265
5.0	9.66	–	10.0	1.5	0.245
10.0	1.24	–	10.0	1.5	0.233
10.0	1.38	–	10.0	1.5	0.246
10.0	1.79	–	10.0	1.5	0.224
10.0	1.94	–	10.0	1.5	0.223
10.0	2.64	–	10.0	1.5	0.237
10.0	2.66	–	10.0	1.5	0.196
10.0	3.76	–	10.0	1.5	0.237
10.0	5.72	–	10.0	1.5	0.208
15.25	1.23	–	10.0	1.5	0.139
15.25	1.61	–	10.0	1.5	0.146
15.25	1.64	–	10.0	1.5	0.154
15.25	2.57	–	10.0	1.5	0.138
15.25	2.59	–	10.0	1.5	0.150
15.25	2.86	–	10.0	1.5	0.164
15.25	3.20	–	10.0	1.5	0.144
15.25	3.55	–	10.0	1.5	0.155
15.25	4.21	–	10.0	1.5	0.137
20.3	0.814	–	10.0	1.5	0.115
20.3	1.12	–	10.0	1.5	0.126
20.3	1.67	–	10.0	1.5	0.134
20.3	2.48	–	10.0	1.5	0.132
20.3	2.58	–	10.0	1.5	0.152
30.5	0.671	–	10.0	1.5	0.096
30.5	1.07	–	10.0	1.5	0.088
30.5	1.35	–	10.0	1.5	0.091
30.5	1.65	–	10.0	1.5	0.083
30.5	1.78	–	10.0	1.5	0.092
5.0	2.38	–	20.0	3.0	0.294
5.0	3.51	–	20.0	3.0	0.244
5.0	5.73	–	20.0	3.0	0.232
5.0	7.62	–	20.0	3.0	0.257
5.0	8.48	–	20.0	3.0	0.283
10.0	1.34	–	20.0	3.0	0.231
10.0	2.20	–	20.0	3.0	0.251
10.0	3.41	–	20.0	3.0	0.219
10.0	3.64	–	20.0	3.0	0.217

Table A.7
cont'd

Orbital amplitude A_b	Radian frequency ω	Water temperature	Ripple length λ	Ripple height η	Energy dissipation factor f_e
(cm)	(s⁻¹)	(°C)	(cm)	(cm)	
10.0	4.01	–	20.0	3.0	0.255
10.0	5.17	–	20.0	3.0	0.196
15.25	0.762	–	20.0	3.0	0.262
15.25	1.17	–	20.0	3.0	0.223
15.25	1.67	–	20.0	3.0	0.229
15.25	2.15	–	20.0	3.0	0.247
15.25	2.77	–	20.0	3.0	0.189
15.25	3.07	–	20.0	3.0	0.199
20.3	1.16	–	20.0	3.0	0.199
20.3	1.49	–	20.0	3.0	0.224
20.3	1.73	–	20.0	3.0	0.214
20.3	1.90	–	20.0	3.0	0.211
20.3	2.30	–	20.0	3.0	0.178
30.5	0.561	–	20.0	3.0	0.130
30.5	0.759	–	20.0	3.0	0.139
30.5	0.919	–	20.0	3.0	0.146
30.5	1.07	–	20.0	3.0	0.143
30.5	1.20	–	20.0	3.0	0.153

Table A.8

Oscillating Bed Data on Energy Dissipation over Fixed Ripples with Regular Waves from Sleath (1985)

Orbital amplitude A_b	Radian frequency ω	Water temperature	Ripple length λ	Ripple height η	Energy dissipation factor f_e
(cm)	(s^{-1})	(°C)	(cm)	(cm)	
3.21	1.64	–	7.3	1.7	0.0486
3.21	2.20	–	7.3	1.7	0.0699
3.21	3.08	–	7.3	1.7	0.124
3.21	5.05	–	7.3	1.7	0.179
5.18	0.86	–	7.3	1.7	0.063
5.18	1.18	–	7.3	1.7	0.143
5.18	1.64	–	7.3	1.7	0.166
5.18	2.14	–	7.3	1.7	0.172
5.18	2.14	–	7.3	1.7	0.187
5.18	3.86	–	7.3	1.7	0.195
5.18	5.30	–	7.3	1.7	0.185
6.42	0.72	–	7.3	1.7	0.070
6.42	0.98	–	7.3	1.7	0.104
6.42	1.96	–	7.3	1.7	0.197
6.42	2.25	–	7.3	1.7	0.205
6.42	3.76	–	7.3	1.7	0.176
6.42	4.36	–	7.3	1.7	0.186
6.42	4.79	–	7.3	1.7	0.188
6.42	5.00	–	7.3	1.7	0.178
6.42	5.53	–	7.3	1.7	0.186
7.66	1.58	–	7.3	1.7	0.157
7.66	2.49	–	7.3	1.7	0.191
7.66	4.90	–	7.3	1.7	0.178
7.66	5.71	–	7.3	1.7	0.172
10.3	0.565	–	7.3	1.7	0.0246
10.3	0.91	–	7.3	1.7	0.118
10.3	0.99	–	7.3	1.7	0.133
10.3	1.73	–	7.3	1.7	0.151
10.3	2.74	–	7.3	1.7	0.151
10.3	3.07	–	7.3	1.7	0.158
10.3	3.85	–	7.3	1.7	0.153
10.3	4.57	–	7.3	1.7	0.146
10.3	4.98	–	7.3	1.7	0.143
10.3	4.99	–	7.3	1.7	0.149
15.4	0.438	–	7.3	1.7	0.0369
15.4	0.452	–	7.3	1.7	0.0649
15.4	0.644	–	7.3	1.7	0.0634
15.4	0.616	–	7.3	1.7	0.0679
15.4	0.473	–	7.3	1.7	0.0752
15.4	0.851	–	7.3	1.7	0.100
15.4	1.10	–	7.3	1.7	0.103

Orbital amplitude A_b	Radian frequency ω	Water temperature	Ripple length λ	Ripple height η	Energy dissipation factor f_e
(cm)	(s⁻¹)	(°C)	(cm)	(cm)	
15.4	1.73	–	7.3	1.7	0.113
15.4	2.08	–	7.3	1.7	0.118
15.4	2.70	–	7.3	1.7	0.125
15.4	2.70	–	7.3	1.7	0.118
15.4	3.31	–	7.3	1.7	0.115
15.4	3.83	–	7.3	1.7	0.112
20.5	0.346	–	7.3	1.7	0.040
20.5	0.513	–	7.3	1.7	0.0561
20.5	0.745	–	7.3	1.7	0.083
20.5	1.18	–	7.3	1.7	0.0917
20.5	1.50	–	7.3	1.7	0.0932
20.5	1.91	–	7.3	1.7	0.103
20.5	2.43	–	7.3	1.7	0.105
20.5	2.81	–	7.3	1.7	0.103
30.8	0.37	–	7.3	1.7	0.0465
30.8	0.727	–	7.3	1.7	0.0624
30.8	0.922	–	7.3	1.7	0.0676
30.8	1.23	–	7.3	1.7	0.0747
30.8	1.75	–	7.3	1.7	0.0736
30.8	2.19	–	7.3	1.7	0.0823

Table A.9

Field Data on Wave-Formed Ripple Geometry from Inman (1957)
(fb: flat bed)

Grain diameter d	Orbital amplitude A_b	Radian frequency ω	Water temperature	Ripple length λ	Ripple height η
(cm)	(cm)	(s^{-1})	(°C)	(cm)	(cm)
0.0118	55.0	0.628	–	5.8	0.46
0.0153	29.1	0.898	–	7.3	1.0
0.0145	20.5	0.785	–	8.8	1.2
0.015	43.1	0.849	–	7.0	0.6
0.0152	22.6	0.628	–	7.9	1.2
0.0151	39.9	0.542	–	7.9	0.6
0.0147	59.3	0.628	–	6.4	0.6
0.0157	61.4	0.571	–	7.9	0.6
0.0137	44.1	0.628	–	7.6	0.6
0.0124	33.4	0.683	–	7.3	0.9
0.0117	20.5	0.785	–	8.5	1.2
0.012	20.5	1.047	–	9.1	1.5
0.0117	11.9	1.013	–	11.9	1.8
0.0118	44.2	0.731	–	6.7	0.6
0.0124	23.7	0.648	–	9.1	0.9
0.0129	21.6	0.628	–	8.8	1.4
0.0126	31.3	0.622	–	7.6	0.8
0.0118	26.9	0.661	–	7.0	0.6
0.0114	55.0	0.571	–	7.6	0.6
0.0117	63.6	0.483	–	7.0	0.6
0.0135	10.8	0.785	–	18.6	2.3
0.0127	6.6	1.257	–	9.4	1.2
0.0115	10.8	0.785	–	18.9	2.4
0.0106	7.5	0.966	–	11.9	1.5
0.0107	4.3	1.047	–	10.0	1.8
0.0102	35.6	0.604	–	7.6	0.5
0.0102	25.9	0.739	–	7.9	0.7
0.0102	41.0	0.483	–	7.9	0.9
0.0106	14.0	0.661	–	16.1	1.5
0.0103	4.3	1.257	–	11.3	1.8
0.0109	10.8	0.483	–	11.9	1.8
0.0106	32.3	0.483	–	7.9	1.4
0.0106	24.8	0.628	–	14.9	1.5
0.0109	16.2	0.524	–	12.5	1.8
0.0113	22.6	0.524	–	11.6	1.5
0.0081	5.4	0.698	–	10.0	1.7
0.0555	44.2	0.698	–	57.3	9.1
0.0483	26.9	0.698	–	53.9	9.1
0.0635	97.0	0.419	–	85.3	15.2
0.0266	44.2	0.648	–	36.6	4.6
0.0302	25.9	0.610	–	46.3	6.7
0.0418	30.2	0.628	–	71.0	11.2

Grain diameter d	Orbital amplitude A_b	Radian frequency ω	Water temperature	Ripple length λ	Ripple height η
(cm)	(cm)	(s^{-1})	($^\circ$C)	(cm)	(cm)
0.0408	31.3	0.483	–	70.7	10.7
0.0412	37.7	0.524	–	81.4	12.5
0.0406	32.3	0.571	–	77.7	13.4
0.0406	32.3	0.571	–	80.5	12.8
0.0466	28.0	0.524	–	80.8	13.7
0.0345	33.4	0.571	–	79.2	12.2
0.0448	31.3	0.648	–	91.4	14.6
0.0462	23.7	0.610	–	91.4	14.6
0.0423	24.8	0.571	–	77.1	11.9
0.043	34.5	0.524	–	82.9	13.4
0.0457	23.7	0.628	–	53.3	7.6
0.0103	109.9	0.393	–	fb	fb

Table A.10

Field Data on Wave-Formed Ripple Geometry from Miller and Komar (1980)

Grain diameter d	Orbital amplitude A_b	Radian frequency ω	Water temperature	Ripple length λ	Ripple height η
(cm)	(cm)	(s^{-1})	(°C)	(cm)	(cm)
0.0165	89.2	0.722	10.0	22.4	–
0.0165	73.1	0.346	10.0	22.4	–
0.0165	178.5	0.628	10.0	9.4	–
0.0165	58.5	0.754	10.0	9.7	–
0.0165	132.7	0.440	10.0	16.6	–
0.0165	55.9	0.440	10.0	9.7	–
0.0165	47.8	0.722	10.0	18.1	–
0.0165	107.0	0.377	10.0	18.1	–
0.0165	6.8	0.785	10.0	25.1	–
0.0165	43.6	0.409	10.0	25.1	–
0.0165	14.3	0.785	10.0	22.4	–
0.0165	72.1	0.409	10.0	22.4	–
0.0165	51.5	0.785	10.0	7.8	–
0.0165	69.6	0.660	10.0	8.2	–
0.0165	98.6	0.471	10.0	8.4	–
0.0165	68.0	0.598	10.0	10.2	–
0.0165	60.6	0.598	10.0	7.7	–
0.0165	80.2	0.518	10.0	8.6	–
0.0165	90.7	0.542	10.0	8.1	–
0.0165	48.6	0.542	10.0	8.6	–
0.0165	30.0	0.849	10.0	8.3	–
0.0165	40.7	0.597	10.0	8.3	–
0.0165	61.9	0.377	10.0	8.3	–
0.0165	42.8	0.660	10.0	7.6	–
0.0165	32.0	0.660	10.0	8.2	–
0.0165	5.3	0.88	10.0	22.2	–
0.0165	31.1	0.409	10.0	22.2	–
0.0165	16.2	0.691	10.0	17.5	–
0.0165	34.1	0.628	10.0	14.9	–
0.0165	53.2	0.377	10.0	14.9	–
0.0287	10.3	1.047	20.0	22.3	–
0.0287	21.0	0.810	20.0	26.9	–
0.0287	12.4	0.754	20.0	27.1	–

Table A.11

Field Data on Wave-Formed Ripple Geometry from Nielsen (1984)
(fb: flat bed)

Grain diameter d	Orbital amplitude A_b	Radian frequency ω	Water temperature	Ripple length λ	Ripple height η
(cm)	(cm)	(s^{-1})	(°C)	(cm)	(cm)
0.049	50.7	0.748	26.0	50.0	5.0
0.05	47.0	0.885	26.0	50.0	15.0
0.05	50.4	0.838	26.0	50.0	15.0
0.05	50.3	0.827	26.0	50.0	15.0
0.025	41.3	0.873	26.0	fb	fb
0.016	67.8	0.739	25.0	fb	fb
0.023	93.8	0.582	26.0	fb	fb
0.017	124.5	0.487	26.0	fb	fb
0.011	39.8	0.885	26.0	5.0	0.5
0.012	31.3	0.885	26.0	fb	fb
0.033	58.6	0.806	20.0	70.0	7.5
0.033	59.9	0.706	20.0	70.0	7.5
0.03	47.7	0.766	20.0	65.0	7.5
0.03	64.1	0.698	26.0	65.0	7.5
0.04	58.6	0.766	20.0	80.0	10.0
0.04	70.9	0.748	20.0	60.0	8.0
0.04	60.8	0.806	20.0	60.0	8.0
0.017	91.7	0.766	21.0	fb	fb
0.016	66.4	0.731	21.0	fb	fb
0.016	78.1	0.598	21.0	fb	fb
0.02	56.5	0.795	21.0	fb	fb
0.016	86.0	0.661	21.0	fb	fb
0.044	58.1	0.628	22.0	55.0	5.7
0.062	137.5	0.524	22.0	55.0	5.7
0.051	94.6	0.598	22.0	48.0	4.3
0.045	63.6	0.668	22.0	48.0	4.3
0.038	116.1	0.487	16.0	50.0	8.0
0.038	101.4	0.499	16.0	50.0	9.0
0.045	88.8	0.56.	16.0	35.0	7.0
0.044	61.5	1.102	16.0	50.0	8.0
0.048	69.2	0.885	16.0	60.0	8.0
0.049	70.7	0.816	16.0	60.0	8.0
0.047	93.3	0.655	16.0	60.0	8.0
0.047	113.6	0.616	16.0	60.0	8.0
0.047	70.9	0.683	16.0	50.0	7.5
0.047	49.9	0.873	16.0	50.0	7.5
0.045	43.6	1.013	16.0	55.0	10.0
0.045	45.2	1.030	16.0	55.0	10.0

Table A.12

Wave Tunnel Data on Ripple Geometry under Regular Waves
from Mogridge and Kamphuis (1972)
d = 0.36, s = 2.65

Orbital amplitude A_b	Radian frequency ω	Water temperature	Ripple length λ	Ripple height η
(cm)	(s^{-1})	(°C)	(cm)	(cm)
77.6	0.781	17.8	42.7	7.0
9.41	2.50	17.2	12.9	2.1
15.7	1.56	17.2	19.7	3.3
15.6	1.56	17.8	20.0	3.4
25.8	1.56	17.8	28.1	4.8
21.8	1.11	17.8	28.4	4.8
29.4	1.11	17.8	37.7	5.8
32.0	1.56	17.8	33.8	5.1
36.0	0.781	17.8	44.3	6.8
42.8	0.781	17.8	50.0	8.8
51.9	0.781	17.8	54.8	9.5
53.7	0.625	17.8	60.1	10.1
60.9	0.521	17.8	65.0	10.4
66.8	0.521	17.8	73.5	11.5
75.4	0.447	18.3	81.2	13.6
93.0	0.447	18.3	101.7	18.4
13.5	1.56	17.8	17.2	3.0
21.1	1.56	17.8	25.0	3.8
29.7	1.56	17.8	33.0	4.6
38.0	1.56	17.8	27.8	4.9
43.9	1.56	17.8	22.7	3.9

Table A.13

Wave Flume Data on Ripple Geometry under Regular Waves
from Mogridge and Kamphuis (1972)
d = 0.36, s = 2.65

Orbital amplitude A_b	Radian frequency ν	Water temperature	Ripple length λ	Ripple height η
(cm)	(s⁻¹)	(°C)	(cm)	(cm)
2.50	5.77	13.6	3.3	0.57
2.69	5.81	13.3	3.6	0.50
3.00	5.82	14.4	3.7	0.53
3.22	5.82	14.4	4.0	0.64
3.40	5.81	13.3	4.2	0.65
3.66	5.81	13.3	4.8	0.66
3.13	5.79	13.8	4.4	0.61
2.91	5.82	7.5	3.6	0.51
3.27	5.78	5.8	4.3	0.61
2.93	5.80	7.2	3.8	0.53
2.74	5.82	4.7	3.4	0.44
3.30	5.80	4.4	4.3	0.62
3.00	5.81	5.6	3.6	0.54
3.98	5.90	8.1	4.9	0.69
4.03	5.77	5.8	5.3	0.75
4.17	5.78	7.8	5.0	0.69
3.51	5.80	5.3	4.5	0.61
4.28	5.78	5.8	5.0	0.67
3.90	5.78	16.7	5.0	0.65
2.62	6.27	18.1	3.2	0.48
2.25	6.28	18.9	3.0	0.44
2.83	6.26	19.2	4.0	0.54
3.61	6.28	19.4	4.5	0.62
3.14	6.23	17.8	4.0	0.56
3.30	6.27	18.6	4.1	0.56
2.89	6.24	18.9	3.7	0.54
3.24	6.26	19.2	4.2	0.57
3.66	6.28	19.2	4.6	0.62
3.07	4.99	18.9	4.5	0.67
4.00	5.01	19.2	5.2	0.70
3.57	4.99	18.6	4.8	0.69
3.81	5.00	18.3	5.1	0.80
2.92	4.98	18.6	3.5	0.53
3.05	5.00	18.6	4.2	0.59
2.97	5.00	18.6	4.1	0.59
5.57	2.50	19.2	6.6	1.15
8.78	2.50	19.2	7.7	1.13
5.88	2.50	19.2	7.0	1.31
5.55	2.50	17.8	6.6	1.00
5.47	3.10	19.2	6.4	0.95
4.91	3.11	21.9	6.1	0.85

Orbital amplitude A_b	Radian frequency ω	Water temperature	Ripple length λ	Ripple height η
(cm)	(s⁻¹)	(°C)	(cm)	(cm)
3.19	5.78	21.9	3.8	0.58
2.80	5.77	21.7	3.4	0.52
3.76	5.77	21.9	4.6	0.70
3.88	5.77	22.2	5.0	0.75
3.48	5.79	22.5	4.3	0.65
4.04	5.80	21.7	4.9	0.72
3.11	5.77	21.7	3.7	0.58
2.69	5.77	21.7	3.5	0.49
3.89	5.77	21.7	4.8	0.67

Table A.14(a)

Wave Tunnel Data on Ripple Geometry under Regular Waves
from Lofquist (1978)
d = 0.18 mm, s = 2.65

Orbital amplitude A_b	Radian frequency ω	Water temperature	Ripple length λ	Ripple height η
(cm)	(s⁻¹)	(°C)	(cm)	(cm)
11.4	2.11	–	14.0	2.0
11.4	1.92	–	14.0	1.7
11.4	2.32	–	13.3	1.8
9.27	2.29	–	11.4	1.6
18.3	1.14	–	21.0	2.8
27.5	0.83	–	26.8	3.3

Table A.14(b)

Wave Tunnel Data on Ripple Geometry under Regular Waves from Lofquist (1978)
d = 0.55 mm, s = 2.65

Orbital amplitude A_b	Radian frequency ω	Water temperature	Ripple length λ	Ripple height η
(cm)	(s⁻¹)	(°C)	(cm)	(cm)
45.8	0.76	–	72.7	15.5
45.9	0.78	–	58.4	12.4
49.7	0.56	–	55.1	10.9
36.7	0.96	–	55.3	10.1
36.7	1.18	–	42.8	8.9
36.7	1.48	–	40.1	7.6
23.0	1.51	–	27.9	5.4
30.1	1.20	–	32.7	6.5
36.7	0.78	–	50.1	10.6
19.3	1.84	–	24.9	4.3
13.9	2.23	–	23.9	3.5
15.1	2.05	–	22.9	3.5
13.8	2.32	–	20.8	3.2
14.3	2.27	–	19.0	3.4
24.5	1.41	–	31.9	6.0
11.9	2.77	–	10.9	2.8
23.8	1.45	–	25.4	5.5
18.3	1.83	–	27.4	4.1
27.6	1.41	–	33.7	6.8
27.6	2.79	–	26.2	4.5
13.7	2.32	–	21.8	3.4
13.8	1.90	–	16.0	2.2
13.7	1.35	–	16.0	2.0

Table A.15(a)

Wave Flume Data on Ripple Geometry under Regular Waves
from Nielsen (1979)
d = 0.082 mm, s = 2.65

Orbital amplitude A_b	Radian frequency ω	Water temperature	Ripple length λ	Ripple height η
(cm)	(s⁻¹)	(°C)	(cm)	(cm)
1.19	6.28	–	2.9	0.6
1.39	6.28	–	2.9	0.5
1.45	6.28	–	2.0	0.5
1.59	6.28	–	2.9	0.5
1.78	6.28	–	2.9	0.4
2.09	6.28	–	3.0	0.5
2.52	6.28	–	3.0	0.5
2.89	6.28	–	3.0	0.45
3.17	6.28	–	3.4	0.6
3.48	6.28	–	3.6	0.6
2.68	3.70	–	4.3	0.7
2.98	3.70	–	4.4	0.8
3.38	3.70	–	4.7	0.8
3.93	3.70	–	5.0	0.8
4.60	3.70	–	5.6	0.8
5.21	3.70	–	5.9	0.9
5.92	3.70	–	5.27	0.7
6.60	3.70	–	6.0	0.75
7.16	3.70	–	5.6	0.6
8.25	3.70	–	5.7	0.8
8.82	3.70	–	5.6	0.6
9.45	3.70	–	5.3	0.5
10.25	3.70	–	5.2	0.55
11.03	3.70	–	4.9	0.55

Table A.15(b)

Wave Flume Data on Ripple Geometry under Regular Waves from Nielsen (1979)
$d = 0.17$ mm, $s = 2.65$

Orbital amplitude A_b	Radian frequency ω	Water temperature	Ripple length λ	Ripple height η
(cm)	(s^{-1})	($^\circ$C)	(cm)	(cm)
3.13	3.70	–	4.5	0.8
4.64	3.70	–	5.6	0.9
5.97	3.70	–	6.7	1.15
6.92	3.70	–	7.5	1.25
7.90	3.70	–	8.7	1.3
8.66	3.70	–	8.5	1.2
9.36	3.70	–	7.4	1.2
10.47	3.70	–	7.4	1.0
12.75	3.70	–	8.8	1.2
13.10	3.70	–	9.4	1.3

Table A.15(c)

Wave Flume Data on Ripple Geometry under Regular Waves
from Nielsen (1979)
d = 0.36 mm, s = 2.65

Orbital amplitude A_b	Radian frequency ν	Water temperature	Ripple length λ	Ripple height η
(cm)	(s^{-1})	($^\circ$C)	(cm)	(cm)
4.05	3.70	–	5.7	0.95
4.47	3.70	–	6.3	1.0
5.00	3.70	–	7.1	1.0
6.40	3.70	–	8.6	1.4
7.52	3.70	–	9.6	1.55
9.22	3.70	–	11.9	1.8
10.5	3.70	–	12.8	1.9
11.29	3.70	–	13.4	2.2
12.4	3.70	–	13.8	1.9
14.0	3.70	–	13.3	1.9

Table A.16(a)

Wave Tunnel Data on Ripple Geometry under Regular Waves
from Lambie (1984)
d = 0.09 mm, s = 2.65

Orbital amplitude A_b	Radian frequency ν	Water temperature	Ripple length λ	Ripple height η
(cm)	(s⁻¹)	(°C)	(cm)	(cm)
11.0	1.09	65.2	11.6	1.45
39.0	1.09	60.2	55.0	3.5
14.5	1.05	64.0	12.4	1.8
8.0	2.73	62.2	7.6	1.4
20.25	1.14	69.0	21.2	1.8
21.0	1.14	65.0	15.6	2.1
13.0	1.40	65.0	14.0	2.0
10.5	2.00	64.4	10.5	1.5
8.5	2.17	59.6	11.0	2.1
10.5	2.17	59.6	10.6	1.3
19.5	2.17	67.2	6.5	2.0
7.75	2.73	52.3	6.6	1.2
11.25	2.73	54.0	8.0	1.2
9.0	2.73	52.4	7.5	1.2
17.5	1.40	65.0	18.0	2.7
14.5	2.00	60.0	8.3	2.3
59.5	1.09	57.0	fb	fb
65.0	1.09	57.0	fb	fb
80.5	0.84	48.4	fb	fb

Table A.16(b)

Wave Tunnel Data on Ripple Geometry under Regular Waves
from Lambie (1984)
d = 0.15 mm, s = 2.65

Orbital amplitude A_b	Radian frequency ω	Water temperature	Ripple length λ	Ripple height η
(cm)	(s⁻¹)	(°C)	(cm)	(cm)
19.75	1.34	56.5	18.2	2.9
19.75	1.34	56.0	23.0	3.3
6.75	2.24	59.0	11.5	2.1
10.25	2.24	50.0	12.5	2.3
11.75	2.31	60.5	13.2	2.2
21.75	1.63	64.5	25.3	3.2
19.25	1.64	60.5	20.3	4.0
16.75	1.64	58.7	18.5	3.3
13.9	1.64	63.5	16.3	2.8
10.15	1.63	60.0	11.5	1.8
15.5	1.06	65.0	17.2	2.8
25.5	1.63	62.5	22.2	4.1
24.0	1.62	70.0	20.4	4.0
39.4	1.19	68.5	33.0	3.9
36.0	1.19	64.2	30.5	4.4
28.0	1.19	64.2	27.0	3.8
26.3	1.19	67.1	24.0	4.8
17.7	1.19	69.7	20.2	3.4
9.75	1.19	75.5	18.8	3.1
9.15	1.19	63.0	9.4	1.4
12.6	1.19	63.0	9.3	1.7
11.5	1.19	63.0	13.8	2.6
37.75	0.87	21.9	29.7	4.0
21.0	1.37	22.0	17.3	2.8
40.5	1.34	51.0	33.0	3.7
15.0	2.24	64.5	17.0	2.5
18.75	2.24	59.5	20.0	1.9

Table A.17

Wave Flume Data on Ripple Geometry under Regular Waves
from Miller and Komar (1980)
d = 0.178 mm, s = 2.65

Orbital amplitude A_b	Radian frequency ω	Water temperature	Ripple length λ	Ripple height η
(cm)	(s⁻¹)	(°C)	(cm)	(cm)
7.59	2.09	17.0	6.0	1.0
8.37	2.09	17.0	7.5	1.0
15.4	1.57	17.0	13.5	1.0
26.8	1.26	17.0	10.6	1.0

Table A.18(a)

Wave Flume Data on Ripple Geometry under Regular Waves
from Kennedy and Falcon (1965)
d = 0.095 mm, s = 2.65

Orbital amplitude A_b	Radian frequency ω	Water temperature	Ripple length λ	Ripple height η
(cm)	(s^{-1})	(°C)	(cm)	(cm)
2.08	5.87	18.3	3.0	0.51
3.88	3.22	18.3	4.8	0.82
5.39	3.22	18.3	5.6	1.1
5.78	2.69	18.3	5.5	1.0

Table A.18(b)

Wave Flume Data on Ripple Geometry under Regular Waves
from Kennedy and Falcoln (1965)
d = 0.32 mm, s = 2.65

Orbital amplitude A_b	Radian frequency ω	Water temperature	Ripple length λ	Ripple height η
(cm)	(s⁻¹)	(°C)	(cm)	(cm)
4.99	4.52	23.9	6.3	1.0
5.33	4.00	23.9	7.2	1.2
6.47	4.00	23.9	8.6	1.6
4.79	4.52	23.9	6.2	1.2
4.26	4.00	23.9	5.9	1.3
3.24	4.52	23.9	4.6	0.7

Table A.19

Wave Flume Data on Ripple Geometry under Regular Waves from Inman and Bowen (1963)
d = 0.2 mm, s = 2.65

Orbital amplitude A_b	Radian frequency ω	Water temperature	Ripple length λ	Ripple height η
(cm)	(s^{-1})	($^{\circ}$C)	(cm)	(cm)
4.9	4.49	8.0	6.5	1.1
9.6	3.14	15.0	10.8	1.5

APPENDIX B: NOTATION

A_b bottom orbital amplitude $A_b = u_{bm}/\omega$

A_{br} representative bottom orbital amplitude of Madsen et al (1988), defined by equation (20)

A_{brms} bottom orbital amplitude based on the root-mean-square wave height

A_* acceleration parameter defined by equation (16)

d grain diameter

D_* non-dimensional parameter $D_* = d\omega^2/g$

e relative error defined in equation (27)

E_d time-averaged energy dissipation per unit area in the wave boundary layer

f_e energy dissipation coefficient defined by equation (1)

f_{erms} energy dissipation coefficient based on the root-mean-square wave height

f_w friction factor defined in equation (1)

f_w' friction factor based on the grain diameter

g acceleration due to gravity

h water depth

H_{rms} root-mean-square wave height

$H_{1/3}$ significant wave height

k wave number

k_n equivalent Nikuradse roughness

k_{nf} equivalent roughness due to form drag

k_{ns} equivalent roughness due to sediment motion

r root-mean-square error

Re near-bottom flow Reynolds number $Re = A_b U_{bm}/\nu$

Re_* friction Reynolds number

s specific gravity of the sand grains

$S_{ub}(\omega)$ frequency spectrum of near-bottom velocity

$S_\eta(\omega)$ frequency spectrum of surface amplitude

S_* non-dimensional parameter $S_* = d\sqrt{(s-1)gd}/4\nu$

t time

u velocity

$u_b(t)$ instantaneous near-bottom velocity

u_{bm} maximum near-bottom velocity

u_{bmrms} maximum near-bottom velocity based on the root-mean-square wave height

u_{br} representative near-bottom velocity of Madsen et al. (1988) defined by equation (18)

u_* shear velocity

u_{*m} shear velocity based on maximum bottom shear stress

X non-dimensional parameter $X = \theta/S_*$

z height above the bottom

z_0 bottom roughness scale

ζ_0 non-dimensional bottom roughness scale

η ripple height

θ non-dimensional parameter $\theta = u_{bm}^2/(s-1)gd$

κ Von Karman's constant $\kappa = 0.4$

λ ripple wave-length

ν kinematic viscosity

ρ density of water

ρ_s density of sand

τ shear stress

$\tau_b(t)$ instantaneous bottom shear stress

τ_{bm} maximum bottom shear stress

ϕ phase lead of maximum bottom shear stress

ψ Shields parameter $\psi = \tfrac{1}{2}f_w'u_{bm}^2/(s-1)gd$

ψ_c critical Shields parameter for the initiation of motion

ω radian frequency

REPORT DOCUMENTATION PAGE

1. AGENCY USE ONLY (Leave blank)	2. REPORT DATE August 1994	3. REPORT TYPE AND DATES COVERED Final report

4. TITLE AND SUBTITLE
Calculation of Movable Bed Friction Factors

5. FUNDING NUMBERS
WU 32463

6. AUTHOR(S)
Palitha Nalin Wikramanayake, Ole Secher Madsen

7. PERFORMING ORGANIZATION NAME(S) AND ADDRESS(ES)
Ralph M. Parsons Laboratory
Massachusetts Institute of Technology
Cambridge, MA 02139

8. PERFORMING ORGANIZATION REPORT NUMBER

9. SPONSORING/MONITORING AGENCY NAME(S) AND ADDRESS(ES)
U.S. Army Engineer Waterways Experiment Station
3909 Halls Ferry Road, Vicksburg, MS 39180-6199

10. SPONSORING/MONITORING AGENCY REPORT NUMBER
Contract Report DRP-94-5

11. SUPPLEMENTARY NOTES
Available from National Technical Information Service, 5285 Port Royal Road, Springfield, VA 22161.

12a. DISTRIBUTION/AVAILABILITY STATEMENT
Approved for public release; distribution is unlimited.

12b. DISTRIBUTION CODE

13. ABSTRACT (Maximum 200 words)

When wind-generated waves propagate from the deep ocean onto the continental shelf, they begin to feel the effects of the bottom. These bottom effects are accounted for as bottom friction, which arises due to the no-slip flow condition on the bottom. This condition gives rise to a bottom shear stress and a thin boundary layer where significant energy dissipation can take place.

The goal of this study was to develop a simple, physically realistic method to predict the friction factor over a movable sand bed under field conditions. Since reliable field measurements are available only for ripple geometry, laboratory data were used to derive the friction factor. Laboratory experiments are outlined in this report along with a brief description of the methods involved in the model derivation.

The model is formulated in two stages, deriving predictive relations for the ripple geometry of a given wave condition, and developing a relationship among flow, ripple geometry, and the resulting friction factor. The relation between ripple geometry and roughness and the relationship between the friction factor and the wave, sediment, and fluid parameters are analyzed. Finally, simple relationships for the prediction of the roughness of a movable bed under regular and irregular waves are proposed and numerical examples illustrating use of the relationships are given.

14. SUBJECT TERMS See reverse.	15. NUMBER OF PAGES 152
	16. PRICE CODE

17. SECURITY CLASSIFICATION OF REPORT UNCLASSIFIED	18. SECURITY CLASSIFICATION OF THIS PAGE UNCLASSIFIED	19. SECURITY CLASSIFICATION OF ABSTRACT	20. LIMITATION OF ABSTRACT

14. (Concluded).

Bed roughness   Movable bed
Bottom shear stress   Ripples
Friction factors   Wave-current interaction